



Advances in spatially encoded single-scan magnetic resonance imaging

Sina Marhabaie

► To cite this version:

Sina Marhabaie. Advances in spatially encoded single-scan magnetic resonance imaging. Theoretical and/or physical chemistry. Université Paris sciences et lettres, 2017. English. NNT : 2017PSLEE028 . tel-01791613

HAL Id: tel-01791613

<https://theses.hal.science/tel-01791613>

Submitted on 14 May 2018

HAL is a multi-disciplinary open access archive for the deposit and dissemination of scientific research documents, whether they are published or not. The documents may come from teaching and research institutions in France or abroad, or from public or private research centers.

L'archive ouverte pluridisciplinaire **HAL**, est destinée au dépôt et à la diffusion de documents scientifiques de niveau recherche, publiés ou non, émanant des établissements d'enseignement et de recherche français ou étrangers, des laboratoires publics ou privés.

THÈSE DE DOCTORAT

de l'Université de recherche Paris Sciences et Lettres
PSL Research University

Préparée à l'École Normale Supérieure-Paris

Advances in spatially encoded single-scan magnetic resonance imaging

Avancées de l'imagerie par résonance magnétique à encodage spatiotemporel

Ecole doctorale n°388

Chimie physique et chimie analytique

Spécialité Imagerie par résonance magnétique

COMPOSITION DU JURY :

Prof. GLADDEN Lynn
University of Cambridge,
La présidente du jury

Prof. GADIAN David
University College London, Rapporteur

Dr. DUMEZ Jean-Nicolas
Institut de Chimie des Substances
Naturelles-CNRS, Rapporteur

Prof. BODENHAUSEN Geoffrey
École Normale Supérieure-Paris,
Directeur de thèse

Dr. PELUPESSY Philippe
École Normale Supérieure-Paris,
Co-directeur de thèse

Soutenue par Sina MARHABAIE
le 12 décembre 2017

Dirigée par Prof.
Geoffrey BODENHAUSEN



Advances in Spatially Encoded Single-Scan Magnetic Resonance Imaging

By: Sina Marhabaie

Département de Chimie

École Normale Supérieure–Paris

A dissertation submitted to École Normale Supérieure–Paris
for the degree of Doctor of Philosophy

Contents

Acknowledgements	vii
Abstract	ix
List of abbreviations	xiii
Résumé	xv
Summary	xxv
1 An overview of magnetic resonance imaging	1
1.1 A short history of nuclear magnetic resonance	1
1.2 Basic theory of nuclear magnetic resonance	3
1.2.1 Basic interactions	3
1.2.2 Chemical shifts, and spin-spin couplings	4
1.2.3 Relaxation and Bloch equations	6
1.3 A short history of magnetic resonance imaging	8
1.3.1 Projectional magnetic resonance tomography	9
1.3.2 Slice-selection and line-scanning	9
1.3.3 Fourier NMR imaging and k -space	10
1.4 Non-Fourier MRI techniques	11
1.4.1 Hybrid imaging techniques	12
1.4.2 Cross-encoding	21
2 The effects of diffusion in spatially encoded magnetic resonance imaging	23
2.1 Diffusion: a short introduction	23
2.1.1 Fick's laws	24
2.1.2 Unrestricted diffusion	26
2.1.3 The effects of diffusion on NMR signals	26

2.1.4	Restricted diffusion, and apparent diffusion coefficient	27
2.2	Levelling the effects of molecular diffusion in spatially encoded magnetic resonance imaging	29
2.2.1	Introduction	29
2.2.2	Theory	30
2.2.3	Experimental	37
2.2.4	Results and discussion	42
2.2.5	Concluding remarks	48
3	Contrast enhancement by echo shifting in spatially encoded single-scan MRI	49
3.1	Types of contrast available in traditional Fourier MRI	49
3.2	Types of contrast available in spatially encoded MRI	52
3.3	Theory	53
3.3.1	Contrast enhancement	53
3.4	Experimental	60
3.5	Results and discussion	61
3.5.1	Enhanced contrast	61
3.5.2	Informative maps	64
3.5.3	Concluding remarks	68
4	Alternative sequences for single-scan time-encoding MRI	69
4.1	Gradient switching rate in available single-scan techniques	69
4.2	Modifications on the original hybrid time-encoding sequence	75
4.2.1	Uniform echo time	75
4.2.2	Reducing the gradient switching rate	76
4.2.3	Interleaved spin-packet-selection	79
4.3	Experimental	80
4.4	Results and discussion	81
4.4.1	Interleaving	83
4.4.2	The effects of excitation pulses with different shapes	84
4.4.3	Overlapping excitation pulses	84
4.4.4	Time-encoding sequence with uniform susceptibility effects	86
4.4.5	Importance of the coincidence of echoes	88
4.4.6	Concluding remarks	91
	Bibliography	95

پیشکش

به پدر و مادرم

به پاس رنجی که به جان خریدند تا مرا پرورند، به پاس محبت های بی دریغشان و به پاس فداکاری هایشان.

به همسرم

برای مهربانی هایی که پای نهال زندیگان ریخت تا جان یابد و به پاس همراهی صمیمانه اش.

Dedicated

To my father and my mother

For all pains they endured to bring me up, for their munificent sympathy, and for their sacrifices.

To my wife

For her compassion that supported to the sapling of our life, and for her sincere companionship.

Acknowledgements

I must express my profound gratitude to many people. The people with whom I spent some time of my life and from each I learnt something to keep for myself for my future career. I would like to acknowledge all the persons who taught me a scientific idea, a new aspect of life or even a French word.

I would also like to acknowledge my PhD advisor Prof. Geoffrey Bodenhausen for providing me the opportunity to pursue a PhD, his scientific support during my studies, the time he spent with me, and also for “Lettres persanes”, the book he donated to me. My co-advisor Dr. Philippe Pelupessy deserves a sincere thanks. I am deeply indebted to him for providing scientific ideas, assisting me during the experiments, and the fruitful discussions we had.

I thank all of my group mates for friendly atmosphere they provided in the laboratory. I will never forget all the fun we had, all the coffee we drank together, and all the smiles we offered to each other. All secretaries and staff of the École Normale Supérieure, specifically those who were patient when I wanted to talk with them in French are also acknowledged.

My family members have always stood behind me. I owe a debt of sincere and deep gratitude to my father for all his efforts and labours, to my mother for all sacrifices she has made for me, and my best friend, Parisa, for her company, sympathy and compassion during the last four years.

Finally, I thank all the jury members for reading and commenting on this dissertation.

Abstract

Although Nuclear Magnetic Resonance (NMR) has been discovered more than seventy years ago, it is still thriving and alive, covering a broad spectrum of applications in science, technology and industry. One of the most ubiquitous applications of Nuclear Magnetic Resonance is an imaging technique dubbed Magnetic Resonance Imaging (MRI), which has found many applications in science, technology, and particularly in medicine. Fourier or k -encoding techniques are MRI methods based on acquiring a magnetic resonance signal as a function of the parameter “ k ”, a subsequent Fourier transformation then will convert the signal to an image. Although nowadays Fourier techniques are prominent in MRI, there are other alternatives, among which spatial encoding, the main subject of this dissertation, should be mentioned. In spatial encoding (also known as time-encoding or spatiotemporal encoding), signal acquisition is performed in such a way that the signal intensity itself resembles the object. Consequently, in spatial encoding there is no need for a Fourier transformation for image reconstruction. However, there are some drawbacks associated with this technique. In particular, spatiotemporal encoding techniques entail a loss of signal-to-noise ratio (SNR). In addition, spatiotemporal encoding techniques usually lead to a higher specific absorption ratio (SAR) than k -encoding methods, which may limit their *in vivo* applications.

Single-scan hybrid imaging techniques that use traditional k -encoding in one direction, and spatiotemporal encoding in the other have been shown to be superior to

traditional full k -encoding methods (that use k -encoding in both directions) in suppressing the effects of frequency variations (caused by inhomogeneous magnetic fields, the presence of more than one chemical shift, or any other frequency variation) and lead to images that are much less distorted than traditional single-scan imaging methods. In this dissertation the main idea behind spatial encoding magnetic resonance imaging will be introduced. Image formation and image properties in different spatial encoding sequences will also be briefly investigated.

Then, the effects of diffusion on an established hybrid sequence called “Rapid Acquisition by Sequential Excitation and Refocusing, RASER” will be investigated. It will be shown that in spatial encoding sequences, the attenuation of the signal due to diffusion is often not uniform across the entire object, leading to a misleading contrast in the image. In order to eliminate this misleading contrast, a double-chirp RASER (DC-RASER) pulse sequence is proposed in this work. The experimental results are in accordance with our theoretical investigations about the effects of diffusion in these sequences. They also confirm that the signal attenuation due to diffusion is uniform for DC-RASER, as expected theoretically.

In order to develop applications of single-scan spatial encoding MRI we show how one can enhance the contrast in the original RASER sequence. By changing the timing of the pulse sequence, we achieved a variant of RASER called Echo Shifted RASER (ES-RASER), which provides a tunable contrast level. Finally, we show how one can improve some aspects of the available time-encoding sequences. By rearranging positive and negative gradients we show how one can reduce the switching rate of the gradients. This is important because fast gradient switching is not always technically feasible; in addition, it may unwittingly stimulate the patient’s nervous system. By using an additional gradient we can change the detection order in the original time-encoding sequence. This leads to an identical echo time for all echoes, and hence a uniform signal attenuation due to relaxation. Furthermore, we show how one can implement

time-encoding sequences in an interleaved fashion in order to reduce signal attenuation due to diffusion.

List of abbreviations

NMR: Nuclear Magnetic Resonance

MRI: Magnetic Resonance Imaging

MR: Magnetic Resonance

SNR: Signal-to-Noise Ratio

SAR: Specific Absorption Ratio

RASER: Rapid Acquisition by Sequential Excitation and Refocusing

DC-RASER: Double Chirp RASER

ES-RASER: Echo Shifted RASER

SPEN: SPatiotemporal ENcoding

EPI: Echo Planar Imaging

CW: Continuous Wave

TE: Echo Time

RARE: Rapid Acquisition with Relaxation Enhancement

FT: Fourier Transformation

te: Time-**E**ncoding

FID: Free Induction **D**ecay

PFG: Pulsed **F**ield **G**radient

ADC: Apparent **D**iffusion **C**oefficient

ADC: Analogue-to-**D**igital **C**onverter

se: Spatial **E**ncoding

TR: Repetition **T**ime

PRESTO: Principles of **E**cho **S**hifting with a **T**rain of **O**bservables

fMRI: functional **M**RI

Résumé

L'attribution de pas moins de six prix Nobel à des sujets liés à la Résonance Magnétique Nucléaire (RMN) est une indication claire de son importance. Il y a plus de soixante-dix ans que la RMN a été découverte, mais elle est toujours prospère et bien vivante, couvrant un large éventail d'applications dans les sciences, technologies et industries. L'une des applications omniprésentes de la RMN est une technique appelée imagerie par résonance magnétique (IRM), qui a trouvé beaucoup d'applications en sciences, en technologie et particulièrement en médecine.

Grâce aux énormes progrès de l'imagerie par résonance magnétique, les médecins peuvent non seulement obtenir facilement des informations utiles sur l'état des maladies de leurs patients, mais les neurologues peuvent aussi interpréter les fonctionnalités de différentes parties du cerveau humain. Aujourd'hui, à l'aide d'aimants supraconducteurs à ultra-haut champ, les biologistes moléculaires peuvent déterminer la structure et la dynamique de grandes protéines et enzymes avec une résolution atomique, et les pharmacologues utilisent fréquemment des méthodes basées sur la RMN pour étudier, concevoir et caractériser de nouveaux médicaments. Les applications de la résonance magnétique ne se limitent pas à la science ou à la technologie. La RMN, de plus, n'est plus une technique à coût élevé. Aujourd'hui, les spectromètres peu coûteux à faible champ peuvent jouer un rôle important à des fins éducatives. Ils ont en outre trouvé des applications dans l'industrie pétrolière et alimentaire, et de plus en plus d'applications

sont attendues pour la RMN à l’avenir. C’est pour ces raisons qu’effectuer un doctorat dans le domaine de la résonance magnétique semble toujours un choix idéal pour ceux qui aiment les défis scientifiques.

Les techniques de transformation de Fourier dites par “encodage dans l’espace k ” sont des méthodes d’IRM basées sur l’acquisition d’un signal de résonance magnétique en fonction d’un paramètre “ k ”, proportionnel à l’aire de gradients (généralement en fonction du temps), qui sera ensuite transformé en une image par transformation de Fourier. Aujourd’hui, les techniques à transformée de Fourier sont les plus importantes en IRM, mais il existe des alternatives parmi lesquelles “l’encodage spatial (ou temporel)”, qui est le sujet principal de cette thèse. Dans l’encodage spatial (également connu sous le terme d’encodage spatiotemporel ou SPEN[1, 2]), l’acquisition du signal s’effectue de telle manière que l’intensité du signal acquis ressemble directement à l’objet. Par conséquent, dans l’encodage spatial, la transformation de Fourier n’est pas nécessaire pour reconstruire l’image.

Il a été démontré que les techniques d’imagerie hybride à balayage unique, qui utilisent l’encodage k traditionnel dans une dimension et l’encodage spatiotemporel dans l’autre, sont supérieures aux méthodes traditionnelles qui utilisent l’encodage k dans les deux dimensions, notamment pour supprimer les effets de variations de fréquence (causées par des champs magnétique inhomogènes, ou par la présence de plusieurs déplacements chimiques, ou toute autre source de variations de fréquence), et conduisent à des images beaucoup moins déformées que les méthodes d’imagerie traditionnelles. Dans le premier chapitre de cette thèse, une brève histoire de la RMN et de l’IRM sera présentée, et la théorie de la RMN et des techniques traditionnelles d’imagerie par résonance magnétique de Fourier ainsi que le concept de l’espace k seront brièvement abordées.

Dans la suite du premier chapitre, l’idée principale principale qui est à la base de l’imagerie par résonance magnétique à encodage spatial sera expliquée, et le concept

d'espace hybride (un espace possédant la dimensionnalité de k dans une direction, et de l'espace normal dans l'autre) sera introduit. La formation d'une image et les propriétés de cette image obtenues en utilisant différentes séquences à encodage spatial, ainsi que leurs avantages et inconvénients par rapport aux méthodes traditionnelles d'encodage k seront brièvement étudiées. Deux artefacts d'image (très répandus dans les techniques d'encodage k à balayage unique), à savoir le “fantôme $\frac{N}{2}$ de Nyquist” les artefacts de “repli” (“wrap-around”) seront également introduits dans le premier chapitre. Il est important de savoir que ces deux artefacts sont intrinsèquement absents dans les méthodes d'imagerie hybride, car ils sont causés par la transformation de Fourier dans la dimension de l'encodage de phase. Comme dans les techniques hybrides on n'utilise pas de transformation de Fourier dans la direction d'encodage spatiotemporel, ces deux artefacts sont donc éliminés.

Dans le deuxième chapitre, les effets de la diffusion sur une séquence hybride établie appelée “acquisition rapide par excitation séquentielle et refocalisation” (RASER) [3] sont étudiés. Tout d'abord, la diffusion est définie, et la physique du mouvement brownien est expliquée de manière concise; puis la première et seconde loi de Fick et ainsi que la diffusion restreinte et non restreinte seront expliquées. Puis l'atténuation d'un signal de résonance magnétique due à la diffusion est étudiée, et les équations décrivant ce phénomène sont présentées. Ensuite, en utilisant le formalisme élaboré pour le traitement de la diffusion, les effets de diffusion seront explorés théoriquement en divisant la séquence en étapes de déphasage et de rephasage, et les équations correspondantes sont dérivées. Selon ces équations, dans les séquences d'encodage spatial, l'atténuation du signal due à la diffusion n'est souvent pas uniforme sur l'ensemble de l'objet, ce qui conduit à un contraste trompeur dans l'image.

Les résultats expérimentaux obtenus à différentes températures (donc avec différents coefficients de diffusion) sont conformes à nos prévisions théoriques sur les effets de la diffusion sur les séquences. Le deuxième ensemble d'expériences mise en œu-

vre avec différentes amplitudes des gradients d'encodage spatial confirme également nos recherches théoriques sur la diffusion. Afin d'éliminer le contraste trompeur, une séquence d'impulsion comprenant deux impulsions balayées en fréquence (DC-RASER) est proposée.

Les performances de RASER, de DC-RASER et de l'imagerie écho-planaire (EPI) seront comparées à trois différents niveaux d'homogénéité du champ magnétique. La fig. 1 montre les résultats expérimentaux. Comme on peut le voir, dans un champ magnétique inhomogène, l'EPI conduit à des images déformées tandis que RASER et DC-RASER produisent des images beaucoup moins affectées. Notez également que, bien que RASER soit robuste vis à vis des inhomogénéités du champ statique, la diffusion moléculaire et les gradients appliqués donnent lieu à une perte de signal non uniforme. Cependant, dans DC-RASER, le signal est uniformément pondéré à la fois par les effets de relaxation T_2 et par la diffusion. Les résultats obtenus dans le deuxième chapitre ont été publiés récemment [4].

Actuellement, les méthodes d'IRM basées sur transformation de Fourier sont prépondérantes dans l'imagerie par résonance magnétique. Ces méthodes sont bien développées et arrivées à maturité, couvrant un large spectre d'applications cliniques, du diagnostic de maladies, des études neurologiques et fonctionnelles, de l'angiographie, etc. Contrairement aux méthodes traditionnelles d'encodage k , les méthodes d'encodage spatial ne sont pas encore complètement arrivées à maturité. Il y a beaucoup d'ouvrages sur divers aspects d'encodage spatial comme la théorie et les principes, la résilience aux champs magnétiques inhomogènes, la résolution et les applications. Cependant, il n'y a que quelques travaux publiés concernant le contraste. Par conséquent, le troisième chapitre de cette thèse porte sur l'amélioration du contraste obtenu en modifiant la séquence RASER, qui débute par une revue de la théorie de la pondération du signal (pondération du signal par la relaxation T_1 et T_2 , diffusion, etc.) , et continue avec une introduction sur le décalage des échos.

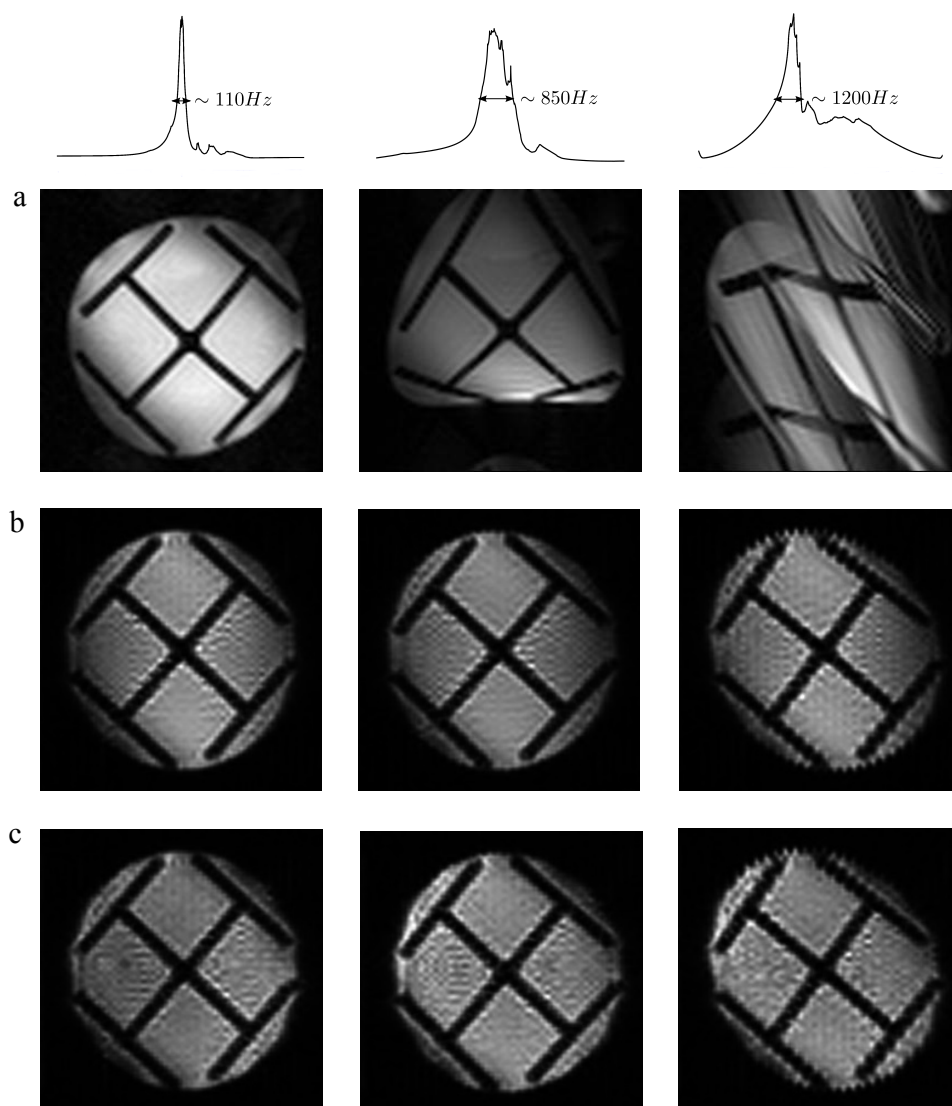


Figure 1: Résumé des résultats expérimentaux du deuxième chapitre. Images obtenues à 800MHz d'un fantôme constitué d'un morceau de plastique immergé dans l'eau dé-ionisée dans un tube de 25 mm de diamètre. De gauche à droite: effets de l'inhomogénéité croissante du champ statique, révélés par les spectres des protons de l'ensemble de fantôme montrés en haut. Rangée supérieure: EPI par échos de spin, obtenu avec un champ de vision FOV 27.0×27.0 mm, une dimension de la matrice 64×64 , une bande passante de 250 kHz, et un temps d'écho $TE = 24.44$ ms. Rangée du milieu: RASER, FOV 27.0×27.0 mm, taille de la matrice 64×64 , bande passante dans la direction de la lecture ("readout") 250 kHz, $TE = 46.0$ ms, temps total d'acquisition = 67.8 ms. Rangée du bas: DC-RASER, avec les mêmes paramètres que le RASER. L'épaisseur de la tranche est d'environ 1 mm dans toutes les images.

Dans la littérature d'IRM, le décalage des échos dans l'espace k ou dans l'espace du temps peut être dû à quelques gradients supplémentaires, volontaires ou involontaires, qui peuvent affecter la formation des échos. Habituellement, dans les méthodes traditionnelles d'encodage k , il se produit involontairement, et par conséquent, il est considéré comme une source d'artefacts d'images (chapitre 20 de la référence [5]). Il a également été utilisé pour améliorer le niveau de contraste dans l'IRM à encodage k [6].

En modifiant le déroulement de la séquence d'impulsions RASER, nous avons réalisé une variante de RASER appelé RASER avec écho décalé (ES-RASER), qui fournit un contraste dû à la relaxation transversale homogène avec un niveau ajustable. Il sera montré que RASER a une bonne résilience par rapport aux inhomogénéités du champ (comme les autres méthodes d'encodage spatiotemporel), mais, dans certains cas il souffre d'un manque de contraste. Cela est parce que RASER est une séquence d'écho de spin. Utilisant des impulsions de refocalisation de 180° , RASER refocalise tous les effets de susceptibilité. Cependant, lorsque deux voxels ont plus ou moins la même densité de spin ρ , ou lorsque leur temps de relaxation T_1 ou T_2 ne sont pas significativement différentes, ces effets de susceptibilité peuvent servir de source de contraste. En décalant les échos (c'est-à-dire en enregistrant le signal après ou avant la formation de l'écho), nous montrons comment on peut améliorer le contraste dans RASER. Les résultats expérimentaux principaux sont présentés sur la fig. 2.

Le fantôme représenté sur la fig. 2 comprend deux parties, une pièce en plastique en forme de croix immergée dans l'eau, et une mince fibre de verre faite en étirant un morceau de verre fondu chauffé dans une flamme (qui donne lieu à des taches noires dans fig. 2d–f). Comme on peut le voir, EPI donne des images déformées dans un champ magnétique inhomogène. Bien que ces distorsions soient absentes dans RASER (fig. 2c), le contraste ne suffit pas à identifier l'existence de la petite fibre de verre. Cependant, cette fibre de verre peut être facilement perçue dans les images ES-RASER (fig. 2d–f). En outre, les images ne sont pas déformées.

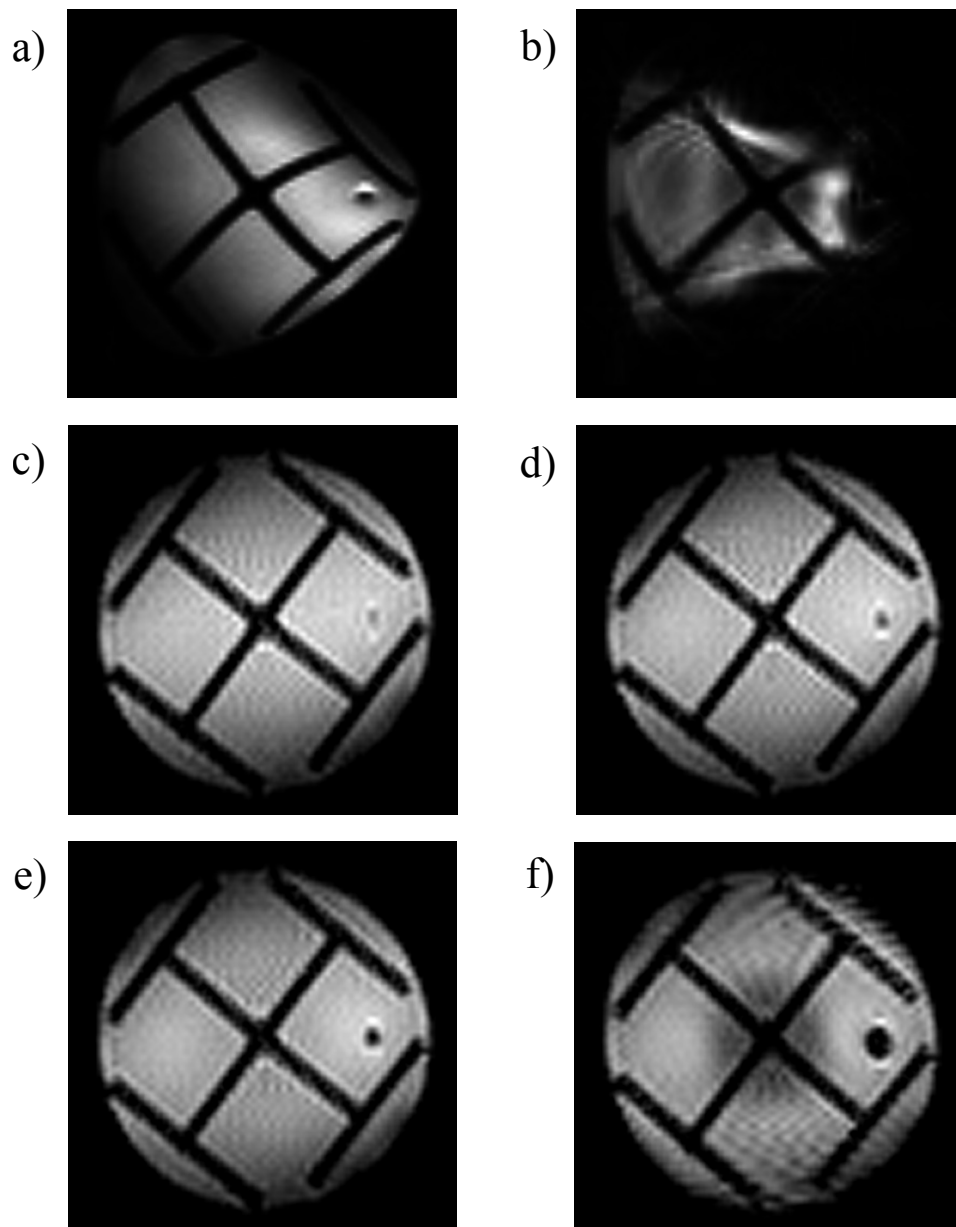


Figure 2: Résumé des résultats expérimentaux du troisième chapitre. (a) EPI par écho de spin conventionnel, et (b) EPI par écho de gradients (sans impulsion de refocalisation), tous les deux avec une taille de matrice 64×64 , un champ de vision FOV 27.0×27.0 mm, une bande passante de lecture de 250 kHz, mais avec $TE = 45,8$ ms pour (a) et $TE = 25,6$ ms pour (b). (c), (d), (e) et (f) RASER avec écho décalé (ES-RASER) avec matrice de taille 64×64 , champ de vision 27.0×27.0 mm, bande passante de 250 kHz (dans la direction de lecture). (c) $TE = 46,0$ ms et $\xi = 0$ (le paramètre ξ donne la mesure du décalage de l'écho). Les images (d) à (f) obtenues en augmentant ξ . (d) $TE = 43,8$ ms et $\xi = 0,1$. (e) $TE = 41,6$ ms et $\xi = 0,2$. (f) $TE = 30,7$ ms et $\xi = 0,7$.

Un aspect de ES-RASER est que la quantité de décalage peut être réglée par ajuster un paramètre appelé “paramètre de décalage” ξ . Nous allons montrer comment la variation de ξ permet de réaliser des images avec des niveaux de contraste différents. Enfin, en utilisant une série d’images obtenues avec différents paramètres de décalage, nous montrons comment on peut extraire certaines cartes informatives qui fournissent une information pixel par pixel sur les paramètres $\frac{1}{T_2^*(r)} = [\frac{1}{T_2(r)} + \frac{1}{T_2^{inh}(r)}]$ ou $[\frac{1}{T_2^{inh}(r)} - \frac{1}{T_2(r)}]$. Les résultats obtenus dans le troisième chapitre ont récemment été publiés [7].

Quarante ans après son invention, l’imagerie écho-planaire (EPI) reste l’une des techniques les plus populaires d’IRM à balayage unique [8, 9], et elle est largement utilisée dans l’imagerie fonctionnelle[10]. Un inconvénient de cette méthode est l’alternance de gradients positifs et négatifs, qui nécessite une commutation très rapide des gradients, ce qui rend cette méthode techniquement difficile à mettre en œuvre. Typiquement, des temps de montée et de descente d’environ 100 μs sont nécessaires pour cette méthode [10]. Plus important encore, même si la commutation rapide entre les gradients positifs et négatifs était techniquement possible, la vitesse de commutation des gradients doit être limitée pour des applications in vivo afin de ne pas stimuler le système nerveux du patient [11].

Le quatrième chapitre est dédié à l’encodage temporel [12, 13]. C’est une technique d’imagerie très similaire à l’encodage spatial, avec cette différence qu’elle utilise un train d’impulsions sélectives modulées en amplitude pour l’encodage temporel, tandis que, dans l’encodage spatial, une impulsion “chirp” balayée en fréquence est utilisée pour l’encodage spatial. Au début de ce chapitre, les techniques à balayage unique disponibles avec différentes vitesses de commutation sont discutées. Ensuite, nous discutons certaines modifications que nous avons apportées afin d’améliorer les séquences d’encodage temporel existantes [12, 13]. En utilisant un gradient supplémentaire, nous pouvons modifier l’ordre de détection de la séquence d’encodage temporel d’origine. Cela conduit à un

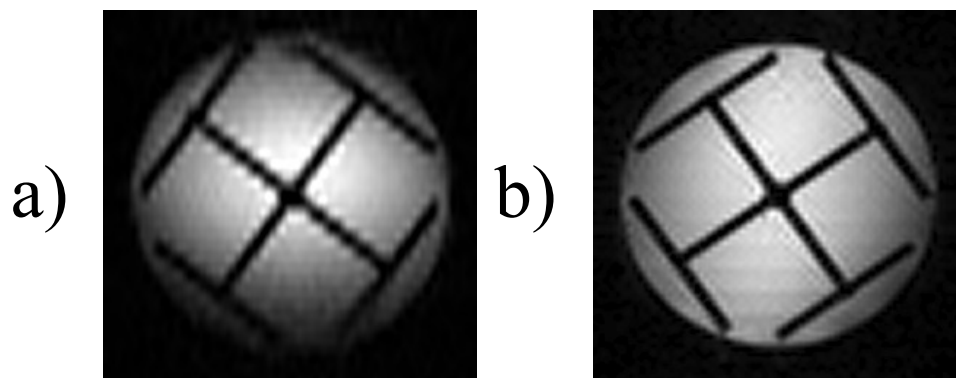


Figure 3: (a) Image d’encodage temporel à balayage unique obtenue par une séquence d’encodage temporel modifiée (fig. 4.4b), avec une taille de matrice de 32×64 (32 dans la direction d’encodage temporel et 64 dans la direction d’encodage k), FOV 27.0×27.0 mm et $TE = 23.6$ ms. (b) Image semblable à celle de (a) mais obtenue par un quadruple entrelacement des fréquences, avec une matrice taille de 64×64 (16×64 pour chaque balayage), FOV 27.0×27.0 mm et $TE = 12.4$ ms.

temps d’écho identique pour tous les échos, et donc une atténuation uniforme du signal due à la relaxation.

Les méthodes d’encodage temporel utilisent des gradients longs et intenses pendant l’excitation et la détection, et par conséquent, elles souffrent généralement d’une atténuation significative du signal due à la diffusion. On montrera comment la mise en œuvre d’une séquence d’encodage temporel d’une manière entrelacée entraîne une réduction notable de l’atténuation du signal due à la diffusion. La fig 3a montre des images obtenues par une séquence d’encodage temporel à balayage unique. Les effets de l’atténuation du signal due à la diffusion peuvent être observés en bas et en haut. Les images de la fig. 3b ont été obtenues par la même séquence de codage temporel, mais de manière entrelacée. De toute évidence, l’atténuation du signal due à la diffusion est beaucoup plus faible qu’avant. Bien entendu, cela entraîne une perte des avantages offerts par une séquence à balayage unique. En continuant nos modifications, on montrera comment on peut modifier la séquence d’encodage temporel d’origine pour réduire la vitesse de commutation des gradients. En réarrangeant les gradients positifs et négatifs, nous montrons comment on peut réduire cette vitesse de commutation.

Comme différentes impulsions d'excitation avec différentes bandes passantes de l'excitation peuvent être utilisées pour les séquences d'encodage temporel, il est important de connaître les effets de l'utilisation d'impulsions d'excitation différentes. Ces effets sont étudiés expérimentalement dans le quatrième chapitre. En plus, l'effet d'un chevauchement entre les paquets de spin sélectionnés sera examiné. Aussi, nous expliquerons pourquoi dans certaines versions modifiées utilisant l'encodage temporel, le réglage minutieux des temps d'écho dans les deux directions de lecture et d'encodage temporel est important.

Finalement, cette thèse se termine par un récapitulatif des conclusions principales et quelques perspectives pour des recherches futures.

Summary

Dedication of six Nobel prizes to the subjects related to Nuclear Magnetic Resonance (NMR) is a clear indication of its importance. Although NMR has been discovered more than seventy years ago, it is still thriving and alive, covering a broad spectrum of applications in science, technology and industry. One of the most ubiquitous applications of NMR is an imaging technique dubbed Magnetic Resonance Imaging (MRI), which has found many applications in science, technology, and particularly in medicine. Thanks to enormous advances in MRI, nowadays, not only can physicians easily obtain useful information about the status of their patients' diseases, but neurologists can also interpret the functionality of different parts of the human brain. Today, owing to ultra high-field super-conducting magnets, not only can molecular biologists determine the structure and dynamics of large proteins and enzymes with atomic resolution, but pharmacologists frequently use NMR-based methods to investigate, design, and characterize new drugs. Applications of magnetic resonance are not limited to science or technology, moreover NMR is not necessarily an expensive technique any more. These days, inexpensive low field spectrometers can play an important role for educational purposes, and in addition they have found some applications in oil and food industry, so that further applications can be expected for NMR in future. All this means that pursuing a PhD degree in the field of magnetic resonance appears to be an ideal choice for those who like scientific challenges.

Fourier or k -encoding techniques are MRI methods based on acquiring a magnetic resonance signal as a function of a parameter “ k ” that is proportional to the area of a pulsed magnetic field gradient (as a function of time), a subsequent Fourier transformation then will convert the signal to an image. Although nowadays Fourier techniques are prominent in MRI, there are other alternatives, among which (time-) spatial encoding (also known as spatiotemporal encoding [1, 2]), the main subject of this dissertation, should be mentioned. In spatiotemporal encoding signal acquisition is performed in such a way that the signal intensity itself resembles the object. Consequently, in spatial encoding there is no need for a Fourier transformation for image reconstruction.

Single-scan hybrid imaging techniques that use traditional k -encoding in one direction, and spatiotemporal encoding in the other have been shown to be superior to traditional full k -encoding methods that use k -encoding in both directions in suppressing the effects of frequency variations (caused by inhomogeneous magnetic fields, the presence of several chemical shifts, or any other frequency variation) and lead to images that are much less distorted than traditional single-scan imaging methods. The first chapter of this dissertation provides a short history of NMR and MRI. Also in this chapter, the theory of NMR, traditional Fourier MRI techniques, as well as the concept of k -space will be briefly presented.

In the rest of the first chapter, the main idea behind spatiotemporal encoding MRI will be explained, and the concept of “hybrid space” (a space which has the dimensionality of k -space in one direction, and of normal space in the other) will be introduced. Image formation and image properties in different spatiotemporal encoding sequences, as well as their pros and cons compared to traditional k -encoding methods, will be briefly investigated. Two image artefacts (which are prevalent in traditional single-scan k -encoding techniques) namely “Nyquist $\frac{N}{2}$ ghost” and “wrap-around artefacts” are also discussed in the first chapter. It is important to know that both of these artefacts are inherently absent in hybrid imaging methods, because they are caused by the Fourier

transformation. Since hybrid techniques do not use any Fourier transformation (in the spatiotemporal encoding direction), they are inherently absent in hybrid MRI techniques.

In second chapter, the effects of diffusion on an established hybrid sequence called “Rapid Acquisition by Sequential Excitation and Refocusing” (RASER) [3] are investigated. First, diffusion is defined, and the physics behind the Brownian motion is concisely explained; then Fick’s first and second laws, as well as restricted and unrestricted diffusion are introduced. Next, the attenuation of a magnetic resonance signal due to diffusion is investigated, and the equations describing this phenomenon are presented. Using an established formalism for the treatment of diffusion, by dividing the sequence into de-phasing and re-phasing periods the effects of diffusion will be explored theoretically, and corresponding equations will be derived. According to these equations, the attenuation of the signal due to diffusion is often not uniform across the entire object in spatial encoding sequences, causing a misleading contrast in the image.

Experimental results obtained at different temperatures (hence with different diffusion coefficients) are in accordance with our theoretical investigations about the effects of diffusion. A second set of experiments implemented with different amplitudes of spatial encoding gradients also confirms our theoretical investigations about diffusion. In order to eliminate the misleading contrast caused by diffusion, a double-chirp RASER (DC-RASER) pulse sequence is proposed and tested.

The performance of RASER, DC-RASER, and echo planar imaging (EPI) will be compared at three different levels of field homogeneity. Fig. 1 shows the experimental results. As can be seen, in an inhomogeneous magnetic field, EPI leads to distorted images while RASER and DC-RASER bring about images that are much less distorted. Also note that, although RASER is robust with respect to field inhomogeneities, molecular diffusion through applied gradients gives rise to a non-uniform signal loss. However, in

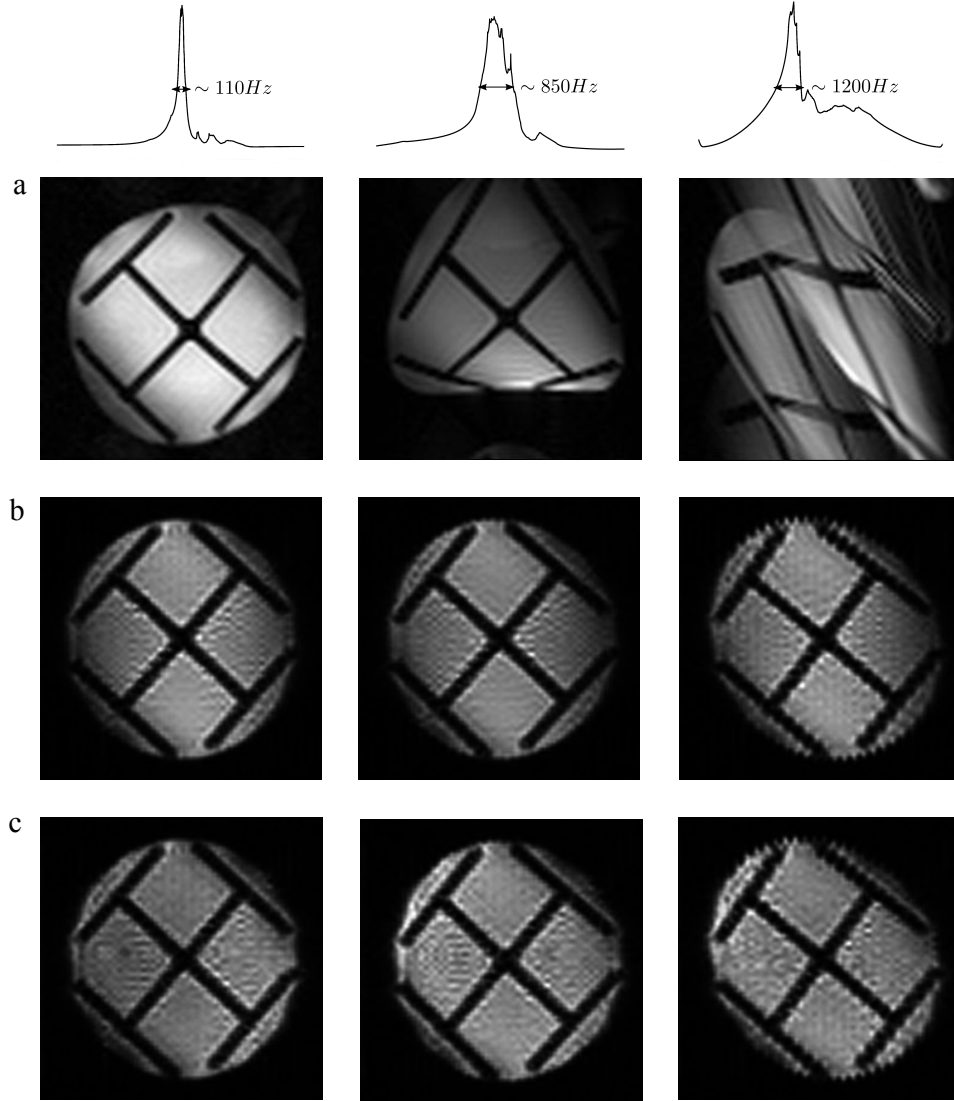


Figure 1: Summary of experimental results of the second chapter. Images of a phantom consisting of a piece of plastic immersed in de-ionized water in a tube of 25 mm diameter at 800 MHz. From left to right: effects of increasing the inhomogeneity of the static field, as evidenced by the proton spectra of the entire phantom shown along the top. Top row: spin echo EPI obtained with a field of view (FOV) of 27.0×27.0 mm, matrix size = 64×64 , bandwidth = 250 kHz, echo time $TE = 24.44$ ms. Middle row: RASER, FOV = 27.0×27.0 mm, matrix size 64×64 , bandwidth in the readout direction 250 kHz, $TE = 46.0$ ms, total acquisition time 67.8 ms. Bottom row: DC-RASER, with the same parameters as RASER. The slice thickness was about 1 mm in all images.

DC-RASER the signal is uniformly weighted both by T_2 relaxation and diffusion effects. The results obtained in the second chapter have recently been published [4].

Today, Fourier-based MRI methods are prominent in magnetic resonance imaging. These methods are well-developed and mature, covering a broad spectrum of clinical applications like disease diagnose, neurological and functional studies, angiography, etc. In contrast to traditional k -encoding methods, spatial encoding methods are not completely mature yet. There are plenty of published works about various aspects of spatial encoding, its theory and principles, its resilience to inhomogeneous magnetic fields, its resolution, and its applications. However, there are only a few published works about the resulting contrast in spatial encoding methods. Therefore, the third chapter of this dissertation deals with enhancing the contrast of the RASER sequence. This chapter starts with a review of the basic theory of signal weighting in traditional k -encoding methods, and continues with an introduction about echo shifting.

In the MRI literature, echo shifting is referred to as any echo displacement (in k -space or with respect to time) due to some additional gradients that willingly or unwillingly affect the formation of echoes. Frequently, echo shifting may occur unwillingly in traditional k -encoding methods, and therefore, it is considered to be the source of some image artefacts (see chapter 20 of ref. [5]). Echo shifting has been used to enhance the contrast level in k -encoding MRI as well [6].

By changing the timing of the RASER pulse sequence, we achieved a variant of RASER called Echo Shifted RASER (ES-RASER), which provides a tunable contrast level. It will be shown that although RASER has a fairly good resilience with respect to static field inhomogeneities, in some cases it suffers from a lack of sufficient contrast. This is because RASER is a spin echo sequence. If one uses 180° refocussing pulses, all susceptibility effects are refocused. However, when two voxels have more or less the same spin density ρ , and when their T_1 or T_2 relaxation times are not significantly different, susceptibility effects can provide a source of contrast. By shifting the echoes, (i.e. by starting to record the signal after the echo formation) we show how one may enhance contrast in RASER. The main experimental results are shown in Fig. 2.

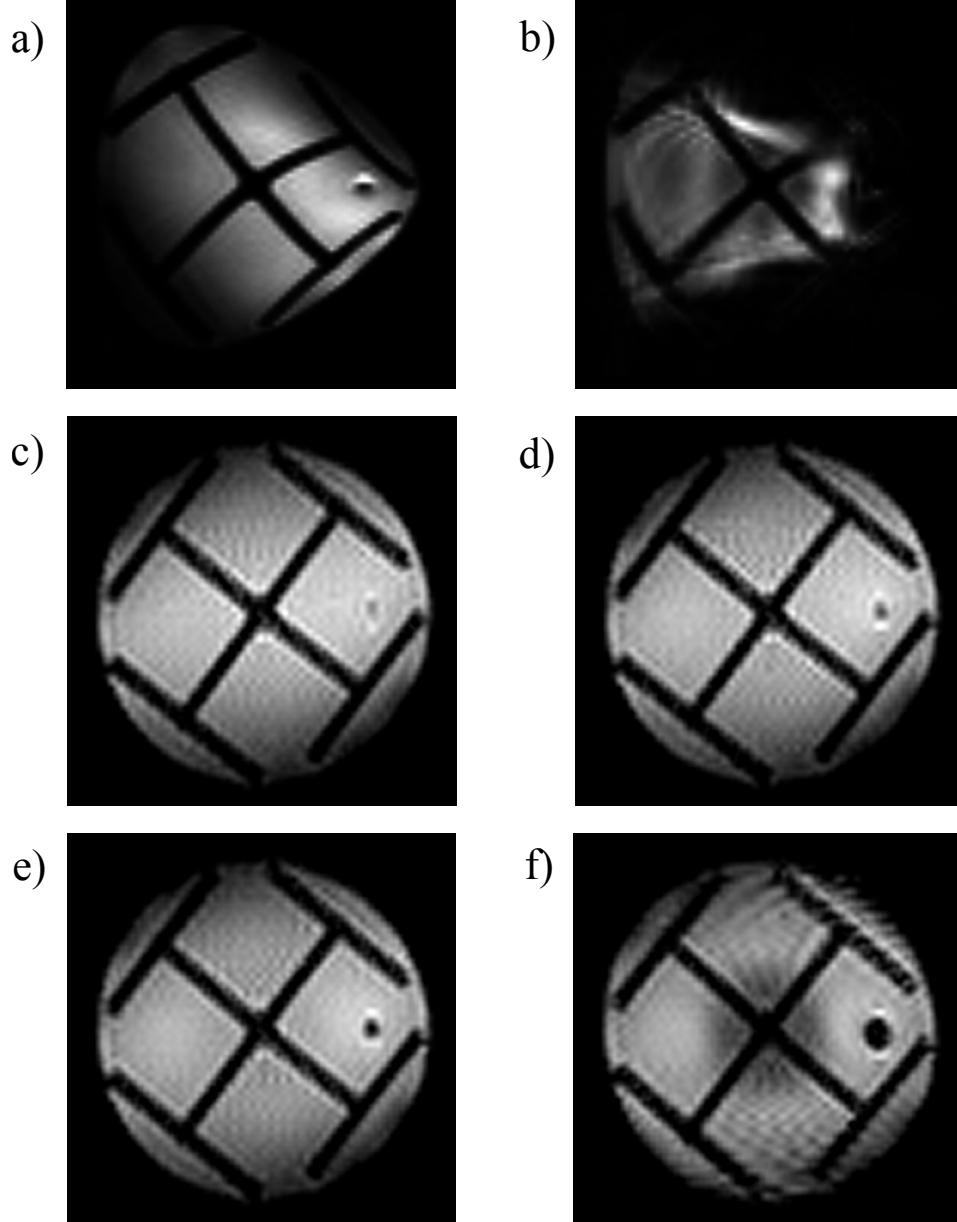


Figure 2: Summary of experimental results of the third chapter. (a) Conventional spin echo EPI, and (b) gradient echo EPI without any refocusing pulse, both with a matrix size 64×64 , FOV 27.0×27.0 mm, readout bandwidth 250 kHz, but with $TE = 45.8$ ms for (a) and $TE = 25.6$ ms for (b). (c), (d), (e), and (f) Echo Shifted (ES)-RASER, all with a matrix size 64×64 , FOV 27.0×27.0 mm, readout bandwidth of 250 kHz. (c) $TE = 46.0$ ms and $\xi = 0$ (the parameter ξ represents the extent of echo shifting, as will be discussed in chapter 3). Images (d) to (f) were obtained with decreasing TE and increasing ξ . (d) $TE = 43.8$ ms and $\xi = 0.1$. (e) $TE = 41.6$ ms and $\xi = 0.2$. (f) $TE = 30.7$ ms and $\xi = 0.7$.

The phantom shown in Fig. 2 comprises two parts, a cross-shaped piece of plastic immersed in water, and a thin glass fibre made by stretching a piece of molten glass heated in a flame (seen as black spots in Fig. 2d–f). As can be seen, EPI brings about distorted images in an inhomogeneous magnetic field. Although these distortions are absent in RASER (Fig. 2c), the contrast is not sufficient to reveal the existence of the small glass fibre. The effects of glass fibre can easily be seen in ES-RASER images (Fig. 2d–f), which are not distorted by the inhomogeneous static magnetic field.

One aspect of ES-RASER is that the extent of the echo shifting can be tuned by adjusting a so-called “mismatch parameter” ξ . We will show how the variation of ξ can help to obtain images with different contrast levels. Finally, using a series of images obtained with different mismatch parameters, we show how one can extract some informative maps that provide a pixel-by-pixel information about the relaxation parameters $\frac{1}{T_2^*(r)} = [\frac{1}{T_2(r)} + \frac{1}{T_2^{inh}(r)}]$ or $[\frac{1}{T_2^{inh}(r)} - \frac{1}{T_2(r)}]$. The results obtained in the third chapter have recently been published [7].

Forty years after its invention, echo planar imaging (EPI) is still one of the most popular single-scan MRI techniques [8, 9] and is widely used in functional imaging [14]. One drawback of this method is the need for closely spaced positive and negative gradients, which require very fast switching of gradients, making it a hardware-demanding method for MRI. Typically, gradient rise and fall times of about 100 μ s are required for this method [10]. More importantly, even if rapid switching between positive and negative gradients is technically feasible, the switching rate of the gradients needs to be limited for *in vivo* applications to avoid stimulating the patient’s nervous system [11].

The fourth chapter is dedicated to time-encoding [12, 13]. This is an imaging technique that is very similar to spatial encoding with the important difference that it uses a train of shaped selective pulses, while in spatial encoding a frequency-swept “chirp” pulse is used for spatial encoding. At the beginning of chapter 4, various available

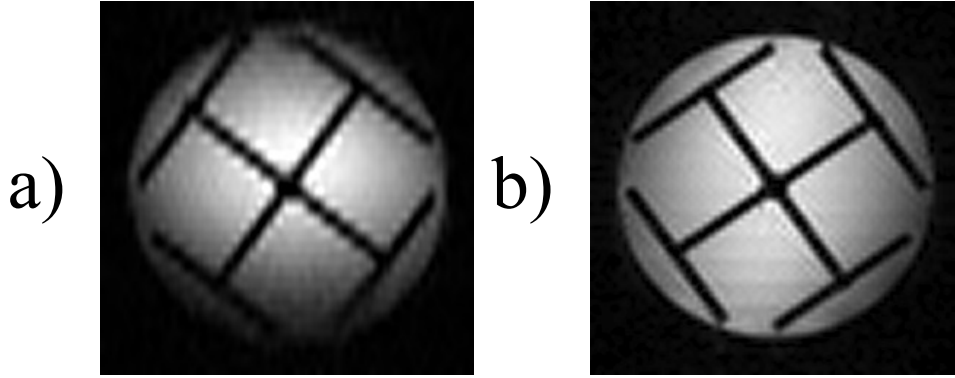


Figure 3: (a) Single-scan time-encoding image obtained by a modified time-encoding sequence (see Fig. 4.4b), with a matrix size of 32×64 (32 in time-encoding direction, and 64 in k -encoding direction), a FOV 27.0×27.0 mm, and $TE = 23.6$ ms. (b) The same as (a) obtained using a four-fold interleaving of the excitation frequencies, with a matrix size of 64×64 (16×64 for each of four scans), FOV 27.0×27.0 mm, and $TE = 12.4$ ms.

single-scan techniques with different switching rates are discussed. Afterwards, we discuss some modifications we have implemented to improve existing time-encoding sequence [12, 13]. By using an additional gradient we could change the order of the detection with respect to the original time-encoding sequence. This leads to identical echo times for all echoes, and hence to a uniform signal attenuation due to relaxation.

Time-encoding methods use long and intense gradients during both excitation and detection, and consequently they usually suffer from significant signal attenuation due to diffusion. It will be shown how implementing a time-encoding sequence in an interleaved fashion brings about a noteworthy reduction in signal attenuation due to diffusion. Fig. 3a shows an image obtained by a single-scan time-encoding sequence. The effects of signal attenuation that are due to diffusion can be seen at the bottom and the top. Fig. 3b on the other hand, was obtained by the same time-encoding sequence, but implemented in an interleaved fashion. Obviously signal attenuation due to diffusion is much less severe than before, albeit, at the cost of losing the advantages offered by a single-scan sequence. By continuing our modifications, it will be shown how one can modify the original time-encoding sequence to reduce the gradient switching rate. By

rearranging positive and negative gradients, one can reduce the switching rate of the gradients.

Since different excitation pulses with different excitation bandwidths can be used for time-encoding sequences, it is important to know the effects of different excitation pulses. These effects will also be experimentally investigated in the fourth chapter. Also the effect of having an overlap between selected spin-packets will be discussed. Moreover, it will be explained why careful adjustment of echo times in both readout and time-encoding directions is important for some modified versions of time-encoding.

Finally, this dissertation ends by recapitulating the main conclusions and by mentioning some perspectives for future research.

Chapter 1

An overview of magnetic resonance imaging

1.1 A short history of nuclear magnetic resonance

One has to be extremely careful when talking about the history of any scientific discovery. Scientific and technological advancements are all connected like pearls on a necklace, and of course it is difficult to cover the entire history of each individual pearl in the introduction of a PhD dissertation. It is even more difficult to highlight a specific scientific work among others, and credit it as “important” or “seminal”, etc., for they are all interdependent. Therefore, to avoid these difficulties, the history of MRI is reviewed here in simple chronological order. Obviously, a history represented in a few paragraphs cannot be exhaustive, and for a more comprehensive review the reader is referred to some references that are wholly dedicated to historical perspectives of Nuclear Magnetic Resonance [[15](#), [16](#), [17](#)].

In 1922, Stern and Gerlach proved experimentally that the angular momentum associated with silver atoms is spatially quantized. Later in 1924, Wolfgang Pauli

introduced a “bi-valued degree of freedom” in quantum theory to solve contradictions between observed molecular spectra and quantum theory. This “bi-valued degree of freedom” is nowadays known as spin $\frac{1}{2}$, associated with some particles. From a theoretical point of view, the intrinsic angular momentum exhibited by some particles can be explained by the relativistic quantum theory proposed by Paul Dirac in 1928.

In 1936 Cornelius J. Gorter published the results of his unfruitful attempt to detect nuclear magnetic spins [18]. Two years later, in 1938, Isidor I. Rabi and his co-workers observed nuclear magnetic resonance (the word was coined by Rabi) in a molecular beam of LiCl [19, 20]. In 1946, Felix Bloch, Edward Purcell and their co-workers independently published their results of the observation of nuclear magnetic resonance in bulk matter [21, 22, 23].

Since NMR is a resonance technique, for a few decades the usual way of studying a spin system was to put the system in a tuned *rf*-circuit located inside a variable magnetic field, and to pass through the resonance condition by varying the field while the frequency of the *rf*-circuit was kept constant. Although this method is still the main scheme for Electron Paramagnetic Resonance (EPR), the invention of Fourier NMR techniques by Richard Ernst was a turning point in NMR [24, 25]. In Fourier NMR, instead of passing the system through resonance conditions, one acquires a time-dependent signal irradiated from the sample upon excitation by an *rf*-pulse. In this method all resonance lines are acquired at the same time, and the Fourier transformation of the time-dependent signal brings about an NMR spectrum of the sample. Fourier NMR is important not only because it benefits from “Fellgett’s advantage”, but also because it enables one to design two-dimensional (2D) NMR [25, 26] experiments, which are essential tools to study large molecular systems.

1.2 Basic theory of nuclear magnetic resonance

1.2.1 Basic interactions

When a magnetic dipole (either a classical magnetic dipole like a macroscopic current loop or a quantum dipole like a proton) is placed in a magnetic field, it interacts with the field according to the following Hamiltonian¹:

$$H = -\vec{\mu} \cdot \vec{B}_0 \quad (1.1)$$

where \vec{B}_0 is the magnetic field vector, and $\vec{\mu}$ is the magnetic moment. The field also exerts a torque on the dipole given by:

$$\vec{T} = \vec{\mu} \times \vec{B}_0 \quad (1.2)$$

Since the magnetic moment of a system is proportional to its angular momentum Eq. 1.1 can also be rewritten as:

$$H = -\gamma \vec{J} \cdot \vec{B}_0 \quad (1.3)$$

where \vec{J} stands for the angular momentum of the system, and the coefficient γ is called gyromagnetic ratio, which has a constant value for each particle. Note that Eqs. 1.1-1.3 are valid for classical systems as well as for quantum systems. The nuclei of many atoms bear an inherent angular momentum or spin. When such nuclei are placed in a magnetic field, the degeneracy between different spin eigenstates will be lifted, so that different eigenstates will have a non-zero energy given by:

$$H = -\gamma \vec{B}_0 \cdot \vec{J} = -\gamma B_{z0} S_z = -\gamma \hbar B_{z0} I_z \Rightarrow E_m = -\gamma \hbar B_{z0} m \quad (1.4)$$

¹This interaction is often called Zeeman interaction.

where the magnetic field is chosen to be parallel to the z direction, B_{z0} and S_z are the z components of the magnetic field and spin operator respectively, \hbar is the Planck constant divided by 2π , and m is an integer or a half-integer representing different eigenstates of the operators S_z or I_z . Lifting the degeneracy leads to a population difference between the different eigenstates; and consequently, the sample will have a net macroscopic magnetization. At high temperatures ($kT \gg \gamma\hbar B_0$) it can be approximated by (Eq. 5.94 Ref. [27]):

$$M_z = \frac{\gamma^2 \hbar^2 I(I+1)}{3kT} B_0 \quad (1.5)$$

where M_z is the net macroscopic magnetization (per spin) at thermal equilibrium, I is the total spin number of the nucleus, k is the Boltzmann constant, and T is the absolute temperature. In continuous-wave (CW) methods, this magnetization causes a frequency-dependent impedance in the tuned rf -circuit, reflecting back an MR signal proportional to M_z . In pulsed techniques, an rf -pulse brings this magnetization in xy plane, where its precession produces an alternating voltage in the detection coil.

1.2.2 Chemical shifts, and spin-spin couplings

The Hamiltonian 1.1 can be used for an isolated spin located in a magnetic field. However, nuclear spins in a chemical compound are almost never isolated. In a molecule, the nuclei are surrounded by electrons, which have an uninterrupted motion. This motion produces a secondary magnetic field, because electrons have an electrical charge, and their motion produces an electrical current. Therefore, in a chemical compound the nuclei interact not only with the external magnetic field but also with the secondary magnetic field arising from their surrounding electron cloud. The external static magnetic field affects the electrons' motion, and the secondary magnetic field associated with it. The secondary magnetic field has often an opposite direction with respect to the external magnetic

field; i.e., the electron cloud surrounding a nucleus often acts like a “shield”. That is, the magnetic field sensed by a nucleus is often smaller than the external magnetic field. It turns out that this “shielding effect” is related to the density of the electron cloud, the denser the electron cloud the larger the shielding. For a nucleus positioned in an isotropic site the Hamiltonian is given by:

$$H = -\vec{\mu}(1 - \sigma) \cdot \vec{B}_0 \quad (1.6)$$

where σ is the shielding parameter, normally reported in ppm, and expresses the degree of shielding on each nucleus. In an anisotropic site, the shielding effects can be described by a 3×3 tensor. However, for liquids and gases, fast molecular rotation will average out all the anisotropies to zero. Therefore, in this case, the resonance frequency is determined only by the isotropic part of the shielding tensor σ , which is the average of the diagonal elements of the tensor. It worth mentioning that in liquids and gases, anisotropic effects can lead to relaxation, although the resonance frequency does not change.

Since σ is determined by the chemical environment, a specific nucleus shows different resonance frequencies in different chemical environments; this phenomenon is called chemical shift. It is extensively used for chemical analysis of different molecules. The chemical shift is usually reported in ppm as a relative quantity with respect to a reference. We have:

$$\delta = \frac{\nu_{sample} - \nu_{ref}}{\nu_{ref}} \quad (1.7)$$

where δ is the chemical shift, and ν_{sample} and ν_{ref} are the resonance frequencies of the sample and the reference respectively.

In addition to the aforementioned interactions, nuclear spins may interact via an “electron-mediated” interaction called spin-spin coupling, or J -coupling. This interaction

is described by the following Hamiltonian, and is responsible for line splitting in high-resolution NMR².

$$H_{J\text{-coupling}} = J\vec{S}_1 \cdot \vec{S}_2 \quad (1.8)$$

where J is the coupling constant (usually reported in Hz) and S_1 and S_2 are spin operators.

There are a variety of other interactions like dipole-dipole interactions, which result from a direct interaction between two nuclei, exactly like between two magnet bars; or quadrupolar interactions, which results from the interaction of the quadrupole moment of a nucleus with its surrounding electric field gradient. However, for our purpose only a basic knowledge of chemical shifts is sufficient.

1.2.3 Relaxation and Bloch equations

Using Eq. 1.2, it can be shown that a macroscopic magnetization (or the expectation value of a quantum mechanical spin operator) will undergo a precession around an external magnetic field. This precession is similar to the precession of a gyroscope, and its frequency, which is called the Larmor frequency, is given by $\omega_L = \gamma B_{z0}$. According to Faraday's law, precession of nuclear spins surrounded by a coil induces an alternating voltage in the coil, which is a common way to observe magnetic resonance. Fig. 1.1³ shows a page from Bloch's notebook, in which precession of spins with the Larmor frequency, and the alternating induced voltage are depicted. Felix Bloch published a paper in 1946 in which he described the "nuclear induction" phenomenon, by representing a set of equations explaining the properties of an NMR signal [21]. He distinguished between parallel and perpendicular components of the magnetization with respect to the magnetic

²Due to very wide peaks, it is difficult to observe J -couplings in solid-state NMR.

³This figure is courtesy of Allen D. Elster, adopted from: <http://mriquestions.com>

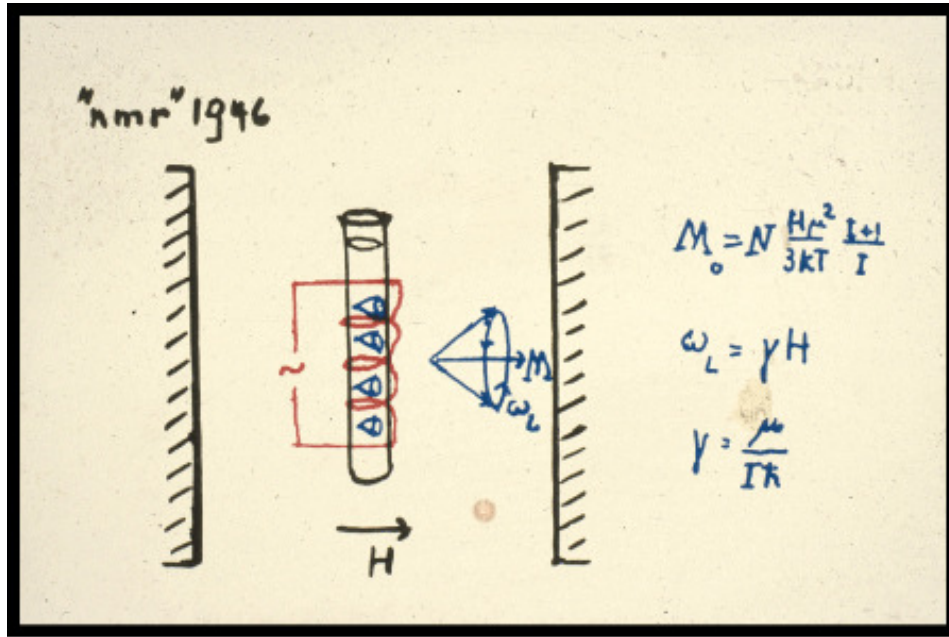


Figure 1.1: A page from Bloch's notebook representing precession of spins, and induction of a voltage in the surrounding coil. (source: courtesy of Allen D. Elster, adopted from: <http://mriquestions.com>)

field, by introducing two different relaxation times: the longitudinal relaxation time T_1 , that describes the rate by which the longitudinal component (parallel component) of the magnetization recovers to its thermal equilibrium; and the transverse relaxation time T_2 , characterising the rate at which the transverse components (perpendicular components) of the magnetization decay to zero. Using Eq. 1.2 and the aforesaid assumptions he derived the following equations called Bloch equations.

$$\frac{dM_x(t)}{dt} = \gamma \left(\vec{M}(t) \times \vec{B}(t) \right)_x - \frac{M_x(t)}{T_2} \quad (1.9a)$$

$$\frac{dM_y(t)}{dt} = \gamma \left(\vec{M}(t) \times \vec{B}(t) \right)_y - \frac{M_y(t)}{T_2} \quad (1.9b)$$

$$\frac{dM_z(t)}{dt} = \gamma \left(\vec{M}(t) \times \vec{B}(t) \right)_z - \frac{M_z(t) - M_0}{T_1} \quad (1.9c)$$

Using these equations one can describe the line shape of an NMR signal of a CW-NMR spectrometer in the steady-state conditions.

Both longitudinal and transverse relaxation processes play a fundamental role in MRI. If different tissues of body have different T_1 or T_2 , by adjusting the repetition time, TR , or the echo time, TE , it is in principle possible to distinguish between them. Many T_1 - and T_2 -weighted sequences have been developed because, each tissue may have a characteristic T_1 and T_2 , based on which it can be discerned from the others. Thus, by way of example, the pulse sequences called FLAIR (Fluid-Attenuated Inversion Recovery [28]) is based on the suppression of the fluid signals, by adjusting the inversion time, TI , so that signals from fluids that have a long T_1 are suppressed while the other parts of the body with a short T_1 are not.

1.3 A short history of magnetic resonance imaging

In 1952, Herman Carr used a magnetic field gradient to create a one-dimensional (1D) spectrum or image [29, 30]. In the Soviet Union, Vladislav Ivanov filed a document to the State Committee for Inventions and Discovery in Leningrad proposing that one may use magnetic resonance to study the interior parts of a human body [31], the idea which was approved in the 1970s. In 1971 Raymond Damadian, who was an associate professor of medicine at the State University of New York, used NMR relaxation times to distinguish between normal tissues and malignant tumours [32]. He demonstrated that cancerous cells have longer T_1 and T_2 relaxation times than normal cells [32]. Later in 1972 he filed a US patent entitled “Apparatus and method for detecting cancer in tissue” [33]. By 1977, he and his team could construct the first full-body MRI scanner, which was based on the “sensitive point” method [34]. Although the scanner was based on the main principles of NMR, it was more or less similar to CW-NMR machines. He used a saddle-shaped magnet which had a localizing property. Since the magnetic field of such a magnet is not homogeneous, only a small volume of spins located at the centre of the magnet are in resonance at any time. Under such conditions, the observed signal

exclusively comes from a small area of the body. To obtain the signal of whole body, the patient must be moved so that the scanner covers the whole body. Damadian called this method “field-focused NMR” [35, 36]. Later he incorporated the “FONAR” company, the first manufacturer of commercial MRI scanners. Because “field-focused NMR” was too slow, it was soon replaced by more recent imaging techniques.

1.3.1 Projectional magnetic resonance tomography

In 1973, Paul Lauterbur who was a chemist working at the State University of New York at Stony Brook published an MR image obtained by a method he named “zeugmatography” [37]. He placed two 1-mm-diameter tubes in a 1.4 T magnetic field. By applying a magnetic field gradient at different orientations, he recorded 1D NMR spectra at 4 different directions of a field gradient that was rotated in steps of 45° . The subsequent mathematical “back-projection”⁴ of the raw data leads to an MR image. In Greek “zeugma” means “what is used to join”, and the reason why Lauterbur named this method zeugmatography is that it depends on the joint effects of two magnetic fields. Shortly after, Lauterbur produced the first image of a living animal, a tiny clam [38].

1.3.2 Slice-selection and line-scanning

In 1973, Peter Mansfield, a physicist working at the University of Nottingham, used magnetic field gradients to localise an NMR signal [39, 40]. Later in collaboration with Andrew Maudsley he introduced a line-scanning technique [41]. Simultaneous application of a magnetic field gradient and an *rf*-pulse leads to selective excitation of a set of spins. One may use this idea for slice-selection (which is still being used in current MRI techniques), or one may use it for line-scanning. Using two perpendicular gradients

⁴In this case, the back-projection scheme is called inverse Radon transformation.

they could select a strip of spins inside the selected slice (a line⁵). Finally in 1977, by obtaining a 1D image of each line, and arranging all 1D images, they achieved the first MR image of a human body part [41].

1.3.3 Fourier NMR imaging and k -space

Applications of Fourier transformation in NMR were introduced by Richard Ernst in the 1960s. About one decade later Kumar, Welte, and Ernst showed how Fourier transformation can be exploited to form 2D or 3D MR images [42]. Their method was easy to implement, and compared to projectional tomography it required a simpler mathematical procedure for image reconstruction. Their method was developed later by Mansfield [9] and others, and soon became a universal MRI technique.

k -space

The term “ k -space” was introduced into the MRI literature by Liks in 1979 [43]. After further works of Ljunggren [44] and Twieg [45] in 1983 it became a widespread formalism in MRI. They have shown that the spin density $\rho(r)$, and the signal $S(k)$ (the signal as a function of the parameter k) form a Fourier pair. The parameter k defined by:

$$\vec{k} = \frac{\gamma}{2\pi} \int_0^t \vec{G}(t') dt' \quad (1.10)$$

Where $\vec{G}(t)$ is the magnetic field gradient. Neglecting the effects of relaxation, the time-dependence of an NMR signal obtained by a Fourier-based technique can be written as:

$$S(t) = \int \exp \left(i\gamma \vec{r} \cdot \int_0^t \vec{G}(t') dt' \right) \rho(\vec{r}) d\vec{r} \quad (1.11)$$

⁵The forth chapter of this dissertation is about a technique similar to line-scanning. In that concept the word “spin-packet” is used instead of “line”. In some references it is called “spin-isochromat” as well.

Replacing 1.10 into Eq. 1.11 gives:

$$S(\vec{k}) = \int \exp\left(i2\pi\vec{r}\cdot\vec{k}\right) \rho(\vec{r})d\vec{r} \quad (1.12)$$

From Eq. 1.12 it is obvious that $S(\vec{k})$ and $\rho(\vec{r})$ constitute a Fourier pair. As Eq. 1.12 implies, in Fourier-based MRI techniques, a signal $S(\vec{k})$ is sampled, then a subsequent Fourier transformation will convert $S(\vec{k})$ to $\rho(\vec{r})$ which amounts to the image. One difference between different Fourier techniques is the difference between their sampling method. In ordinary Fourier techniques each line of the k -space is sampled within one scan (one excitation), while in fast imaging techniques multiple lines per excitation are sampled. By way of examples, k -space trajectories for three different imaging methods are shown in Fig. 1.2. Currently, a variety of k -space trajectories are used in MRI; each of which has its pros and cons [5].

1.4 Non-Fourier MRI techniques

As we saw in the previous section, Fourier MRI techniques are based on the sampling of k -space in two or three dimensions followed by a Fourier transformation in all directions. Although none of the original MRI techniques like Lauterbur's projectional tomography technique or Mansfield's line-scanning technique, were fully Fourier techniques, nowadays Fourier techniques are prominent in MRI. These methods are well developed to exploit different phenomena such as T_1 relaxation, T_2 relaxation, diffusion, etc., as a source of information. There are plenty of Fourier-based pulse sequences each of which is suitable for a specific application. Non-Fourier techniques have been shown to have some essential advantages over Fourier methods. For example, in the case of large frequency variations, that is whenever the static magnetic field is not homogeneous or there are different chemical shifts in the object, single-scan hybrid imaging (to be explained in the next

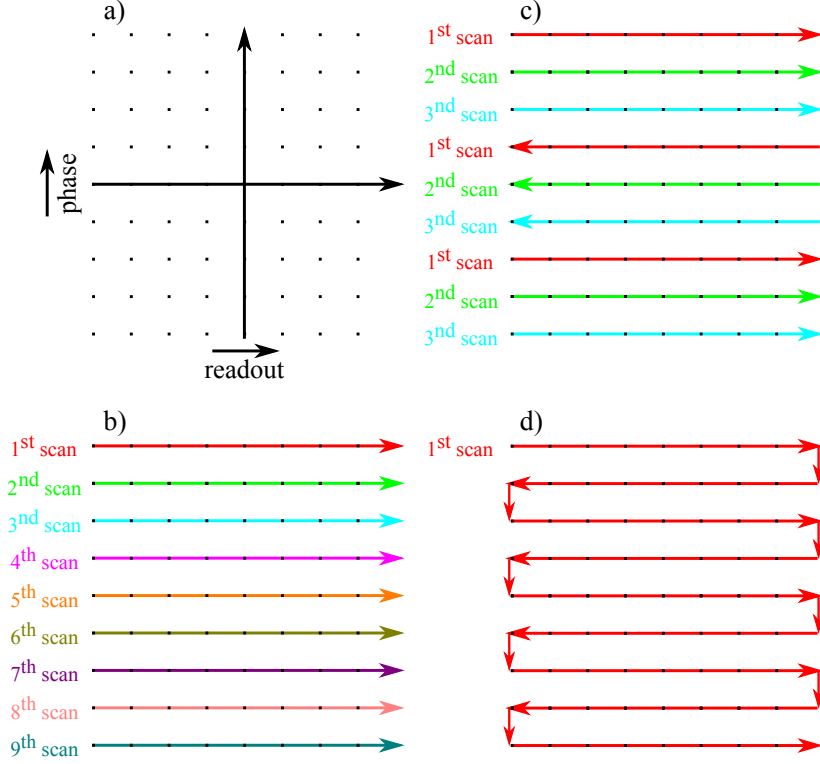


Figure 1.2: (a) A 2D k -space used in a typical Fourier MRI technique, which will be differently sampled in different methods. Different k -trajectories for (b) a gradient echo, (c) a fast spin echo (also known as turbo spin echo, or Rapid Acquisition with Refocused Echoes, RARE), and (d) an EPI sequence are shown. Different colours represents data sampled within different excitations. Note that in fast spin echo or EPI, the trajectories pass through $k_{\text{readout}} = 0$ several times for a given excitation; this means that in these methods multiple echoes are acquired in each excitation.

section) has been shown to be superior over traditional k -encoding techniques, bringing about images that are less distorted [46, 47].

1.4.1 Hybrid imaging techniques

We refer to Fourier methods as methods utilising the concept of Fourier MRI and k -space in all directions. Hybrid methods are a class of non-Fourier techniques that use k -encoding in one direction, and non-Fourier methods in the other direction. Although some techniques like Lauterbur's projectional tomography can be included in this category (projectional tomography uses a hybrid of Fourier and Radon transformations), in this

dissertation, only those methods that use k -encoding in one direction and time-encoding or spatial encoding in the other will be called hybrid techniques. The main idea behind time-encoding [12] and spatial encoding [48] is almost the same, and these names have sometimes been used interchangeably in the MRI literature; in addition spatial encoding is sometimes referred to as SPatiotemporal ENcoding or SPEN [1, 2]. The main idea of both methods is the localisation of the MR signal to a small part of the sample, either by spin-packet-selective pulses or by frequency-swept “chirp” pulses. In the following chapters of this dissertation some aspects of hybrid imaging techniques will be discussed. To be precise, henceforth in this dissertation, those hybrid techniques that use spin-packet-selective pulses are referred to as time-encoding, and those methods that use frequency-swept chirp pulses are called spatial encoding. Also, the term “spatiotemporal encoding” will be used to refer to common aspects of time-encoding and spatial encoding.

Since most of this dissertation is about hybrid techniques, they deserve a more detailed discussion. The key point about spatiotemporal techniques can be understood by inspection of Fig. 1.3. For the sake of simplicity, we limit ourselves here to a 1D problem, however the idea can be generalised to 2D and 3D. Fig. 1.3a represent a 1D spin density and a typical MR signal obtained by a k -encoding method. In Fourier techniques the signal bears no resemblance to the spin density (the object), since they are related by a Fourier transformation. In contrast to Fourier techniques in which the MR signal and the object are not similar at all, the signal acquisition in spatiotemporal encoding methods is done in such a way that there is a one-to-one correspondence between the signal intensity (usually as function of time) and spin density as a function of position. Such a correspondence is demonstrated in Fig. 1.3b. Spatiotemporal methods exploit suitable techniques to localise the MR signal into a small part of the image. For example, in Fig. 1.3b the signal intensity observed at the instant t_1 is almost exclusively coming from spins of the spin-packet located at X_1 . Obviously, no Fourier transformation is

required to reconstruct an image from such a signal, since the signal intensity itself looks like the object.

In hybrid imaging techniques, one may use another space instead of k -space, which can be tentatively called “hybrid space”. A schematic picture of such a space is depicted in Fig. 1.4. This space has the units of the parameter k (m^{-1}) in one direction, and the units of real space (m) in the other direction, and it can be converted into an image by a 1D Fourier transformation. Since the signal in the spatiotemporal encoding direction obtained by hybrid techniques is localised in a small part of the object, in this direction the signal intensity itself looks like the object, and no transformation is required.

Time-encoding

Time-encoding is a single-scan MRI technique introduced by Meyerand and her colleagues in the 90s [49, 12, 50, 51, 13]. Time-encoding is a hybrid single MRI technique that uses traditional k -encoding only in one direction. The second direction is encoded in time. That is, in the time-encoding direction, the echo time for each echo depends on the position of the corresponding spin-packet. Later in 1995, they introduced a variant⁶ of hybrid time-encoding technique [12], which was in fact a type of line-scanning, as proposed by Mansfield [41]. They used a series of selective pulses (which they called plane-selective pulses, and here they are called spin-packet-selective pulses) to excite the sample, followed by a 180° refocusing pulse, which leads to a train of echoes. Since each spin-packet-selective pulse excites a narrow spin-packet, each echo corresponds to a specific spin-packet.

Although the original time-encoding sequence [12] suffers from non-homogeneous T_2 -weighting for different spin-packets, it is less sensitive to field inhomogeneities, and also less vulnerable to motional artefacts, hence, each line has a localised signal so artefacts

⁶In this dissertation the time-encoding sequence introduced in the reference [12] is referred to as the original time-encoding sequence.

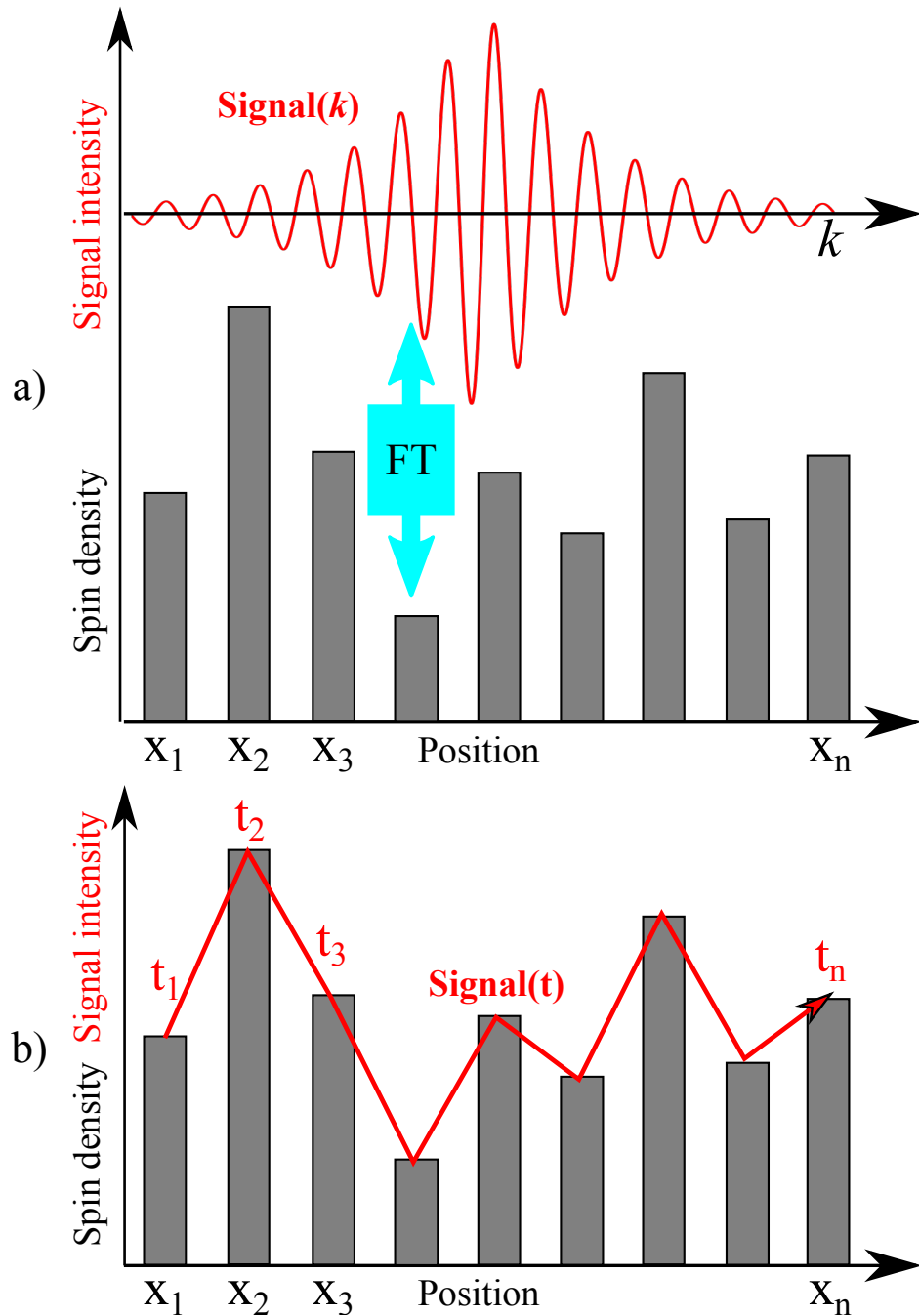


Figure 1.3: (a) A 1D spin density divided into neighbouring spin-packets, and the corresponding MR signal obtained by a traditional k -encoding techniques. To convert the signal into an image one needs a Fourier transformation. (b) The same spin density as in (a), with the corresponding MR signal obtained by a spatiotemporal MRI technique, showing the one-to-one correspondence between the signal intensity $S(t)$, and spin density $\rho(X)$.

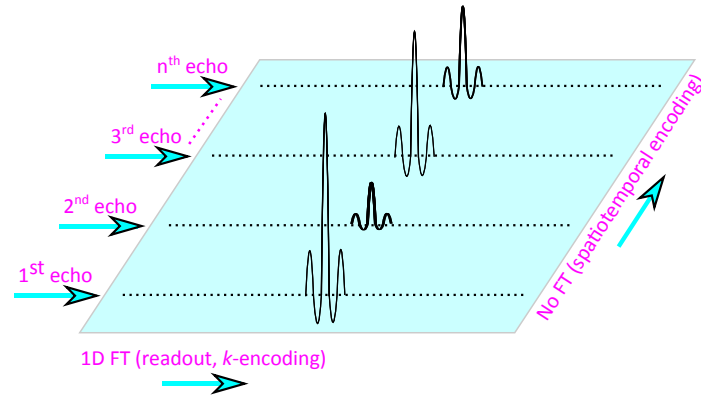


Figure 1.4: A schematic representation of hybrid space used in hybrid imaging techniques, comprising two directions, one with the units of the parameter k (m^{-1}), and the other with the units of normal space (m). Spatiotemporal techniques lead to localised echoes (in the spatiotemporal direction), each of which corresponds to a small part of the object. A Fourier transformation of each echo results in a small image (normally a small line in the object). These small images are put together to produce a complete 2D image of the object.

cannot spread out to the whole image [13]. In Fourier methods on the other hand, each point in k -space corresponds to the whole image, and as a result artefacts easily spread out to the whole image. Meyerand’s time-encoding sequence, and some modification leading to uniformly T_2 -weighted images, will be discussed in detail in the fourth chapter of this dissertation.

Spatial encoding

Another method to localise an MR signal is to simultaneously apply a frequency-swept pulse and a magnetic field gradient. In 1994, Pipe could obtain a 1D image without using any Fourier transformation by simultaneous application of a frequency-swept rf -pulse and a magnetic field gradient. The combination of an rf -pulse and a gradient leads to a quadratic phase profile where almost the entire signal stems from the vertex of the quadratic profile (i.e., from the flat region of the quadratic profile) [48, 52]. Applying a field gradient will allow one to move the vertex of the quadratic profile in order to obtain the signal from the region of interest. Pipe called this method spatial encoding since the

spatial information of the spin density is directly encoded into the signal. The idea of using frequency-swept *rf*-pulses for spatial encoding has been extended to hybrid MRI by Frydman and co-workers [1, 2, 46, 47, 53, 54, 55]. As mentioned above, these single-scan imaging methods are superior over customary *k*-encoding techniques in inhomogeneous magnetic fields, since their images are less distorted [47, 55]. Garwood and colleagues also have adapted these methods [3, 56]; their hybrid imaging method called Rapid Acquisition by Sequential Excitation and Refocusing (RASER) brings about uniformly T_2 -weighted images, since the echo time, TE , is the same for all points, in contrast to traditional *k*-encoding single-scan techniques in which each echo has a different echo time. In the second chapter we will discuss the effects of molecular diffusion in RASER, and in the third chapter we show how one can modify RASER to enhance the contrast.

Signal localisation in spatial encoding

As mentioned above, in time-encoding, signal localisation is done by applying a train of spin-packet-selective pulses. However, in spatial encoding, signal localisation is slightly different. An MR signal constitutes from in-plane-magnetizations of all parts of the sample. If different parts of the object have different phases, they cancel out each others, reducing the signal. In other words, phase variations of the in-plane-magnetizations diminish the signal. In spatial encoding the idea is to impose a position-dependent phase on the sample so that there is a steep phase variations across the entire object except than a small region of interest. In the region of interest phase varies very smoothly. In such conditions, the signal almost exclusively stems only from those parts that have a smooth phase variations; the signal of the other parts vanish. By applying field gradients, this region of interest is moved during the data acquisition so that the signal of the entire object is acquired.

Signal-to-noise ratio in spatiotemporal encoding

In general, spatial encoding techniques result in a smaller SNR compared to k -encoding methods. In spatial encoding the signal of each row along the spatiotemporal encoding direction of the hybrid space stems only from the part of interest in the object, while the remaining parts do not give any significant contribution to the signal. In k -encoding methods, on the other hand, each row along the phase-encoding direction of the k -space stems from the entire sample. Assuming that all parameters that affect the SNR are kept the same, the relation $\text{SNR}_{SPEN} = \frac{\text{SNR}_k}{\sqrt{N}}$ holds between the signal-to-noise ratio of a k -encoding method (SNR_k) that yields N pixels in the phase-encoding direction and of a spatiotemporal encoding method (SNR_{SPEN}) that provides N pixels in the spatiotemporal encoding direction [51].

Spatial resolution in spatiotemporal encoding

In time-encoding techniques, the localisation of the signal is achieved by a train of spin-packet-selective pulses. Consequently, the resolution in the time-encoding direction is equal to the thickness of the selected spin-packets:

$$\Delta x = \frac{b_w}{\gamma G_{te}} \quad (1.13)$$

where Δx is the thickness of the voxel, b_w is the bandwidth of the spin-packet-selective pulse, and G_{te} is the time-encoding gradient (for more information refer to chapter 4). In spatial encoding however, the spatial resolution is more complicated, and requires an exhaustive investigation [54, 57]. It turns out that the spatial resolution is given by:

$$\Delta x = C \frac{\text{FOV}_{SPEN}}{\sqrt{R}} \quad (1.14)$$

where FOV_{SPEN} is the field of view in the spatial encoding direction, $R = b_w \tau$ is a dimensionless parameter given by the product of the bandwidth of the chirp pulse (b_w) and its duration (τ), and C is a constant [54, 57].

Image artefacts in single-scan hybrid imaging techniques

One of the differences between traditional single-scan k -encoding and single-scan hybrid imaging methods is that hybrid techniques do not suffer from a notorious artefact called Nyquist $\frac{N}{2}$ ghost. Such an artefact can be seen in Fig. 1.5c. The acquisition block in single-scan k -encoding sequences (e.g., EPI) contains an alternating readout gradient, which results in a train of echoes. In an ideal situation the even and odd echoes exactly coincide, and the time interval between two consecutive echoes in the free induction decay (FID) is the same. Such a situation is depicted in Fig. 1.5a. In a real case however, a small mis-setting, e.g., a small asymmetry between positive and negative gradients or even a small delay before the start of the first echo will propagate to all following echoes. Such a situation is depicted in Fig. 1.5b. Fourier transformation of a k -space like in Fig. 1.5b brings about a Nyquist $\frac{N}{2}$ ghost. In fact, in the phase-encoding direction of Fig. 1.5b there are three types of signal modulation. First, all even and odd echoes are modulated. The modulation period in this case is equal to the distance between two consecutive rows in k -space. Such a modulation leads to the main non-aliased image that appears in the centre if the FOV is appropriately adjusted. Moreover, all even echoes, and similarly all odd echoes are modulated. This modulation of even and odd echoes results in two aliased half-images at the top and the bottom of the image.

In hybrid methods however, there is no Nyquist $\frac{N}{2}$ ghost, because, as it was explained above, artefacts are caused by performing a Fourier transformation on imperfect data. Obviously, if one does not apply any Fourier transformation (like in the

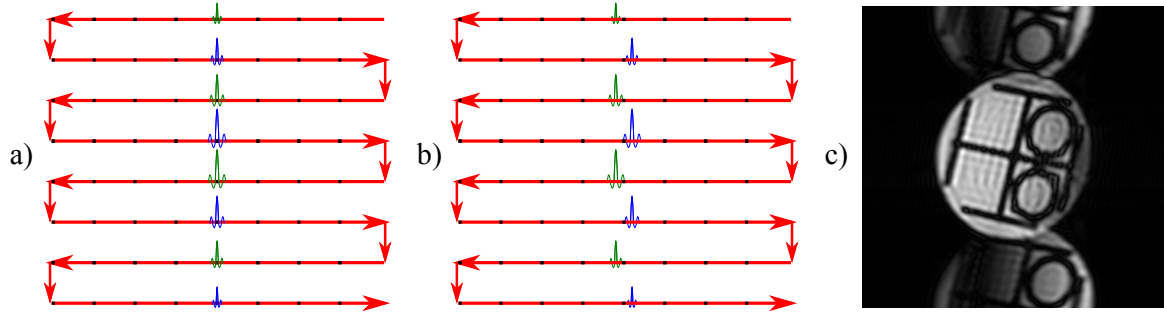


Figure 1.5: (a) A typical k -space obtained by an ideal EPI sequence, where all even and odd echoes coincide. (b) A typical k -space obtained in a real EPI sequence where even and odd echoes do not exactly coincide. Note that the even and odd echoes are represented by different colours. (c) An EPI image with Nyquist $\frac{N}{2}$ ghosts at the top and the bottom of the image.

spatiotemporal encoding direction in hybrid imaging methods) no Nyquist $\frac{N}{2}$ artefacts occur in the images.

Another difference between hybrid techniques and traditional k -encoding methods is that in hybrid techniques there is no aliasing (hence no wrap-around artefacts) in the spatiotemporal encoding direction [12]. This is again because, in spatiotemporal encoding no Fourier transformation is performed in the spatiotemporal encoding direction. Aliasing occurs only when one applies a Fourier transformation to data that are not sampled at an appropriate sampling rate, consequently, wrap-around artefacts are absent if one does not use any Fourier transformation. Therefore, in the case that one is only interested in some small parts of the object, spatiotemporal encoding methods can be used without any need for anti-aliasing techniques. This is not the case in traditional k -encoding methods, in which the image is folded back (wrap-around artefacts) if the object is larger than the FOV. Note that in k -encoding methods using digital filtering techniques, one can easily filter out all the unwanted signals in the readout direction, whereas in the phase-encoded direction one has to apply more complicated anti-aliasing techniques, like the pre-saturation of the unwanted regions.

1.4.2 Cross-encoding

In 2009, Paquin and his colleagues introduced a sequence that uses spatial encoding in both directions [58]. It is called cross-encoding because in this method the x gradient is used to encode the y direction, and vice versa. Since it uses spatial encoding for both directions, to obtain a 2D image, no Fourier transformation (in any direction) is required in this method. Cross-encoding, and similar techniques like xSPEN have exceptional resilience with respect to field inhomogeneities, making them a promising candidate for imaging in presence of metallic implants [55, 59].

With this basic theory of spatiotemporal encoding represented in this section, we are ready to investigate different aspects of spatiotemporal encoding methods. This will be done in the next three chapters.

Chapter 2

The effects of diffusion in spatially encoded magnetic resonance imaging

2.1 Diffusion: a short introduction

The concept of diffusion has been used in different fields of research such as chemistry, physics, biology, engineering, economics, and even sociology. In physical science diffusion is a process by which the particles of a system intermingle with each other. It can happen in gases, in liquids, and even in solids [60]. One must clearly distinguish between bulk flow and diffusion, which are two entirely different phenomena. Although the motions of particles are responsible for both phenomena, the former occurs when the particles collectively move due to a macroscopic force (usually caused by a pressure gradient) exerted on a very large number of particles in bulk, while the latter is due to Brownian motions of the particles, and does not require any external force. In this chapter diffusion is introduced first, and then its effects on spatially encoded MRI will be discussed.

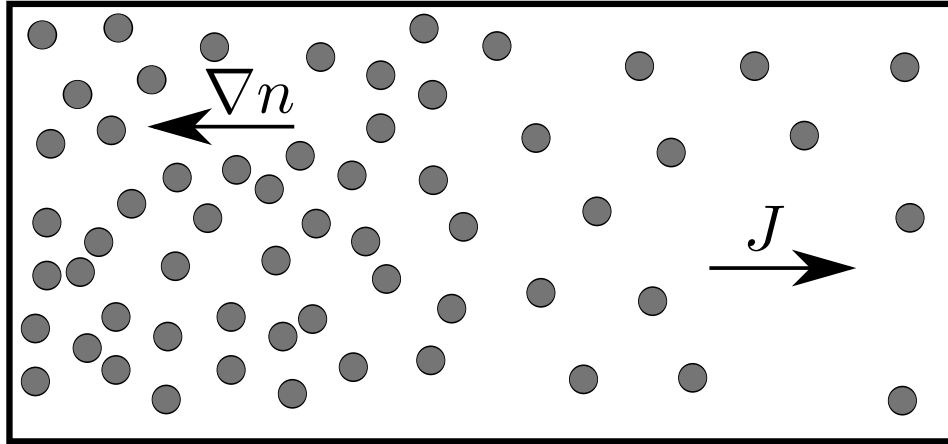


Figure 2.1: The flow of the particles from a dense area towards a dilute area.

2.1.1 Fick's laws

Let us imagine that we have some particles that are distributed non-uniformly in a medium which does not completely hinder their motion. An example of such a situation is an inhomogeneous solution in which the concentration of the solute is not the same everywhere. In this case, as depicted in Fig. 2.1, there would be a net flow of the particles from the area with higher concentration towards the area with lower concentration. This net flow will continue until there is no concentration difference in our medium. Adolf Fick investigated diffusion in such a case, and presented his results in 1885 [61]. According to Fick's first law this flow is given by:

$$J = -D\nabla n(r, t) \quad (2.1)$$

where J is the flow, $n(r, t)$ is the concentration as a function of the position r and time t , and D is called the diffusion coefficient. Obviously, in any diffusion process the total number of particles must be conserved, that is the rate of concentration change, $\frac{\partial n}{\partial t}$, and the divergence of the flux must fulfil the following conservation law:

$$\nabla \cdot J + \frac{\partial n}{\partial t} = 0 \quad (2.2)$$

replacing Eq. 2.1 in Eq. 2.2 brings about the diffusion equation, also known as Fick's second law:

$$\frac{\partial n(r, t)}{\partial t} = D \nabla^2 n(r, t) \quad (2.3)$$

Fick had a phenomenological approach to the diffusion problem. As mentioned above, the first idea was developed to describe the diffusion of some solute particles non-uniformly dissolved in a solvent. Such a phenomenon is called mutual diffusion, hence as the solute particles flow in one direction, the solvent particles have to flow in the opposite direction to keep the total density constant. For a system composed of identical particles we can replace $n(r, t)$ by $p(r, t)$ which is the local probability of finding a particle at position r at time t . If we assume that although $p(r, t)$ is macroscopically uniform, it can have some local non-uniformities, we can still apply Fick's laws for $p(r, t)$. Of course $p(r, t)$ is more general than $n(r, t)$, and can be used either for a system which is composed of identical particles or for a system composed of different particles. Self-diffusion refers to the situation in which some identical particles move and intermingle with each others as a result of their random motions due to their thermal energy. Albert Einstein explained this case, and derived the following expression for D :

$$D = \mu k_B T \quad (2.4)$$

Where μ is the mobility of the particles, which is the ratio of the particle's drift velocity to an applied force. Eq. 2.4 is called Stokes-Einstein, or Einstein-Smoluchowski, or sometimes Sutherland-Einstein relation as it was revealed by William Sutherland in 1904 [62, 63], by Albert Einstein in 1905 [64], and by Marian Smoluchowski in 1906 [65].

2.1.2 Unrestricted diffusion

Since $p(r, t)$ is interpreted as the probability of finding a particle at a position r at time t , it can be written as:

$$p(r', t) = \int p(r, 0)P(r|r', t)dr \quad (2.5)$$

where $P(r|r', t)$ is the conditional probability of finding a particle at the position r' , and time t provided that it is at position r at the time 0. Since, $p(r', t)$ obeys Fick's law regardless of the initial distribution $p(r, 0)$, it follows that $P(r|r', t)$ also obeys Fick's law. Therefore we have:

$$\frac{\partial P(r|r', t)}{\partial t} = D\nabla^2 P(r|r', t) \quad (2.6)$$

If the original distribution of particles at $t = 0$ is a point distribution, that is if $P(r|r', 0) = \delta(r' - r)$, and if the diffusion takes place in a container whose walls are located at infinity, the solution of Eq. 2.5 would be a Gaussian function:

$$P(r|r', t) = (4\pi Dt)^{-\frac{3}{2}} \exp\left(-\frac{(r' - r)^2}{4Dt}\right) \quad (2.7)$$

The solution 2.7 is only valid for the case that the diffusing particles never reach the boundaries of the container. Such a case is called unrestricted diffusion. Restricted diffusion is another case in which the diffusing particles hit the walls of the container (or any other hard barrier), and are reflected back.

2.1.3 The effects of diffusion on NMR signals

The effect of molecular diffusion on NMR signals has been widely studied [66]. In 1950 E. L. Hahn realised that to explain the attenuation of spin echoes in some samples, the

effects of diffusion of the molecules through an inhomogeneous magnetic field has to be taken into account [67]. Later in 1954, using random walk theory, H. Y. Carr and E. M. Purcell reformulated Hahn's analysis, and obtained a relation similar to what H. C. Torrey obtained two years later [68]. In 1956 Torrey combined Bloch's and diffusion equations, and obtained the following equation connecting the attenuation of the signal for a spin echo formed in an inhomogeneous magnetic field [69].

$$S = S_0 \exp\left(-\frac{2}{3}D\gamma^2G^2\tau^3\right) \quad (2.8)$$

where S_0 is the initial signal intensity, S is the signal intensity at the peak of the echo, D is the diffusion constant, γ is the gyromagnetic ratio, G is the magnetic field gradient, and τ is the time interval between the excitation and the 180° pulse (or between the 180° pulse and the echo), as shown in Fig. 2.2a. In most NMR experiments, two short pulsed gradients, symmetrically positioned on both sides of a 180° pulse, are applied instead of a long constant gradient. The first pulsed field gradient (PFG) de-phases the magnetization which will be re-phased by another PFG. Such a situation is depicted in Fig. 2.2b. In this case the signal intensity is given by:

$$S = S_0 \exp\left(-D\gamma^2G^2\tau^2\left(\Delta - \frac{\delta}{3}\right)\right) \quad (2.9)$$

where δ is the length of the pulsed field gradients, and Δ is the time interval between the two gradient pulses. Fig. 2.2a is a special case of Fig. 2.2b, in which $\Delta = \delta = \tau$. Replacing these values in Eq. 2.9 leads to Eq. 2.8, as expected.

2.1.4 Restricted diffusion, and apparent diffusion coefficient

Eq. 2.7 is valid for isotropic media whose boundaries are located at infinity. Most real systems studied by MR techniques however, are restricted and anisotropic, and often

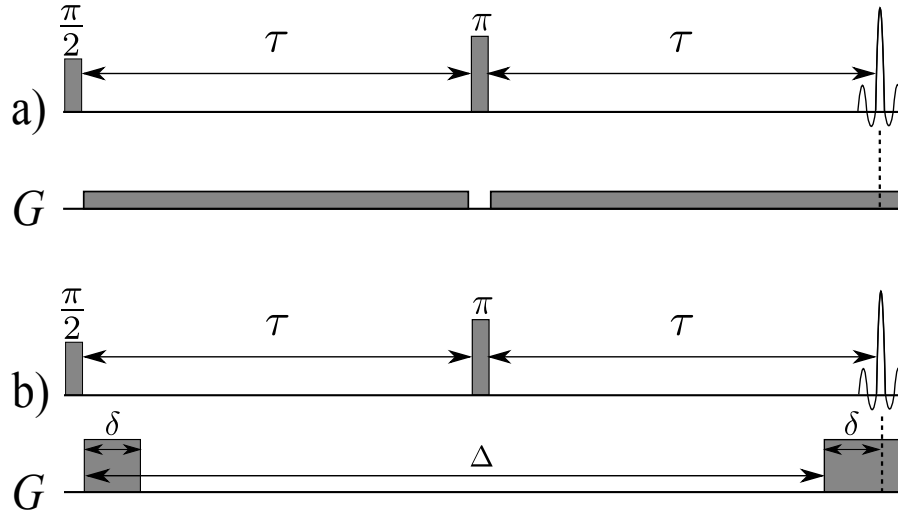


Figure 2.2: (a) Formation of an echo using a continuous magnetic field gradient (or in an inhomogeneous magnetic field), and (b) echo formation using two pulsed field gradients. G represents the pulsed field gradient (or the static inhomogeneity), τ is the time interval between the 90° and 180° pulses (or equivalently between the 180° pulse and the echo), δ is the length of pulsed field gradients, and Δ is the time interval between the beginning of the two gradient pulses.

can contain different parts with different spatially-dependent diffusion coefficients. In order to take into account the anisotropy, i.e., the existence of different diffusion rates along different directions, a diffusion tensor must be defined instead of a single diffusion coefficient D , which is as follows:

$$\begin{bmatrix} D_{xx} & D_{xy} & D_{xz} \\ D_{yx} & D_{yy} & D_{yz} \\ D_{zx} & D_{zy} & D_{zz} \end{bmatrix} \quad (2.10)$$

Diagonal elements of the diffusion tensor, represent the diffusion coefficients measured along the three principle axes. The off-diagonal terms represent the correlation between the random motions along each pair of axes. By dint of MR techniques, diffusion tensor

can be assessed by applying a field gradient along different axes¹, and by measuring the signal attenuation. In real systems there are a lot of factors that can cause signal attenuation, like susceptibility effects, flow, bulk movement of the spins, to name only a few. The effects of these factors are difficult to assess, and usually the signal attenuation is entirely attributed to diffusion effects. Therefore, the observed diffusion coefficients are usually called apparent diffusion coefficients, abbreviated by ADC.²

2.2 Levelling the effects of molecular diffusion in spatially encoded magnetic resonance imaging

2.2.1 Introduction

A general introduction about hybrid imaging techniques is presented in the previous chapter, and is not repeated here. In 2007, Chamberlain et al. introduced an imaging method dubbed Rapid Acquisition by Sequential Excitation and Refocusing (RASER) [3]. They extended the concept of spatial encoding to achieve a uniform weighting by T_2 relaxation, but did not address the issue of weighting by diffusion. Translational diffusion leads to irreversible losses in signal intensity in the presence of magnetic field gradients. Ideally if the diffusion coefficient D is not position-dependent, the attenuation of the signal $S(r)$ of a voxel $\Delta V(r)$ should not explicitly depend on the position r . In other words, the pulse sequence, must faithfully reflect local properties (like $D(r)$, $T_1(r)$, $T_2(r)$, etc.) of the spin density to the signal, and the pulse sequence itself, must not non-uniformly weight the signals of different area of the object.

¹Among nine elements of the diffusion tensor, only six elements are independent. Therefore, in order to be able to measure them, one needs to apply magnetic field gradients along at least six non-collinear directions.

²In magnetic resonance texts the term “ADC” also refers to “Analogue-to-Digital Converter” which is a piece of hardware used for data acquisition in almost all modern digital instruments, and must be distinguished from Apparent Diffusion Coefficient.

In this chapter we will show that in spatial encoding, the diffusional loss of the signal $S(r)$ may depend on the coordinate r of the voxel $\Delta V(r)$. In spatial encoding the duration of de- and re-phasing intervals can be position-dependent, and may not necessarily be the same for all coordinates r ; therefore, the signal attenuation due to diffusion may be position-dependent as well. This position-dependent signal attenuation due to diffusion may act as a source of information. For example, it has been used in single-scan diffusion-ordered NMR spectroscopy [70, 71, 72, 73]. However, in MRI it mostly acts as an artefact. In the RASER experiment, as our experimental results confirm, the marginal voxels will be more severely attenuated than those in the centre, even if the diffusion coefficients is the same for all the voxels. The experiment evaluated in this chapter (DC-RASER) can compensate for this drawback, and provide images in which the attenuation of the signal $S(r)$ due to diffusion does not depend on the coordinate.

2.2.2 Theory

Attenuation of signals by homogeneous T_2 relaxation

Homogeneous T_2 relaxation, and inhomogeneous T_2^* effects must be in general distinguished, because the latter can be refocused using 180° pulses to form spin echoes, while the former are irreversible. In addition, molecular diffusion through an inhomogeneous magnetic field causes signal losses that cannot be refocused. In traditional Fourier methods which acquire more than one echo per excitation (e.g., EPI), different data points in k -space suffer to a different extent from homogeneous T_2 , and inhomogeneous T_2^* effects. As shown by Constable, this can result in signal loss and blurring of the image [74]. In traditional Fourier techniques T_2 and T_2^* effects depend only on the local values of T_2 and T_2^* . In these methods the signal and the image form a Fourier pair, and consequently each point in k -space contains signals of the entire object.

In spatial encoding techniques, on the other hand, signals $S(r)$ corresponding to different areas of the object can be encoded and decoded at different moments. Therefore, the signal loss due to $T_2(r)$ and $T_2^*(r)$ will be larger for points that are encoded earlier or decoded later, since the signal intensity depends on the interval between excitation and detection. Thus, in contrast to traditional k -encoded methods, one may observe different losses for two voxels that have the same $T_2(r)$ and $T_2^*(r)$. This can be crucially problematic when homogeneous T_2 relaxation is fast or when T_2^* is short, i.e., when the field is very inhomogeneous.

RASER is a hybrid technique which uses spatial encoding in one dimension, and k -space encoding in the other, and leads to uniformly T_2 -weighted images. In spatial encoding, different parts of the object are excited sequentially by simultaneous application of a gradient and a frequency-swept chirp pulse. In 2010, Frydman and co-workers [47] discussed various spatially encoded pulse sequences, with an emphasis on effects of inhomogeneous magnetic fields, in this chapter we demonstrate how diffusion can cause a misleading contrast in spatially encoded imaging. The original RASER pulse programme is depicted in Fig. 2.3, and Fig. 2.4 shows the pulse sequence we have used, which leads to images that are uniformly weighted by both T_2 and diffusion effects. Fig. 2.4 has been adapted from a previously reported work [46], by using shaped 180° pulses for slice-selection. The latter method is referred to as “double-chirp RASER”, abbreviated by DC-RASER. Both RASER and DC-RASER sequences bring about uniformly T_2 -weighted images. In addition, in both sequences the excitation is done by applying a long chirp pulse (usually as long as a few tens of milliseconds) in which the frequency is linearly swept. By adjusting the amplitude of the rf -pulse, different nutation angles (in our experiments 90°) can be achieved, in which the equilibrium magnetization M_z is transformed into transverse magnetization M_{xy} by an rf -pulse that deliberately violates the condition for adiabatic sweeps. We refer to such pulse as a 90° excitation chirp pulse.

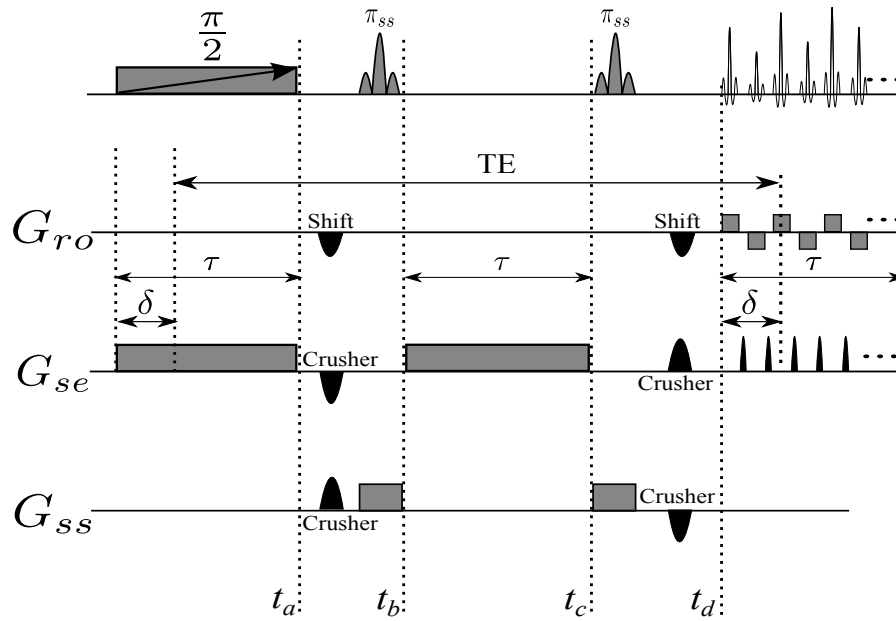


Figure 2.3: RASER pulse programme. The Frequency-swept chirp pulse with a WURST amplitude profile is represented by a grey box with an sloping arrow. Shaped inversion pulses are labelled by π_{ss} . The gradients G_{ro} , G_{se} and G_{ss} are used for readout, spatial encoding and slice-selection, respectively. Crusher gradients cause irreversible de-phasing of the magnetization. Shift gradients have the effect of shifting the echoes to the centre of k -space. TE is the echo time, τ is the duration of the chirp pulse, and δ is the time at which an arbitrary voxel is excited by the chirp pulse. Experimental values for the parameters are given in the caption to Fig. 2.7.

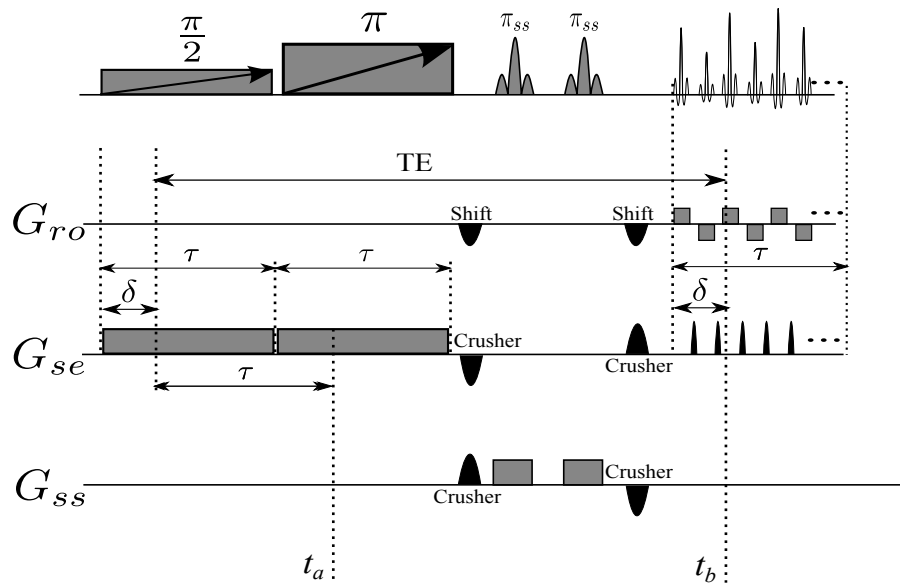


Figure 2.4: DC-RASER pulse programme. The Frequency-swept chirp pulses with a WURST amplitude profiles are represented by grey boxes with sloping arrows. Shaped inversion pulses are labelled by π_{ss} . Like RASER, the gradients G_{ro} , G_{se} and G_{ss} are used for readout, spatial encoding and slice-selection, respectively. Crusher gradients cause irreversible de-phasing of the magnetization. Shift gradients have the effect of shifting the echoes to the centre of k -space. TE is the echo time, τ is the duration of the chirp pulse, and δ is the time at which an arbitrary voxel is excited. Experimental values for the parameters are given in the caption to Fig. 2.7.

34 The effects of diffusion in spatially encoded magnetic resonance imaging

When a gradient is applied during a chirp pulse, different voxels are excited by the pulse at different moments. If the order of detection is the same as the order in which the magnetization has been excited, the interval between excitation and detection is the same for all the voxels, provided that the acquisition time is equal to the length of the excitation pulse (τ in Fig. 2.3), which is the case for both RASER and DC-RASER. The outcome of such a sequence will therefore be a uniformly T_2 -weighted image. As long as diffusion effects are negligible, the two methods of Fig. 2.3 and Fig. 2.4 lead to similar images. The resulting quadratic phase profile has been described analytically by Pipe [48, 52]. Without loss of generality, we shall assume that the spatial encoding gradient G_{se} is applied along the y direction. The profile of the phase of the magnetization excited by an excitation chirp pulse of duration τ with a linear frequency sweep from $-\frac{b_w}{2}$ to $\frac{b_w}{2}$ where b_w is the bandwidth or the total range of frequencies swept by the pulse is given by:

$$\phi_{90} = -\frac{R}{8} + \frac{R}{2}Y - \frac{R}{2}Y^2 \quad (2.11)$$

where Y is the dimensionless normalized y -coordinate defined as $Y = \frac{y}{L}$ in which $L = \frac{b_w}{\gamma G_{se}}$ is the total length (in meters) covered by the chirp pulse, and R is the localizing factor given by $R = b_w \tau$. The larger the parameter R , the better the spatial resolution, since the area from which the signal is stemming becomes narrower when R increases. Similarly, after an inversion by a frequency-swept 180° (adiabatic) pulse, the phase of the in-plane-magnetization as a function of Y is given by:

$$\phi_{180} = -\frac{R}{4} - RY^2 \quad (2.12)$$

Using Eqs. 2.11 and 2.12, and considering the fact that a 180° pulse inverts the signs of all phases, one can deduce the phase profiles resulting from the basic RASER and DC-RASER pulse sequences. At different moments t_a , t_b , t_c and t_d in the basic RASER

sequence we have the following phases:

$$\phi_a = -\frac{R}{8} + \frac{R}{2}Y - \frac{R}{2}Y^2 \quad (2.13a)$$

$$\phi_b = -\phi_a = \frac{R}{8} - \frac{R}{2}Y + \frac{R}{2}Y^2 \quad (2.13b)$$

$$\phi_c = \phi_b + \gamma G \tau y = \phi_b + RY = \frac{R}{8} + \frac{R}{2}Y + \frac{R}{2}Y^2 \quad (2.13c)$$

$$\phi_d = -\phi_c = -\frac{R}{8} - \frac{R}{2}Y - \frac{R}{2}Y^2 \quad (2.13d)$$

while for DC-RASER we have:

$$\phi_a = -\frac{R}{8} + \frac{R}{2}Y - \frac{R}{2}Y^2 \quad (2.14a)$$

$$\phi_b = -\phi_a + \phi_{180} = \frac{R}{8} - \frac{R}{2}Y + \frac{R}{2}Y^2 - \frac{R}{4} - RY^2 \quad (2.14b)$$

$$= -\frac{R}{8} - \frac{R}{2}Y - \frac{R}{2}Y^2 \quad (2.14c)$$

as can be seen from Eqs. 2.13d and 2.14c, the phase profiles of both basic RASER and DC-RASER sequences are the same, therefore, as long as effects of diffusion through the field gradients can be neglected the same image is expected from both sequences.

Effects of inhomogeneous fields

In order to take into account the effects of inhomogeneous magnetic field, in the phase profile equation of both sequences, the term $\omega = \gamma G_{se}y$ must be replaced by $\omega = \gamma G_{se}y + \omega_{inh}$, where ω_{inh} is the offset frequency (in $\frac{rad}{s}$ units) caused by the field inhomogeneities³. Therefore Eqs. 2.13d and 2.14c can be rewritten as:

$$\phi = -\frac{R}{8} - \frac{R}{2}Y' - \frac{R}{2}Y'^2 \quad (2.15)$$

³Here, ω_{inh} refers to a frequency variation regardless its source. Therefore, our arguments can be generalised to the other cases. For example at the presence of more than one chemical shift.

36 The effects of diffusion in spatially encoded magnetic resonance imaging

In Eq. 2.15 $Y' = Y + Y_{inh}$ where $Y_{inh} = \frac{\omega_{inh}}{\gamma G_{se} L}$. Therefore, an inhomogeneous magnetic field causes a pixel displacement or image distortion, because, the point which is supposed to appear at Y in a homogeneous field will appear at $Y' = Y + Y_{inh}$ in an inhomogeneous field. This image distortion is given by $Y_{inh} = \frac{\omega_{inh}}{\gamma G_{se} L}$, which is proportional to ω_{inh} , and consequently, the larger the field inhomogeneities the larger the image distortion, as it is expected. It is also inversely proportional to G_{se} , i.e., the larger the spatial encoding gradient, the smaller the image distortion caused by the inhomogeneous field. Although in spatial encoding sequences, it is possible to use a large spatial encoding gradient to suppress the image distortions, one cannot use a very large spatial encoding gradient, as the signal attenuation due to diffusion associated with a long spatial encoding gradient can be very large. An inhomogeneous magnetic field causes some image distortions in the k -encoding as well. However, often these distortions can be effectively suppressed using a large readout bandwidth (large readout gradient).

Effects of diffusion

Both sequences in Figs. 2.3 and 2.4 are affected by diffusion through a magnetic field gradient. The influence of diffusion during application of frequency-swept pulses in the presence of gradients has been studied by Giraudeau and Akoka [75, 76], and by Shrot and Frydman [72]. To understand the role of diffusion we divide the sequences into intervals τ where the magnetization is either being de-phased or re-phased. In such a case the signal loss at the end of each complete de- and re-phasing interval is given by Eq. 2.8. In the case of n consecutive de- and re-phasing intervals, as in sequences with multiple refocusing, we will have⁴:

$$S = S_0 \prod_{j=1}^n \exp\left(-\frac{2}{3} D \gamma^2 G_j^2 \tau_j^3\right) \quad (2.16)$$

⁴Eqs. 2.8 and 2.16 are valid for diffusion through a constant gradient only. If pulsed gradient are used these equations have to be modified.

Using Eqs. 2.8 and 2.16, the signal loss due to diffusion for the basic RASER sequence is:

$$S = S_0 \exp\left(-\frac{2}{3}D\gamma^2 G_{se}^2 [(\tau - \delta)^3 + \delta^3]\right) \quad (2.17)$$

While for the DC-RASER sequence, the signal attenuation is:

$$S = S_0 \exp\left(-\frac{2}{3}D\gamma^2 G_{se}^2 \tau^3\right) \quad (2.18)$$

where τ is the duration of each chirp pulse, and $\delta = (\frac{y}{L} + \frac{1}{2})\tau$ is the time at which the chirp pulse hits the magnetization of a voxel at the coordinate y . Fig. 2.5 illustrates the de- and re-phasing stages in both of the sequences. We have assumed that the gradients that act during signal acquisition are continuous, while in practice a train of short “blips” has been used. The deviations caused by this approximation are negligible⁵. Eqs. 2.17 and 2.18 show that the losses due to diffusion in the DC-RASER sequence do not depend on δ , while in the basic RASER they do. In the latter case, the loss is worst for $\delta = 0$ or $\delta = \tau$. For DC-RASER, the loss due to diffusion is always equal to the maximum loss in the basic RASER experiment, but it is uniform over the entire object, whereas the signal loss in the basic RASER depends on the spatial coordinates, which gives rise to a misleading contrast. This non-uniform signal loss is not limited to RASER, and can be observed in other spatially encoded sequences as well.

2.2.3 Experimental

All experiments were performed on a Bruker 800 MHz NMR spectrometer equipped with micro-imaging facilities. In order to verify the accuracy of Eq. 2.17, two sets of different

⁵Since the total area of the blips is the same as the area of a constant spatial encoding gradient, at the end of each blip, the phase profiles of the experiments using a constant gradient and the experiment using a train of blips are exactly the same, and Eqs. 2.17 and 2.18 are exactly valid at the end of each blip. Therefore, they only differ in a short period between two successive blips, which is not significant.

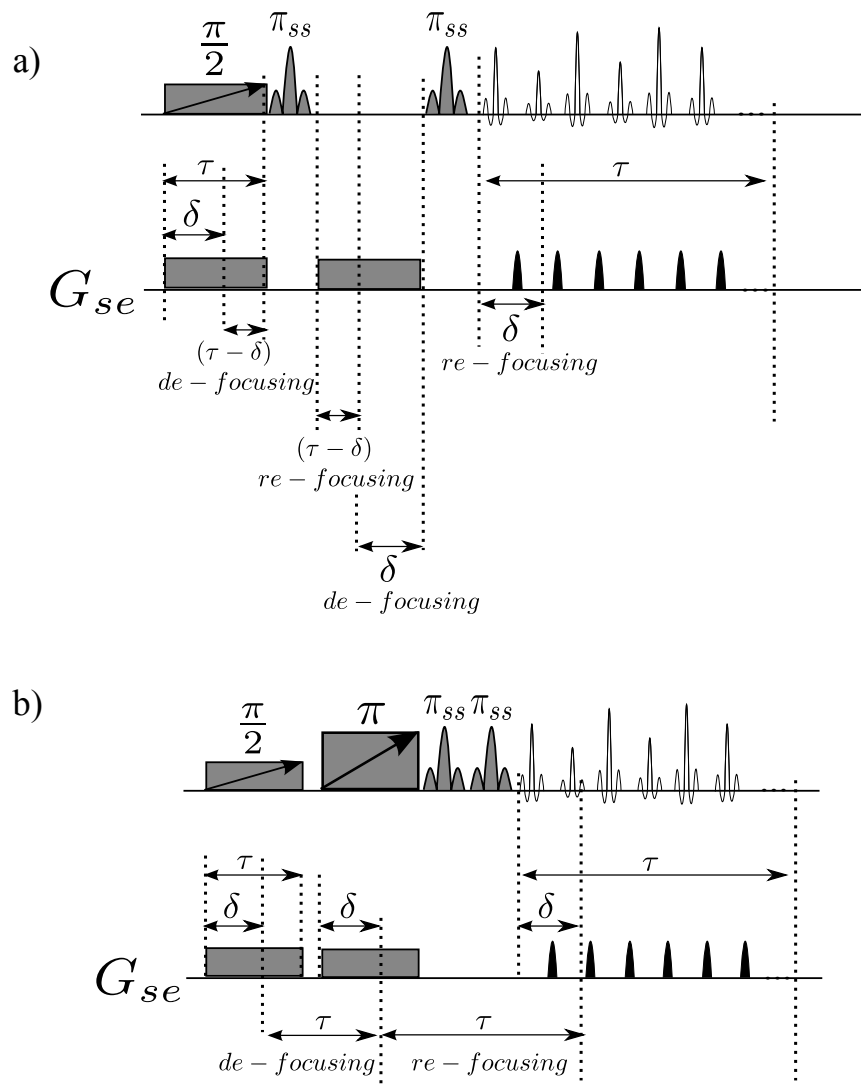
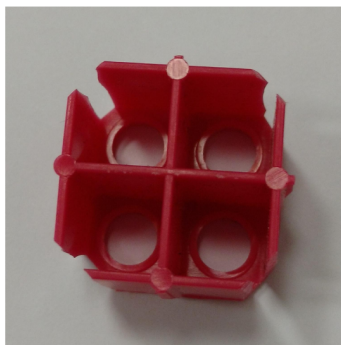


Figure 2.5: Intervals where de-phasing and re-phasing of magnetization occurs under the spatial encoding gradients G_{se} in the sequences of Figs. 2.3 and 2.4 for (a) RASER, and (b) DC-RASER.

experiments were performed. In the first set of experiments, different values of G_{se} were used, and in the second set the variable parameter was D .

Experiments with variable spatial encoding gradients

In the first set of experiments, by using an imaging probe with an internal diameter of 2.5 cm we performed RASER and DC-RASER with different values of G_{se} . The phantom was a cross-shaped piece of plastic inserted into a glass tube, and immersed in de-ionized water. This phantom is shown in Fig. 2.6. For the sake of comparison, a standard multi-shot k -encoded spin echo image [5] and a spin echo EPI image [8, 9] were obtained with the Paravision programme (the standard programme used in many Bruker MRI instruments). For the other images, the pulse programme were implemented in the Topspin programme (the standard Bruker programme used in Bruker NMR instruments) and the resulting signals were processed using a home-written Python code. In all cases, a field of view (FOV) of 27.0×27.0 mm, a matrix size of 64×64 points, and a slice thickness of about 1mm were used. In both basic RASER and DC-RASER sequences, frequency-swept chirp pulses [77] with “apodized” amplitudes of WURST pulses [78] (which provides a smoother excitation and inversion profile) have been used. In these pulses, the frequency of the rf -pulse is swept between two predefined values to excite a wide range of frequencies. Simultaneous application of a chirp pulse and a gradient leads to sequential excitation of different voxels, which is the key idea of spatial encoding. In order to compare the efficiency of different single-scan sequences, i.e., EPI, basic RASER, and DC-RASER, three different images were recorded in a magnetic field in which the homogeneity was deliberately degraded by mis-setting the currents of the $x^2 - y^2$ and x shim coils. Proton spectra of the entire phantom are depicted on top of Fig. 2.7, which approximately represent the extent of the magnetic field inhomogeneity.



z direction

Figure 2.6: Top view of a cross-shaped piece of plastic used as a phantom in this chapter, and in the following chapters. In all figures an “axial” image of this phantom is depicted. The z direction is chosen to be into the plane.

Variable temperature experiments

In order to verify the results obtained in the first set of experiments, a new set of experiments were performed at different temperatures, leading to different diffusion coefficients. Since our imaging probe did not support variable temperature, these experiments were performed on a liquid-state 5 mm NMR probe equipped with three orthogonal field gradients. The phantom was a 5mm NMR tube filled with de-ionized water. At each temperature, two images were recorded using the sequences shown in Figs. 2.9a and b. Please note that these multi-scan sequences were designed specifically to investigate the effects of diffusion in RASER and DC-RASER sequences, and totally differ from single-scan RASER and DC-RASER. In fact for them the spatial encoding and readout directions are the same, and an image can be obtained either by performing a 2DFT on the raw data, or by performing only a 1DFT on the phase-encoding direction. This is because the phase profiles resulting from these sequences in the readout direction are similar to the phase profiles of RASER (or DC-RASER) in spatial encoding direction. Of course if one wants to use 2DFT, the Nyquist criterion for data sampling must be fulfilled.

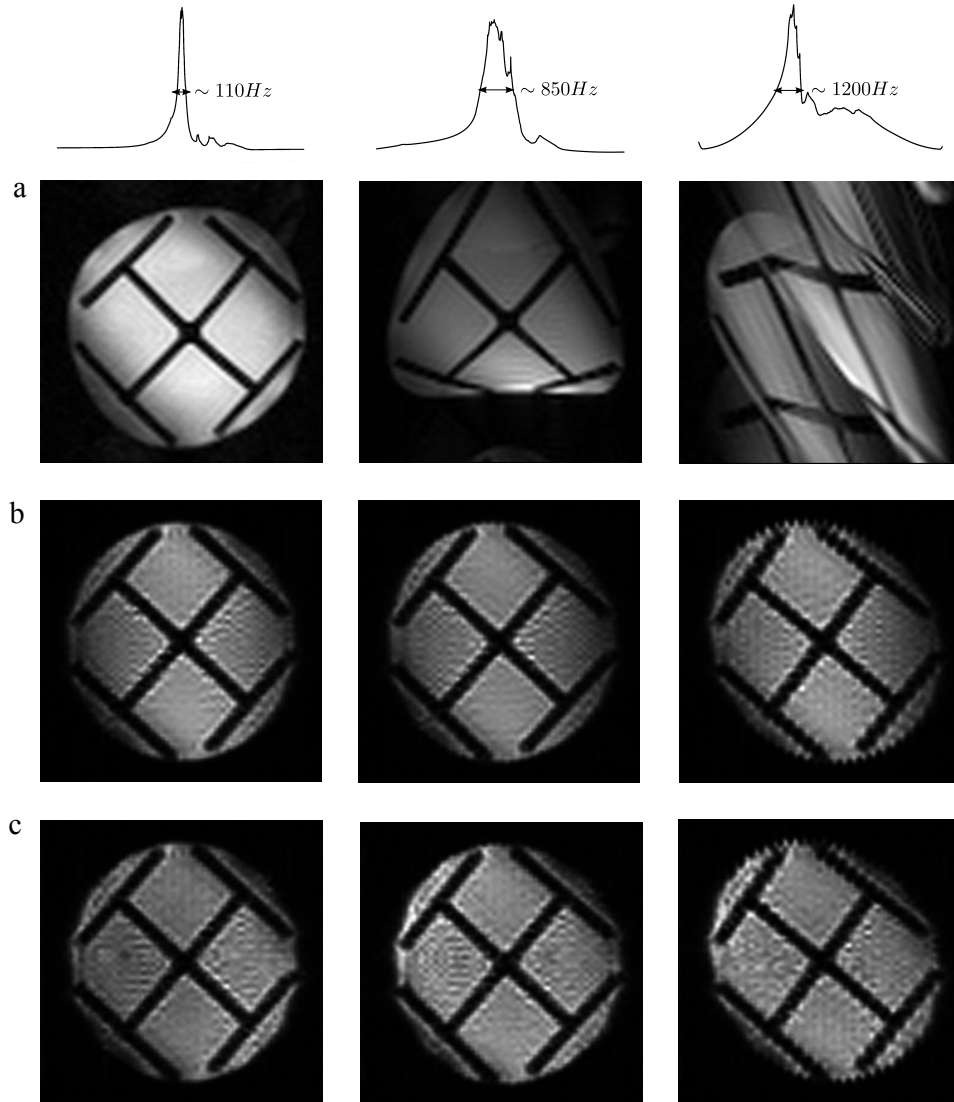


Figure 2.7: Images obtained at 800 MHz of a phantom consisting of a cross-shaped piece of plastic immersed in de-ionized water in a tube of 25 mm diameter. From left to right: effects of increasing inhomogeneity of the static field, as seen from the proton spectra of the entire phantom shown along the top. Top row: spin echo EPI obtained with an $\text{FOV} = 27.0 \times 27.0$ mm, matrix size = 64×64 , bandwidth = 250 kHz, $TE = 24.44$ ms. Middle row: RASER, $\text{FOV} = 27.0 \times 27.0$ mm, matrix size = 64×64 , bandwidth 250 kHz in the readout direction, Wurst chirp pulse, $\tau_{chirp} = 21.8$ ms, $G_{se} = 0.035$ T/m, $TE = 46.0$ ms, total acquisition time = 67.8 ms. Bottom row: DC-RASER, with the same parameters as in RASER. The slice thickness was about 1 mm in all images.

2.2.4 Results and discussion

Experimental results: different values for spatial encoding gradients

The top row of the Fig. 2.7 depicts spin echo EPI images of our phantom. It is obvious from these images that the inhomogeneity of the static field has a deleterious effect on the image quality. In the (horizontal) phase-encoding dimension the areas of the blip gradient pulses must be small enough to fulfil the Nyquist theorem. The inhomogeneities of the static field can only be neglected if they are much smaller than averaged blip gradients⁶. The distortions are less severe in the (vertical) readout direction, where one can take advantage of fast digitizers and high sampling rates, and of gradients that are strong enough to mask static field inhomogeneities.

For spatially encoded methods, however, the effects of the inhomogeneities are different. Since there is no need for a Fourier transformation in the spatially encoded dimension, there are no limits imposed by the Nyquist theorem. Consequently, for a given acquisition time one can apply much stronger gradient pulses than in traditional k -encoded methods. This makes it possible to mask the effects of field inhomogeneities. The second row of Fig. 2.7 shows basic RASER images. These experiments are quite robust with respect to inhomogeneous static fields, and give rise to images of higher quality than EPI when the field is not homogeneous, but the effects of diffusion are not uniform. In Fig. 2.7 (second row), the central pixels are brighter than the pixels near the right and left edges. The central pixels correspond to $\delta = \frac{\tau}{2}$, the left pixels to $\delta = 0$, and the right pixels to $\delta = \tau$. In agreement with Eq. 2.17, the signal losses due to diffusion are most pronounced near the edges. To visualize this effect, colour maps are shown in Fig. 2.8. Cross-sections (blue lines) corresponding to the average signal intensity of the two middle rows of the 64×64 matrix were plotted along the top. In contrast to

⁶Averaged value of blip gradients equals to the total area of the blip gradients divided by the acquisition time.

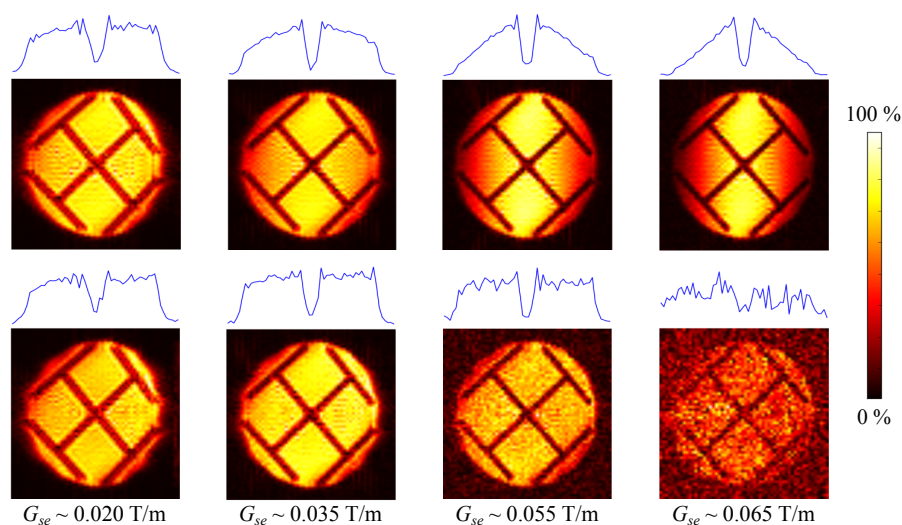


Figure 2.8: Colour-coded maps corresponding to Fig. 2.7, obtained with (top row) the RASER sequence, and (bottom row) DC-RASER, with spatial encoding gradient amplitudes G_{se} increasing from left to right. The inhomogeneity of the static field was the same as in the central column of Fig. 2.7, the width of the proton signal being 850 Hz. The maximum intensity in each image has been normalized to 100 percent.

basic RASER, DC-RASER gives rise to a flat profile, as can be seen in Figs. 2.7 and 2.8, confirming that signal losses due to diffusion are uniform over the entire sample. The remaining slight attenuation in signal intensity near the edges can be attributed to rf -inhomogeneity. This deviation from a perfectly flat profile is also observed in the reference images, and should thus not be ascribed to limitations of either DC-RASER or basic RASER methods.

As can be seen in Fig. 2.8, the larger the gradients, the greater the losses due to diffusion, and the lower the signal intensity. Moreover, in basic RASER images, the stronger the spatially encoding gradients, the larger the misleading differences in signal intensity between the centre and the edges of the image (as is evident from the blue lines on the top of the colour-coded maps). This confirms our discussion of the role of diffusion. Note that when the pulsed field gradients are stronger, spatially encoded methods are less sensitive to inhomogeneities. For the basic RASER sequence, the

stronger the applied gradients, the better one compensates for internal gradients, but the worse the misleading contrast due to diffusion. On average, the diffusion losses are smaller for basic RASER than for DC-RASER, as can be seen from Eqs. 2.17 and 2.18. For DC-RASER, the losses are equal to, but never worse than the maximum signal losses in the basic RASER method. For a correct interpretation of the signal intensity in basic RASER images, one has to keep the role of diffusion in mind, otherwise these losses may be mistakenly attributed to apparent spatial variations of spin density $\rho(r)$, spatial variations of homogeneous $\frac{1}{T_2}(r)$ relaxation rates, or spatial variations of the diffusion coefficients $D(r)$ in different parts of the object. In DC-RASER images, on the other hand, the contrast only stem from genuine local differences of these parameters.

Experimental results: different diffusion coefficients

Fig. 2.10 represents the images of our phantom (a 5mm NMR tube in this case) with four different diffusion coefficients obtained by adjusting the temperature to four different values. The left column corresponds to the sequence shown in Fig. 2.9a, and the right column corresponds to Fig. 2.9b. All images obtained by multi-scan sequences, and are phase-encoded in a usual manner. Both sequences shown in Figs. 2.9a and b have the same behaviour in the phase-encoding direction (vertical direction in the image). However in the spatial encoding direction (horizontal direction in the image) they are different. It is evident that for low temperatures (for small diffusion coefficients) the two sequences are more or less the same. This is because, as mentioned before both sequences have the same phase profile. Therefore, if the effects of diffusion are negligible, as it is the case if the diffusion coefficient is small, both sequences must give rise to the same images. However, for higher temperatures (larger diffusion coefficients) the left column behaves like RASER, while the right column behaves likes DC-RASER. Such a behaviour is expected from Eqs. 2.17, and 2.18, which confirms our previous results as well.

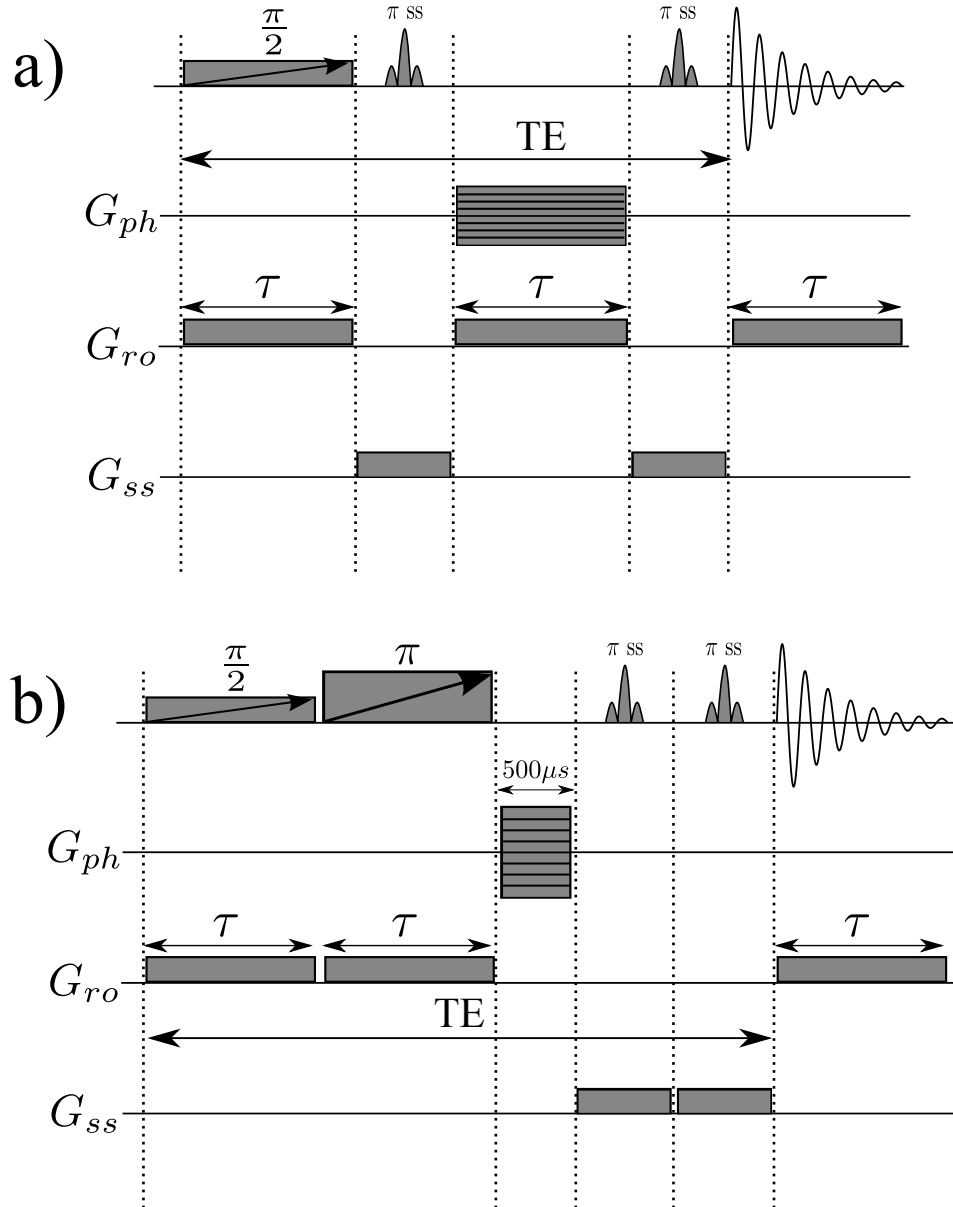


Figure 2.9: The pulse programmes used in the variable temperature experiments. (a) A multi-scan sequence used to investigate diffusion effects in RASER. (b) A multi-scan pulse programme used to investigate the effect of diffusion in DC-RASER. Frequency-swept chirp pulses with WURST profiles are represented by grey boxes with sloping arrows. Note that in these sequences the readout and spatial encoding directions are the same, and the second direction is phase-encoded in a usual manner. Although the phase-encoding gradients do not have the same length their amplitude have been adjusted so that they have the same integral. The experimental parameters are given in the caption to Fig. 2.10.

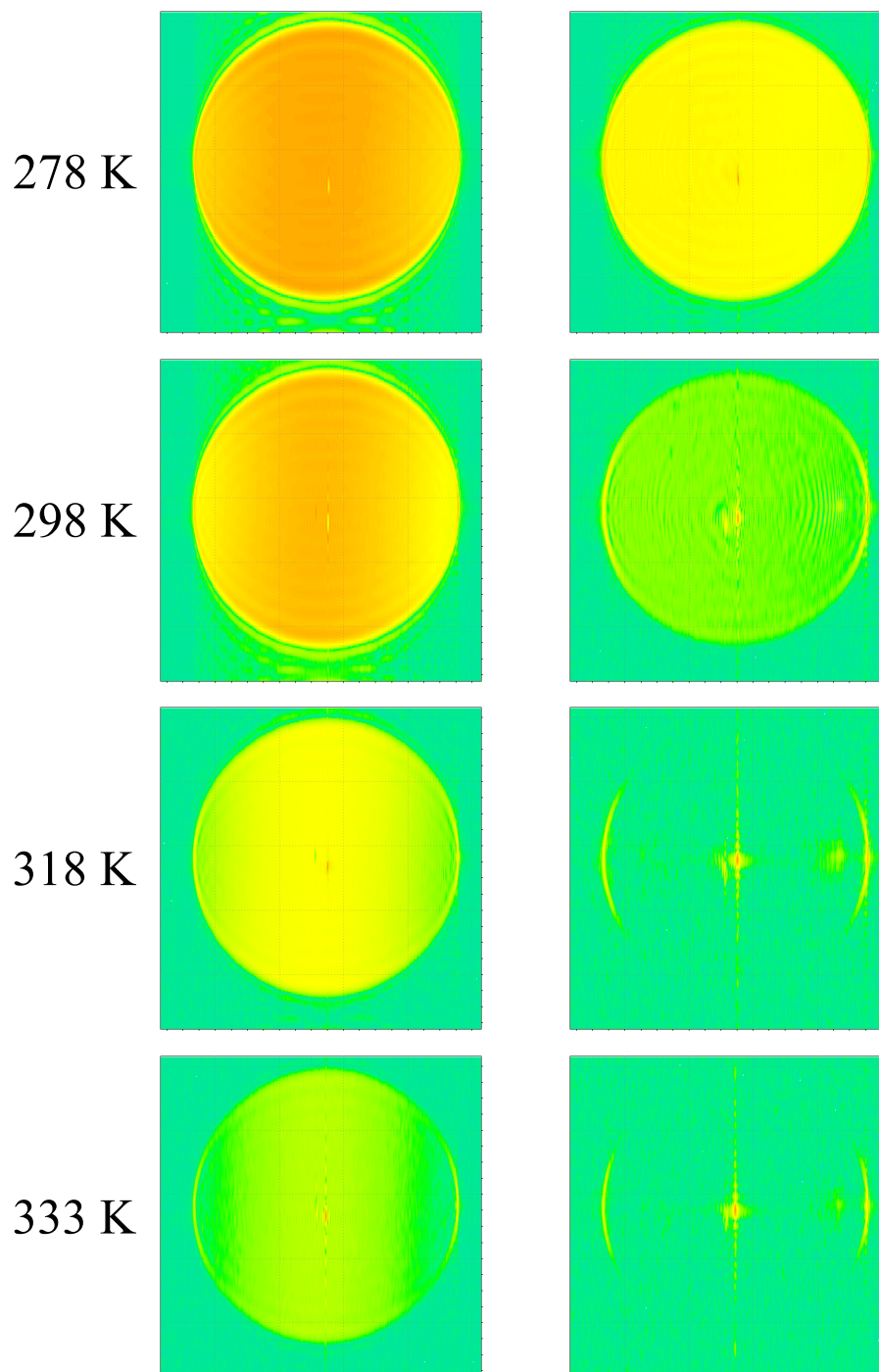


Figure 2.10: Different images obtained at four different temperatures, and hence with four different diffusion coefficients. The left column obtained using the pulse program of Fig. 2.9a, and the right column recorded using the pulse program of Fig. 2.9b. The phantom was a 5mm NMR tube filled with de-ionized water. In both cases the duration of the chirp pulses was $\tau=30$ ms, the readout bandwidth was 25 kHz, and the $TE = 65$ ms.

Specific absorption rate (SAR) considerations for *in vivo* applications

As for any other MRI method, the specific absorption rate (SAR) is an important concern for *in vivo* applications. For almost all spatially encoded methods that use rather long frequency-swept *rf*-pulses, SAR can potentially be problematic. By using long repetition times RT , it is possible to alleviate this problem. Also a variant of the DC-RASER sequence (with two additional 90° pulses) has already been applied *in vivo* [47]. In order to reduce SAR one may also apply small gradients (and hence use chirp pulses with small bandwidth) and then exploit super-resolution methods [2, 46] to reconstruct the image. These methods enable one to use weaker chirp pulses (thus attenuating the SAR) while keeping sufficient resolution. However, the stronger the field inhomogeneities, the larger the encoding gradients (and hence the larger the *rf* amplitudes) that need to be applied in order to obtain undistorted images.

Signal-to-noise ratio comparison between RASER and DC-RASER

There are a lot factors that affect the signal-to-noise ratio (SNR) resulting from a sequence. However, in our case the most important factors are T_2 and the strength of the spatial encoding gradient. The effect of T_2 is the same for both RASER and DC-RASER, because TE is the same for both. Obviously the shorter the relaxation time T_2 , the larger the signal loss due to relaxation, and consequently this method is not a promising method to study objects with very short T_2 . In contrast to T_2 losses, the diffusional signal losses due to G_{se} are not the same for these two sequence. As implied by equations 2.17 and 2.18, the average signal loss due to diffusion is less for RASER than for DC-RASER. As a result, the average SNR is larger for RASER; however, to interpret the resulting images one must be careful. As discussed in the “Results and discussion” section, when diffusion can be neglected, the signal-to-noise ratio (SNR) is identical for both RASER and DC-RASER, while in the presence of diffusion DC-RASER has the same SNR as

RASER at the edges of the image. If the SAR permits it, DC-RASER is preferable since the diffusion losses are uniform; the apparent gains in SNR in RASER at centre of the image only cause a misleading contrast.

2.2.5 Concluding remarks

In conclusion, although the basic RASER experiment is quite robust with respect to inhomogeneous static fields, signal losses due to diffusion may give rise to a misleading contrast. This is because the de- and re-phasing intervals are not the same for all coordinates r across the sample. As a consequence, even if the local diffusion coefficient $D(r)$ is the same for all voxels $\Delta V(r)$, the attenuation of the signal $S(r)$ due to diffusion is not independent from the coordinates r of the voxel $\Delta V(r)$, which gives rise to a non-genuine contrast. In the DC-RASER experiment however, these losses are uniform over the entire object, so that the contrast can be ascribed to genuine factors such as variations of spin density, relaxation rates, and diffusion coefficients.

Chapter 3

Contrast enhancement by echo shifting in spatially encoded single-scan MRI

3.1 Types of contrast available in traditional Fourier MRI

In a magnetic resonance image, the signal intensity of each pixel provides some information about the spin density of the corresponding voxel. However, the signal intensity is always weighted due some phenomena like longitudinal and transverse relaxations, and diffusion. Therefore, if two voxels have different relaxation or diffusion properties (different T_1 , T_2 , T_2^* , D , etc.) they can be distinguished even they have the same spin density. This, can be accomplished by favouring one of the weighting mechanisms over the others. For example for a gradient echo sequence (that starts with an excitation not an inversion) with a repetition time of TR , and an echo time of TE , the signal intensity S of a voxel with a spin density of ρ_0 , longitudinal relaxation time T_1 , and transverse relaxation time

T_2 can be written as:

$$S = \rho_0 \left(1 - \exp\left(\frac{-TR}{T_1}\right) \right) \exp\left(\frac{-TE}{T_2^*}\right) \quad (3.1)$$

In this case, choosing a $TR \gg T_1$ nullifies the effects of the factor $(1 - \exp(\frac{-TR}{T_1}))$, and choosing a $TE \ll T_2^*$ cancels out the effects of the factor $\exp(\frac{-TE}{T_2^*})$. Therefore, by choosing an appropriate value for TR and TE one can favour one weighting mechanism over the other. However, one must note that a magnetic resonance signal is always weighted by a mixture of all weighting mechanisms. The images in which one of the weighting mechanisms is favoured are usually referred to as T_1 -weighted, T_2 -weighted, diffusion-weighted, etc. Fig. 3.1 shows the importance of choosing an appropriate TR or TE to be able to differentiate between two voxels with different T_1 or T_2 . In Fig. 3.1a the signal intensity of a typical T_1 -weighted sequence (the term $(1 - \exp(\frac{-TR}{T_1}))$) is shown. The blue curve shows the signal for a voxel with long T_1 , and the red curve represents the signal of a voxel whose T_1 is short. It is assumed that both voxels have the same spin density. As can be seen, for very short or very long repetition times (corresponding to TR_1 and TR_3 respectively) the difference between the signals of the two voxels is low, rendering an image with a low contrast. However, for an appropriate value of TR the two signals are significantly different, leading to an image with a fair contrast. The same story applies for T_2 -weighting, and the echo time TE has to be adjusted carefully, as can be seen in Fig. 3.1b. It turns out that for two voxels with the same spin density, and with a slightly different T_1 , the optimum value for repetition time in a T_1 -weighted sequence is $TR_{opt} = T_{1,shorter}$, where $T_{1,shorter}$ is the shorter T_1 between the two voxels. Similarly for a T_2 -weighted sequence the optimum value for the echo time is $TE_{opt} = T_{2,shorter}$, where $T_{2,shorter}$ is the shorter T_2 between the two voxels (chapter 15 of ref. [5]).

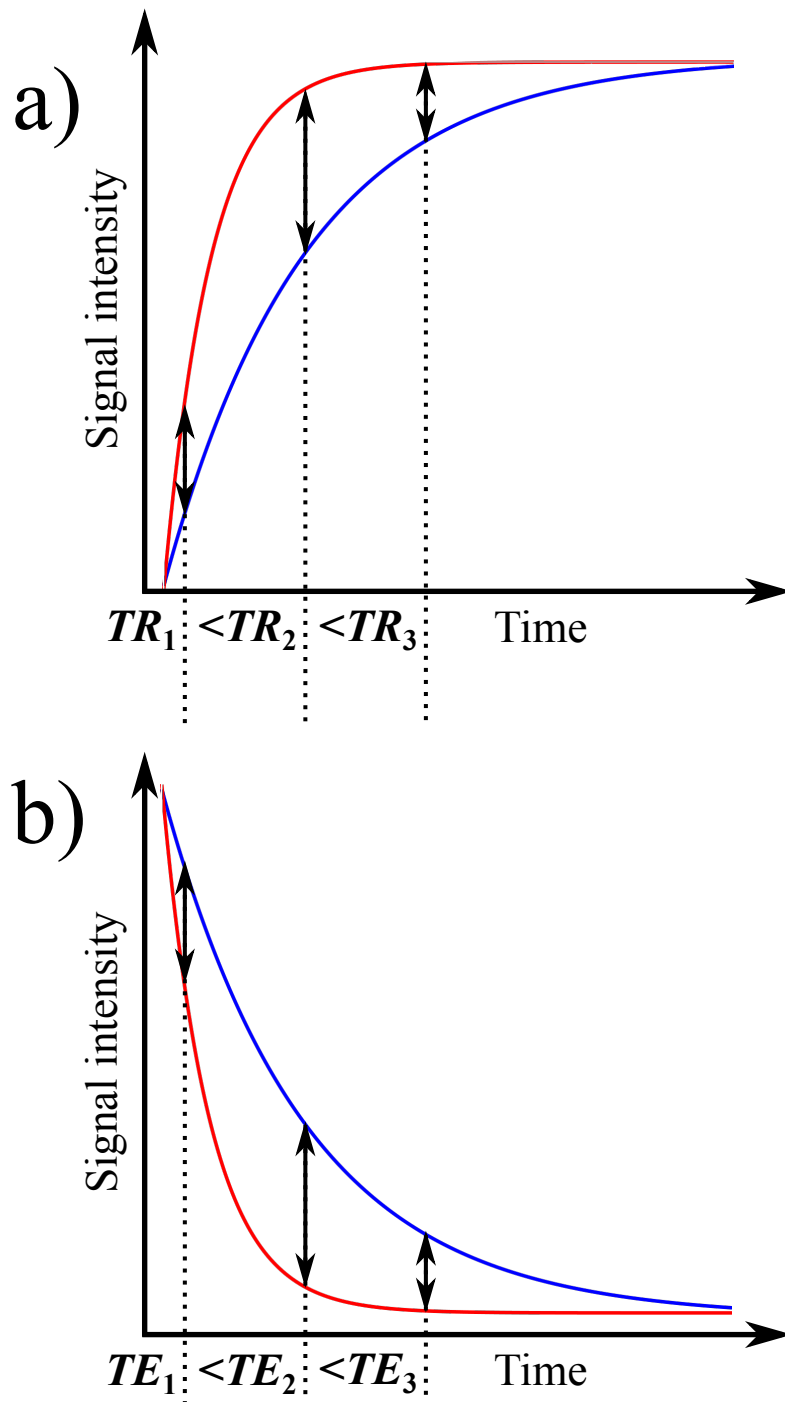


Figure 3.1: (a) Signal intensity in a typical T_1 -weighted sequence for a voxel with a short T_1 , the red curve, and for voxel with long T_1 , the blue curve. Note that to have a fair contrast TR must be appropriately adjusted. (b) Signal intensity in a typical T_2 -weighted sequence for a voxel with a short T_2 , the red curve, and for voxel with long T_2 , the blue curve. Like (a) to be able to observe a reasonable contrast, a proper TE must be used.

3.2 Types of contrast available in spatially encoded MRI

As discussed in the previous chapter, to overcome the effects of static field inhomogeneities, single-scan hybrid imaging methods that use spatial encoding in one direction and k -space encoding in the other have been shown to be superior to traditional imaging techniques based on full k -space encoding. Like all other MRI techniques, these methods can in principle be implemented in different ways that favour different sources (and hence different types) of contrast. There are plenty of published works about various aspects of spatial encoding, in particular about the theory and principles [48, 52, 12, 53, 54, 79], the resilience to inhomogeneous magnetic fields [59, 47, 58, 55], the spatial resolution [46, 2], and various applications [13, 3, 56, 80, 81, 82, 83, 84, 85]. However, hybrid techniques have not completely matured yet, and there are only few published works concerning contrast. By modifying an already established hybrid imaging sequence called Rapid Acquisition by Sequential Excitation and Refocusing (RASER) [3] so as to obtain Echo Shifted RASER (ES-RASER) sequences, we show in this chapter that by shifting spin echoes one can tune the contrast due to inhomogeneous T_2^{inh} decay.

In this chapter, we show how a variant of the RASER sequence dubbed ES-RASER can lead to tunable T_2^{inh} -weighted images. One must distinguish between T_2^* , T_2 , and T_2^{inh} which are related by the equation $\frac{1}{T_2^*} = \frac{1}{T_2} + \frac{1}{T_2^{inh}}$. In sequences that contain an echo delay TE the brightness of individual voxels $\Delta V(r)$ is normally reduced by local attenuation factors $\exp(\frac{-TE}{T_2^*(r)})$ and $\exp(\frac{-TE}{T_2(r)})$ for T_2^* - and T_2 -weighting respectively (gradient echo and spin echo sequences respectively).

¹In some references T_2^{inh} is represented by T_2' . To avoid any misunderstanding in this dissertation T_2^{inh} is defined by $\frac{1}{T_2^*} = \frac{1}{T_2} + \frac{1}{T_2^{inh}}$.

3.3 Theory

3.3.1 Contrast enhancement

The principles of the RASER sequence [3] have been explained in some detail in the previous chapter and will not be repeated here. We focus on our modification that leads to a T_2^{inh} -weighted image where the contrast can be tuned to the desired level by modifying the relative durations and amplitudes of two encoding gradients that can be characterized by a “mismatch parameter” ξ . The idea is reminiscent of so-called “echo shifting” in k -encoded MRI techniques. As explained above, the attenuation factor depends on the echo time TE (in the case of T_2 - or T_2^* -weighting). Since TE is normally shorter than the repetition time TR , there is a loss of contrast for very short TR s. In 1992, Moonen and co-workers introduced the idea of echo shifting to enhance the T_2^* contrast under such conditions, that is, whenever the repetition time (TR) is short [6]. By shifting the echoes, Moonen and his colleagues could achieve $TE > TR$, which enhances the T_2^* contrast. This technique has been applied to a variety of k -encoded imaging methods [86, 87]. Although echo shifted multi-scan k -encoding methods are different from our single-scan spatial encoding ES-RASER method, their main logic is similar. In ES-RASER, the spin echoes are shifted to enhance the contrast level. The pulse sequence used for ES-RASER is shown in Fig. 3.2.

By comparing the RASER sequence in Fig. 2.3 with ES-RASER, we see that in RASER, the duration τ_2 of the second spatial encoding gradient G_2 , is the same as τ_1 while in ES-RASER they are not equal. In order to start decoding from the edge of the field of view in ES-RASER the areas of G_1 and G_2 must be the same, while in order to shift the spin echoes, τ_2 must differ from τ_1 . To explain the idea of echo shifting, the ES-RASER sequence can be represented by a simple double-echo sequence, as shown in Fig. 3.3.

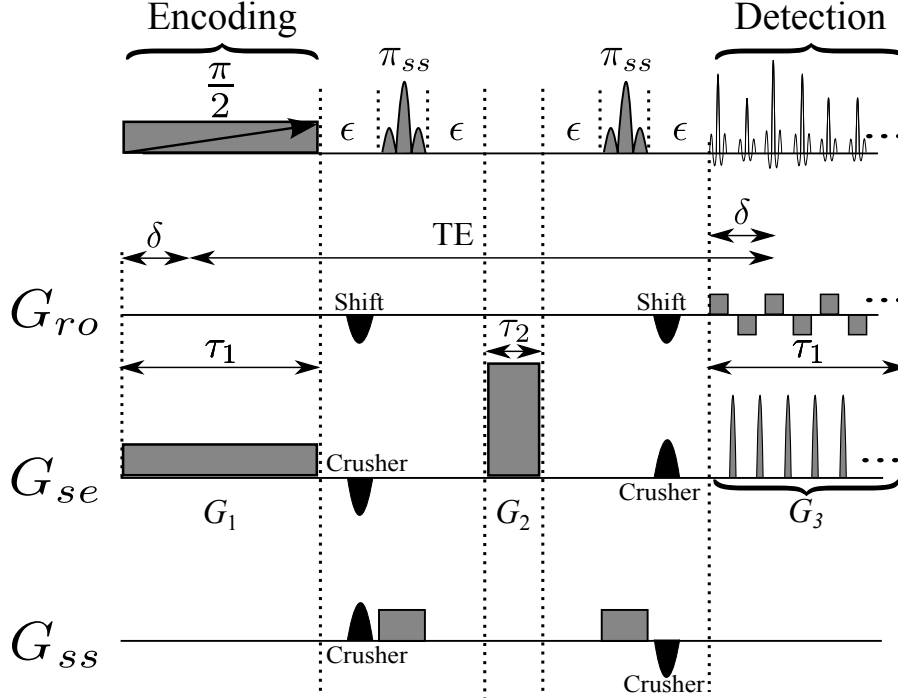


Figure 3.2: The Echo Shifted Rapid Acquisition by Sequential Excitation and Refocusing (ES-RASER) sequence. The chirp $\frac{\pi}{2}$ encoding pulse uses a linear frequency sweep. An arbitrary spin-packet is excited at $t = \delta$. G_{ro} , G_{se} , and G_{ss} represent the readout, spatial encoding, and slice-selection gradients respectively. The labels “ π_{ss} ” stand for slice-selective shaped pulses with I-BURP2 profiles [88]. The “Shift” gradients of duration ϵ shift the echoes to the centre of k -space; their total area must correspond to half the area of one of the alternating readout gradients. The simultaneous “Crusher” gradients of duration ϵ remove artefacts. In all ES-RASER experiments shown in Fig. 3.6, the chirp pulses have Wurst amplitude profiles [78] and cover a range of 45 kHz in $\tau_1 = 21.8$ ms, the matrix sizes were 64×64 , the FOV 27.0×27.0 mm, $G_{se} = 0.035$ T m $^{-1}$, $G_{ro} = 0.22$ T m $^{-1}$, $G_{ss} = 0.07$ T m $^{-1}$ and the slice thickness was ca. 1 mm. The areas of the spatial encoding gradient G_1 and of the gradient G_2 must be equal, and both must be equal to the integral G_3 of all blip gradients in the detection period. The mismatch parameter is defined as $\xi = 1 - \frac{\tau_2}{\tau_1}$. For the special case where $\tau_2 = \tau_1$ i.e., ($\xi = 0$), ES-RASER becomes identical with the basic RASER method.

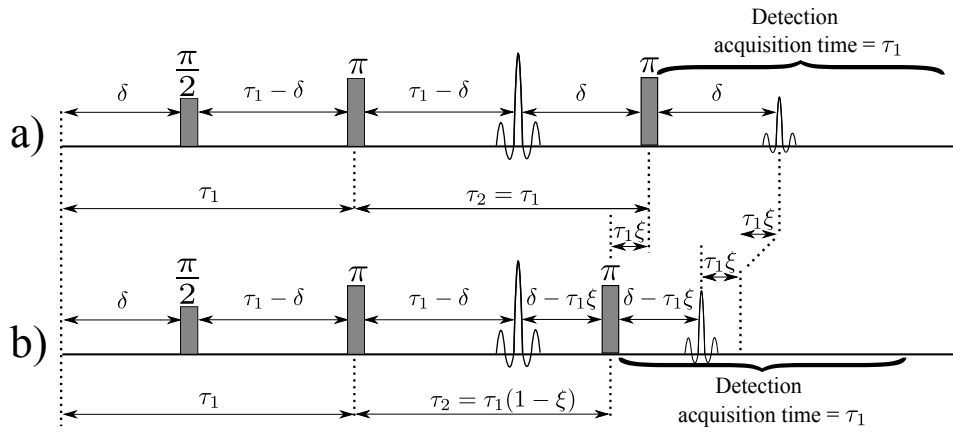


Figure 3.3: (a) Normal double echo sequence with two “matched” refocusing pulses. A chirp excitation pulse of duration τ_1 acts like a hard $\frac{\pi}{2}$ pulse that hits a typical spin-packet at $t = \delta$. The magnetization then de-focuses during the interval $\tau_1 - \delta$. The first spin echo occurs at time $t = 2\tau_1 - \delta$. If the interval between the two π pulses is $\tau_2 = \tau_1$, the second spin echo occurs at $t = 2\tau_1 + \delta$, where the signal of the corresponding spin-packet is detected. The pulse durations can be neglected compared to the delays. If diffusion can be neglected, the second echo is attenuated by a factor of $\exp(\frac{-2\tau_1}{T_2})$ regardless of T_2^{inh} , since the inhomogeneous decay is fully refocused. (b) “Mismatched” double echo sequence where the time interval between the two refocusing pulses is reduced by $\tau_1 \xi$, and the entire signal acquisition is shifted back by $-\tau_1 \xi$. The first spin echo still occurs at time $t = 2\tau_1 - \delta$, but the second spin echo now appears at $t = 2\tau_1(1 - \xi) + \delta$. The signal amplitude of the spin-packet, which is detected at $t = 2\tau_1 - \tau_1 \xi + \delta$, is therefore attenuated by a factor $\exp(\frac{-(\tau_1 + \tau_2)}{T_2}) \exp(\frac{-\tau_1 |\xi|}{T_2^{inh}})$. Note that in (b) not only the second π pulse, but the entire acquisition sequence is shifted backward by $\tau_1 \xi$. For further clarification refer to the text and Fig. 3.2.

As can be understood from Fig. 3.3a, if $\tau_1 = \tau_2$ (i.e., in the original RASER sequence), the sequence will result in a normal train of spin echoes, and hence in a purely T_2 -weighted image attenuated by $\exp(\frac{-TE}{T_2(r)})$ that is hardly affected by $T_2^{inh}(r)$, since the field inhomogeneities are refocused. However, any mismatch in the timing of the sequence, i.e., of the gradient durations (for $\tau_1 \neq \tau_2$) will cause a mismatch by an interval of $\tau_1 - \tau_2$ between the peak of the spin echo and the point in time where the signal of a given voxel is decoded. As shown in Fig. 3.3b, in this case the attenuation factor is $\exp(\frac{-TE}{T_2(r)} - \frac{|\tau_1 - \tau_2|}{T_2^{inh}(r)})$. Therefore, a mismatch in timing (for $\tau_1 \neq \tau_2$) permits us to incorporate T_2^{inh} -weighting into the RASER sequence. Note that, while changing the duration τ_2 of the second encoding gradient, its area must be kept constant.

If we define a dimensionless mismatch parameter as $\xi = \frac{(\tau_1 - \tau_2)}{\tau_1} = 1 - \frac{\tau_2}{\tau_1}$, the attenuation factor can be written as $\exp(\frac{-TE}{T_2(r)} - \frac{|\xi|\tau_1}{T_2^{inh}(r)})$. Therefore, depending on the values of the parameters TE , ξ , T_2 , and T_2^{inh} , different factors will have a dominant effect on contrast. In the original RASER method [3], the durations of the two gradients are the same ($\tau_2 = \tau_1$), which means that $\xi = 0$. In this limit the effects of T_2^{inh} on the contrast are minimized, while for $\tau_2 \neq \tau_1$ the contrast is affected by variations in inhomogeneous T_2^{inh} . Thus the pulse programme of Fig. 3.2 can be tuned to adjust the relative contributions of T_2 and T_2^{inh} to the contrast. Using the pulse sequence of Fig. 3.2, one can start with a mismatch parameter $\xi = 0$ and gradually vary ξ until an appropriate contrast has been achieved.

Immunity of the sequence to globally inhomogeneous magnetic fields

As explained in the first chapter, in spatially encoded MRI the signals stem from those parts of the sample for which the spatial variation of the phase is zero. Therefore, in order to know which part of the object is being decoded at each time during signal acquisition we need to express the phase of the magnetization as a function of spatial

coordinates. The phase profile produced by a frequency-swept chirp pulses, and more specifically the phase profile resulting from the RASER sequence have been described elsewhere [52, 2, 54, 3, 4]. Without loss of generality, we can assume that the spatial encoding gradient G_{se} is applied along the y direction. Hence, when $\tau_1 = \tau_2$ (i.e., in RASER), neglecting all inhomogeneities, the phase of the magnetization after the second 180° pulse can be expressed as a function of the normalised y -coordinate (Eq. 2.13d):

$$\phi_{RASER}^{homo} = -\frac{R}{8} - \frac{R}{2}Y - \frac{R}{2}Y^2 \quad (3.2)$$

where Y is the dimensionless normalized y -coordinate defined as $Y = \frac{y}{L}$ in which $L = \frac{b_w}{\gamma G_{se}}$ is the total length (in meters) covered by the chirp pulse, and R is the localizing factor given by $R = b_w \tau$ where b_w and τ are the bandwidth and the duration of the chirp pulse respectively. In the previous chapter, we saw that in an inhomogeneous magnetic field Eq. 3.2 must be rewritten as (Eq. 2.15):

$$\phi_{RASER}^{inhomo} = -\frac{R}{8} - \frac{R}{2}Y' - \frac{R}{2}Y'^2 \quad (3.3)$$

where $Y' = Y + Y_{inh}$, $Y_{inh} = \frac{\omega_{inh}}{\gamma G_{se} L}$ is the apparent displacement, and ω_{inh} is the frequency offset (in $\frac{rad}{s}$ units) due to the field inhomogeneities.

Now, imagine that instead of τ_1 the duration of the second spatial encoding gradient is τ_2 . In this case the spin echo occurs $(\tau_1 - \tau_2)$ seconds before the detection moment (or $(\tau_1 - \tau_2)$ seconds after the detection moment if $\xi < 0$), as can be seen in Fig. 3.3. Consequently, during this time a phase factor of $\omega_{inh} \times (\tau_1 - \tau_2)$ is built up due to field inhomogeneities. Therefore, just before the signal acquisition the phase will be:

$$\begin{aligned} \phi_{ES-RASER}^{inhomo} &= \phi_{RASER}^{inhomo} + \omega_{inh} \times (\tau_1 - \tau_2) \\ &= \phi_{RASER}^{inhomo} + R\left(1 - \frac{\tau_2}{\tau_1}\right)Y_{inh} = \phi_{RASER}^{inhomo} + R\xi Y_{inh} \end{aligned} \quad (3.4)$$

Therefore, compared to RASER in which $\xi = 0$, here we have an extra phase factor $R\xi Y_{inh}$. To comprehend the role of this extra term, we should note that the signal is given by the integral:

$$Signal = \int \rho(x, y) \exp(i \text{phase}(x, y)) dx dy \quad (3.5)$$

consequently any phase factor other than a constant phase that does not depend on the spatial coordinates will result in an attenuation of the signal intensity, and hence a contrast in the image. This is because, a position-dependent phase factor will alternately result in positive and negative integrands, which diminish the integral (signal).

The key point here is that although the extra term $R\xi Y_{inh}$ can bring about some local contrasts, it will not distort the image. As mentioned in the first chapter, the signals in spatially encoded MRI come almost exclusively from the flat regions of the phase profiles. Therefore, in order to obtain those parts of the object being decoded at each time, we demand very small spatial variations in the phase profile where its derivative vanishes, i.e., $\frac{d\phi}{dY} = 0$. For a spin-packet decoded at the time t , a phase factor of $\gamma G_{se} y t = R Y \frac{t}{\tau}$ has to be added, which is caused by the detection gradient. Therefore in a homogeneous magnetic field for the case of RASER we have:

$$\frac{d}{dY} (\phi_{RASER}^{homo} + \gamma G_{se} y t) = \frac{d}{dY} \left(-\frac{R}{8} - \frac{R}{2}Y - \frac{R}{2}Y^2 + RY\frac{t}{\tau} \right) = 0 \quad (3.6)$$

$$\Rightarrow Y_{RASER}^{homo} = -\frac{1}{2} + \frac{t}{\tau} \quad (3.7)$$

In inhomogeneous fields, all terms Y , must be replaced by $Y + Y'$; therefore, in an inhomogeneous magnetic field for RASER we have:

$$\frac{d}{dY} \left(-\frac{R}{8} - \frac{R}{2}Y' - \frac{R}{2}Y'^2 + RY' \frac{t}{\tau} \right) = 0 \quad (3.8)$$

$$\Rightarrow Y_{RASER}^{inhomo} = -\frac{1}{2} + \frac{t}{\tau} - Y_{inh}(Y) \quad (3.9)$$

Which is exactly what we expect. In RASER, an inhomogeneous magnetic field cause an image distortion, which equal to $Y_{inh}(Y)$. Note that $Y_{inh}(Y)$ is a function of position. Therefore, the displacement of different voxles is not the same, which is called image distortion.

To see the effects of field inhomogeneities on image distortion in ES-RASER an extra term $R\xi Y_{inh}$ has to be added to Eq. 3.8. That is:

$$\frac{d}{dY} \left(-\frac{R}{8} - \frac{R}{2}Y' - \frac{R}{2}Y'^2 + RY' \frac{t}{\tau} + R\xi Y_{inh} \right) = 0 \quad (3.10)$$

$$\Rightarrow Y_{ES-RASER}^{inhomo} = -\frac{1}{2} + \frac{t}{\tau} - Y_{inh} + \frac{\frac{dY_{inh}}{dY}}{1 + \frac{dY_{inh}}{dY}} \xi \quad (3.11)$$

Therefore, compared to RASER here, there is an extra pixel displacement given by $\frac{\frac{dY_{inh}}{dY}}{1 + \frac{dY_{inh}}{dY}} \xi$. This extra displacement is small if $|\frac{dY_{inh}}{dY}| \ll 1$. We have:

$$\frac{dY_{inh}}{dY} = \frac{1}{G_{se}} \frac{dB_z^{inh}}{dy} \quad (3.12)$$

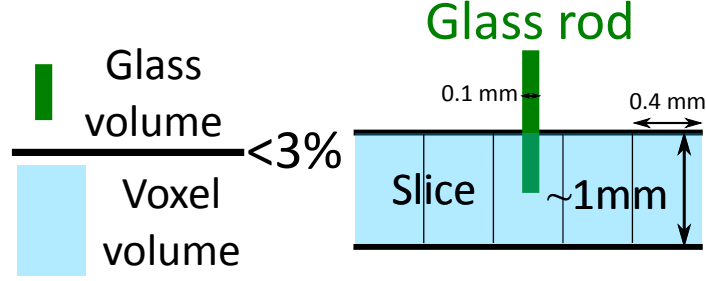


Figure 3.4: Schematic view of the imaged slice. The diameter of the glass fibre is smaller than the dimensions of the voxels. As a result, the spin density does not significantly change in the vicinity of the glass fibre. However, as shown in Fig. 3.5, the magnetic field will be perturbed in the vicinity of the tip of the glass fibre. Therefore, the observed contrast can be attributed to local susceptibility effects caused by the glass fibre.

Where B_z^{inh} is defined as: $B_z^{inh} = \frac{\omega_{inh}}{\gamma}$. Therefore, unless the field inhomogeneities are comparable with or greater than the spatial encoding gradient, image distortions in ES-RASER are small (in the order of image distortions in basic RASER). In the case that field inhomogeneities are comparable with or larger than the spatial encoding gradient, both RASER and ES-RASER lead to distorted images.

3.4 Experimental

The experiments were performed on a Bruker 800 MHz NMR instrument equipped with an imaging probe with an internal diameter of 2.5 cm. The phantom comprised of two parts, a cross-shaped piece of plastic immersed in water, which was used in the experiments described in the previous chapter (Fig. 2.6); and a thin glass fibre made by stretching a piece of molten glass heated in a flame. The glass fibre was suspended so that its tip was positioned within the thickness of the selected slice. The imaged slice and the position of the glass fibre are shown schematically in Fig. 3.4.

Although the glass fibre does not significantly change the spin density in the vicinity of its tip, the magnetic field is locally inhomogeneous near the tip of the glass fibre because

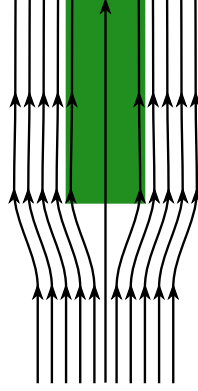


Figure 3.5: Locally perturbed magnetic field lines (black arrows) in the vicinity of the glass fibre (green rectangle). Since the magnetic susceptibilities of glass and water differ, there is a field gradient close to their interface.

of differences in the magnetic susceptibility of glass and water, as schematically depicted in Fig. 3.5. The discontinuity of the susceptibility leads to a dark spot in the resulting images. The phantom was placed in a 25 mm OD glass tube filled with de-ionized water. Echo planar imaging (EPI) [8] images were obtained using the Paravision programme. The pulse programmes appropriate for all other images were implemented in Topspin, and the signals were processed by a home-written Python code. In all cases, the matrix size was 64×64 , the field of view (FOV) was 27.0×27.0 mm, and the slice thickness was about 1 mm. The two slice-selective shaped pulses had I-BURP2 [88] shapes. The phase errors due to the first pulse are compensated by the second one, so that one need not use shaped pulses that are specifically designed for refocusing, which require more *rf* power.

3.5 Results and discussion

3.5.1 Enhanced contrast

As previously mentioned in this dissertation, one of the merits of hybrid methods compared to traditional k -space encoding is that even in very inhomogeneous magnetic

fields the images are not severely distorted. To illustrate this point, all images shown in Fig. 3.6 were recorded in an inhomogeneous magnetic field.

The homogeneity of the magnet was deliberately degraded by mis-setting the current in the xy shim coil of our 18.81 T (800 MHz) wide-bore magnet. Traditional k -space encoded EPI images were obtained either with a spin echo sequence (i.e., with a 180° refocusing pulse), or with a gradient echo sequence (i.e., without any refocusing pulses). The former brings about a T_2 -weighted image while in the latter case the image is T_2^* -weighted. These images are shown in Fig. 3.6a and b respectively. It is obvious that both are severely distorted. The spin echo sequence gives a much stronger signal with less contrast, but it does not prevent image distortions. This is because the distortions are mostly determined by the ratio of the strengths of the applied gradients to the internal gradients. In contrast to the traditional k -encoded EPI images of Fig. 3.6a and b, the RASER image shown in Fig. 3.6c ($\xi = 0$), and the ES-RASER images shown in Fig. 3.6d ($\xi = 0.1$), Fig. 3.6e ($\xi = 0.2$), and Fig. 3.6f ($\xi = 0.7$) do not suffer from significant distortions due to the inhomogeneous magnetic field, because the encoding gradient is much larger than the internal gradients. As expected, the sequence with $\xi = 0$ (i.e., the original RASER sequence that leads to a purely T_2 -weighted image) refocuses the de-phasing caused by the discontinuity of the magnetic susceptibility at the interface between water and glass. Since the spin density hardly changes between two adjacent voxels (including the voxels near the glass fibre, which have a diameter that is much smaller than the voxel size) the contrast will not be sufficient to differentiate between two adjacent voxels, as is evident from Fig. 3.6c. However, there is a marked contrast in Fig. 3.6d–f where the brightness of the voxels is determined by their T_2^{inh} ; which is drastically affected in the vicinity of the glass fibre. Note that neither the spin density nor the homogeneous T_2 varies between these voxels. The mismatch parameter ξ of ES-RASER can be tuned to obtain the desired contrast, as shown in Fig. 3.6d–f for $\xi = 0.1, 0.2$ and 0.7 . For practical strengths of encoding gradients (allowed for our machine), values of ξ

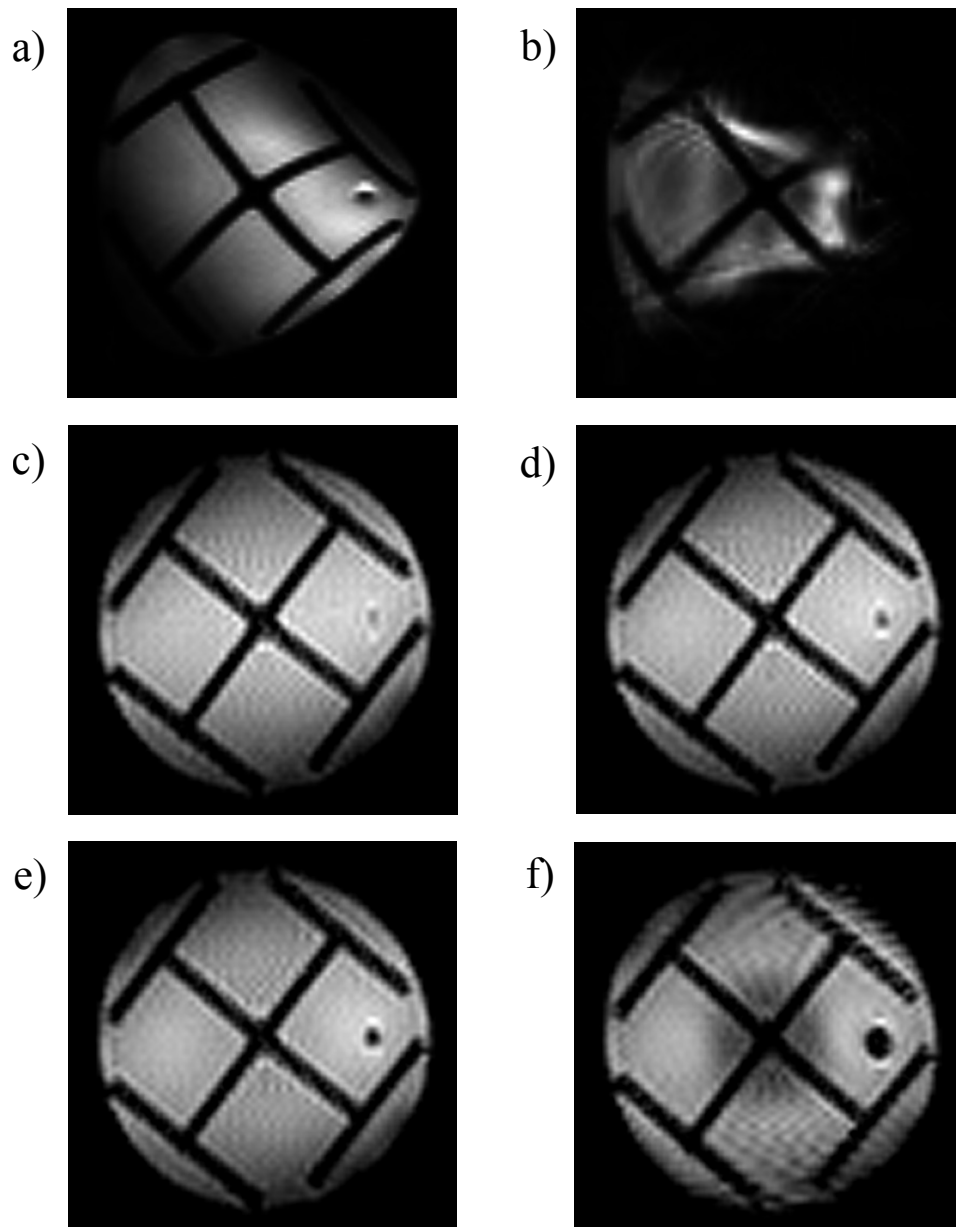


Figure 3.6: (a) Conventional spin echo EPI, and (b) gradient echo EPI, both with a matrix size 64×64 , FOV 27.0×27.0 mm, readout bandwidth 250 kHz, but with $TE = 45.8$ ms for (a) and $TE = 25.6$ ms for (b). (c), (d), (e), and (f) Echo Shifted (ES)-RASER, with matrix sizes 64×64 , FOV 27.0×27.0 mm, readout bandwidth of 250 kHz. (c) $TE = 46.0$ ms and $\xi = 0$ (i.e., like in the original RASER experiment). Images (d) to (f) where obtained with decreasing TE and increasing ξ : (d) $TE = 43.8$ ms and $\xi = 0.1$; (e) $TE = 41.6$ ms and $\xi = 0.2$; (f) $TE = 30.7$ ms and $\xi = 0.7$. Note that in ES-RASER, the larger the parameter ξ the shorter the echo time TE , and the larger the contrast. This property of ES-RASER stands in opposition to traditional k -encoding methods, where the contrast increases for longer TE intervals.

up to 0.95 can be achieved. Increasing the mismatch parameter ξ leads to an increase of the attenuation factor, and hence to an enhanced T_2^{inh} contrast. The contrast may be adjusted empirically to the desired level by repeating the sequence with increasing mismatch parameters ξ until a satisfactory contrast has been achieved. Typical effects may be appreciated in Fig. 3.6c-f.

By choosing a positive value for the mismatch parameter, one introduces an asymmetry in the timing of the sequence, so that the spin echo occurs before the detection moment, as can be seen in Fig. 3.3b. However, in order to introduce an asymmetry in the timing of the RASER sequence, one may also prolong the delay between the two π pulses instead of shortening it. This leads to a negative mismatch parameter, hence $\xi = 1 - \frac{\tau_2}{\tau_1}$. In this case the spin echo occurs after the detection moment. The attenuation factor is still given by $\exp(\frac{-(\tau_1+\tau_2)}{T_2}) \exp(\frac{-\tau_1|\xi|}{T_2^{inh}})$, but of course τ_2 is longer than for a positive mismatch parameter, leading to a larger signal loss due to T_2 relaxation.

Looking at the images in Fig. 3.6c-f it is obvious that the larger the parameter ξ , the larger the contrast. However, a larger ξ implies a shorter echo time TE . Note that this property of the ES-RASER stands in contrast to most MRI methods where the contrast increases for large echo times TE . This is because in ES-RASER it is mainly the asymmetry in the timing that determines the contrast, rather than the duration of TE .

3.5.2 Informative maps

Beside contrast enhancement, ES-RASER sequence can be used to obtain various informative maps. Indeed, the attenuation factor can be rewritten as $\exp(\frac{-TE}{T_2(r)} - \frac{|\xi|\tau_1}{T_2^{inh}(r)}) = \exp(\frac{-2\tau_1}{T_2(r)} + \xi\tau_1[\frac{1}{T_2(r)} - \frac{(|\xi|/\xi)}{T_2^{inh}(r)}])$, for both negative and positive mismatch parameters. There-

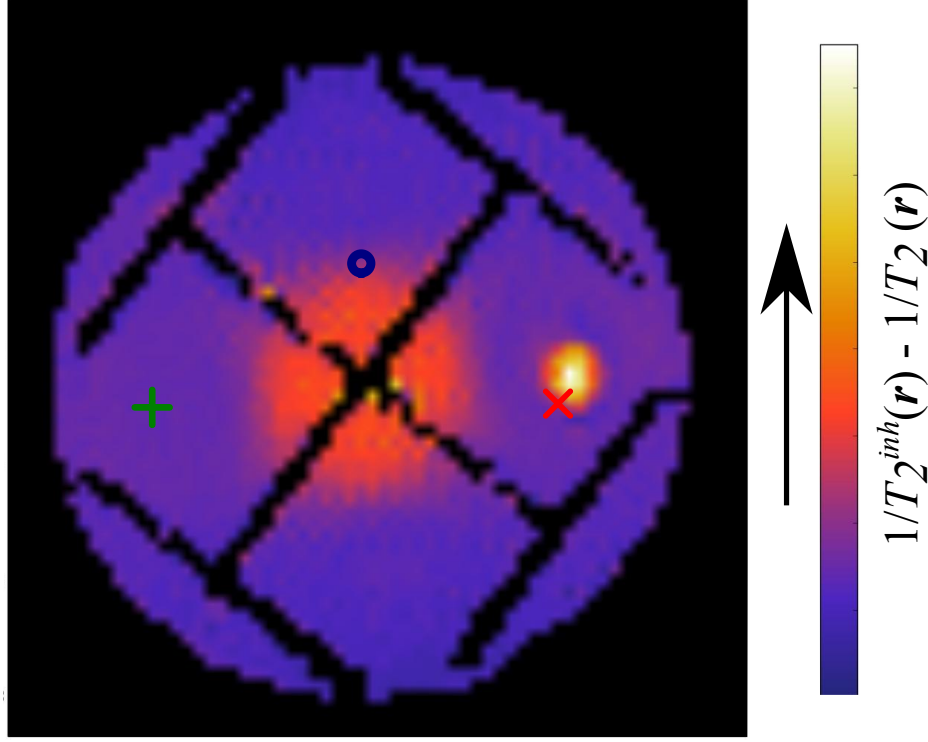


Figure 3.7: Colour map of the difference $(\frac{1}{T_2^{inh}(r)} - \frac{1}{T_2(r)})$ derived from a series of 11 ES-RASER images obtained in a homogeneous magnetic field. Areas with small susceptibility effects appear in violet. The area in the centre which appears in red has moderate susceptibility effects. The homogeneity of the field in the area close to the tip of the glass fibre is severely distorted. The meaning of symbols “o”, “x”, and “+” are explained in the caption to Fig. 3.8.

fore, one can extract the parameters $(\frac{1}{T_2^{inh}(r)} - \frac{1}{T_2(r)})$ for $\xi < 0$ ² or $(\frac{1}{T_2(r)} + \frac{1}{T_2^{inh}(r)}) = \frac{1}{T_2^*(r)}$ for $\xi > 0$ by fitting the signal intensity as a function of ξ for each pixel. Fig. 3.7 shows a typical map obtained by fitting the signal intensity pixel-by-pixel from a set of 11 images where $\xi \geq 0$ was varied in the range $0 \leq \xi < 0.925$. This map can be considered as a representation of $\frac{1}{T_2^{inh}}$, provided the variations in $T_2(r)$ are small compared to the variations in $T_2^{inh}(r)$. For $\xi > 0$ one can obtain a map of the difference $(\frac{1}{T_2^{inh}(r)} - \frac{1}{T_2(r)})$ while for $\xi < 0$ one can obtain a map of the sum $(\frac{1}{T_2^{inh}(r)} + \frac{1}{T_2(r)}) = \frac{1}{T_2^*(r)}$.

Fig. 3.8 shows the signal intensity as function of the parameter ξ for three different voxels. The red curve that decays faster than the others, corresponds to a voxel with

²The sign function $|\xi|/\xi = 1$ for $\xi > 0$, and $|\xi|/\xi = -1$ for $\xi < 0$ respectively.

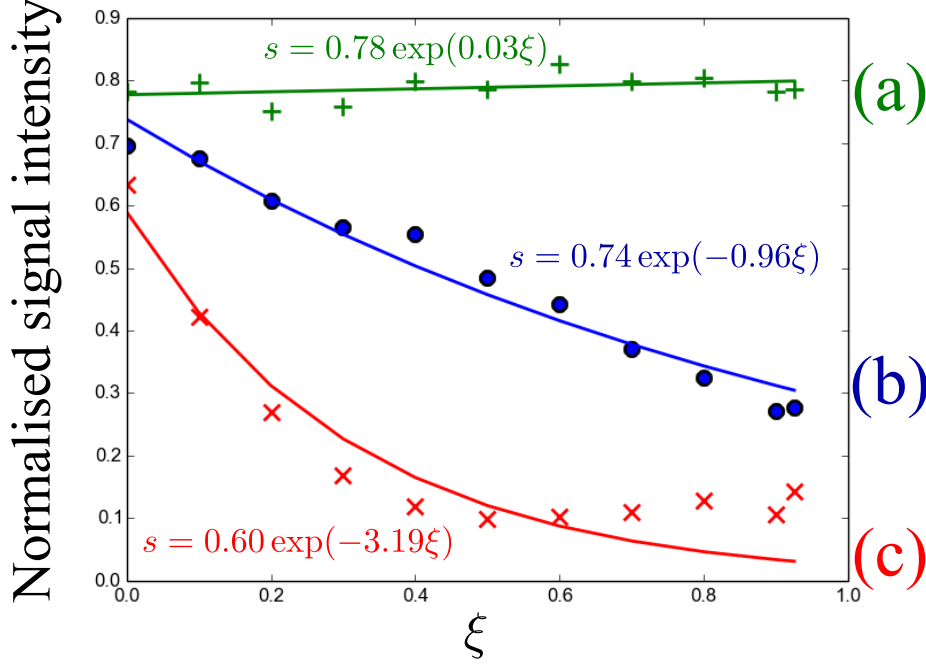


Figure 3.8: Signal intensity as a function of the parameter ξ . (a) A voxel with small susceptibility effects indicated by a “+” symbol in Fig. 3.7. (b) A voxel near the central area of the phantom with moderate susceptibility effects indicated by a “o” symbol in Fig. 3.7. (c) A voxel in the vicinity of the glass fibre with severe susceptibility effects indicated by a “x” symbol in Fig. 3.7. Discrete points represent experimental data, and solid lines represent fit curves. Optimised fit parameters are given in the equations. Obviously in (c) by increasing the mismatch parameter ξ , the signal decays more rapidly than in (a) or (b), i.e., $\frac{1}{T_2^{inh}}$ is larger for the voxels in the vicinity of the glass fibre.

large susceptibility effects in the vicinity of the glass fibre (“x” symbol in Fig. 3.7); whereas the blue curve corresponds to a voxel with moderate susceptibility effects near the central area (“o” symbol in Fig. 3.7). The green curve shows a slightly increasing signal, which is an indication of small susceptibility effects (“+” symbol in Fig. 3.7). These curves, are in agreement with what is shown in Fig. 3.7.

For the sake of comparison a B_0 map of the cross-shaped phantom without glass fibre is shown in Fig. 3.9. This map was obtained by a standard B_0 mapping sequence available in Paravision. As can be seen, the area in the centre has moderate susceptibility effects, which is again in agreement with Fig. 3.7.

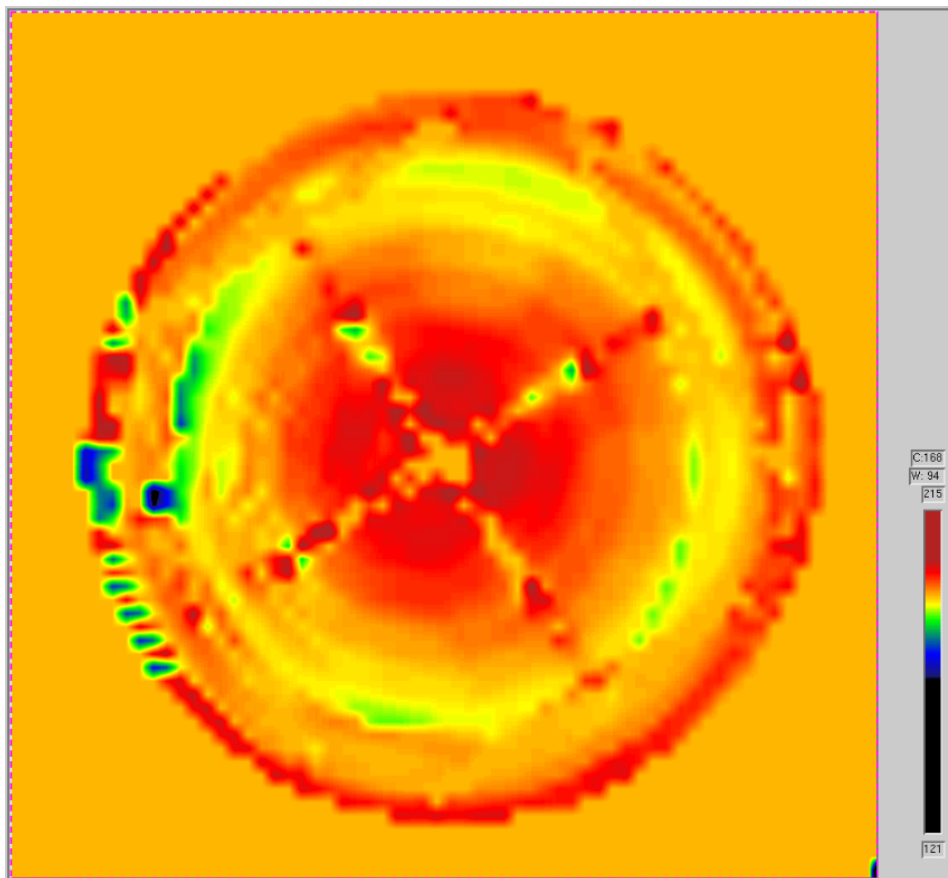


Figure 3.9: B_0 map obtained by standard B_0 mapping sequence available in Paravision. The phantom was the cross-shaped piece of plastic without the glass fibre, and the magnetic field was homogeneous. Similar to Fig. 3.7 the central area shows a field inhomogeneity, although the magnet was properly shimmed. This most probably is due to susceptibility effects of the plastic object.

3.5.3 Concluding remarks

There are currently two methods that are frequently used for functional magnetic resonance imaging (fMRI): Echo Planar Imaging (EPI) [8], and Principles of Echo Shifting with a Train of Observables (PRESTO) [86]. Each of them has its own pros and cons. Compared to EPI, PRESTO is less prone to image distortions due to inhomogeneous fields. Like ES-RASER, PRESTO also allows for tunable weighting (T_2^* -weighting in this case) that can be optimized empirically. However, compared to single-scan methods like EPI, PRESTO suffers from a limited temporal resolution, thus limiting the ability of observing the blood oxygen level dependent (BOLD) contrast [87]. The RASER sequence has been used successfully both for morphological brain imaging [3] and for fMRI [56, 80]. We believe that ES-RASER may offer a better alternative for both EPI and PRESTO, since it can provide the advantages of EPI, while avoiding its disadvantages. ES-RASER is a single-scan technique, so that its temporal resolution can be as high as in EPI, while being much less sensitive to image distortions caused by inhomogeneous magnetic fields. It is worth mentioning that we have adapted our ES-RASER pulse sequence to the Paravision programme, which is more user-friendly than Topspin for imaging applications, and more popular in the MRI community. So in addition to the *in vitro* applications shown in this chapter, ES-RASER is ready for *in vivo* investigations. This is one of the perspectives of this chapter.

Chapter 4

Alternative sequences for single-scan time-encoding MRI

4.1 Gradient switching rate in available single-scan techniques

Forty years after its invention, echo planar imaging (EPI) is still one of the most popular single-scan MRI techniques, [8, 9, 89] and is widely used in functional imaging [14]. One drawback of this method is the need for closely-spaced positive and negative gradients, which requires very fast switching of the gradients, setting high demands on the hardware. Typical gradient rise and fall times of about 100 μ s are required for this method [10]. More importantly, even if rapid switching between positive and negative gradients is technically feasible, the switching rate¹ of the gradients needs to be limited for *in vivo* applications in order not to stimulate the patient’s nervous system [11].

¹In the MRI literature, especially those concerning MRI hardware, “gradient switching rate” is also known as “gradient slew rate”.

Some single-scan methods use alternating gradients. Some of them, such as EPI and hybrid spatial encoding, use alternating gradient during data acquisition, and in some cases like in hybrid time-encoding [12, 13], alternating gradients are used for excitation. In hybrid spatial encoding methods, either a constant decoding gradient or a series of blips can be used in the spatial encoding direction; k -encoding along the other dimension is obtained by a series of rapidly alternating gradients, similar to the detection block of the EPI sequence.

Another class of single-scan imaging techniques comprises hybrid time-encoding methods [12, 13], in which the sample is excited using a series of spin-packet-selective² pulses. These pulses excite narrow strips of spins called spin-packets. The excited spin-packets are then detected using a constant readout gradient which produces a train of echoes, each of which arises from a single spin-packet. Similar to the other hybrid techniques, it is sufficient to perform a 1D Fourier transformation (1DFT) on each echo to convert the raw signal to an image.

Among the established single-scan imaging methods, BURST techniques [90, 91] have the lowest gradient switching rate, because they only use constant gradients. Employing a very small flip angle, and a constant readout gradient, BURST techniques produce a series of echoes that are equally spaced in k -space. These echoes are phase-encoded in the conventional manner. At the end, an image is produced by a two dimensional Fourier transformation (2DFT) of the signal. Despite having this advantage, BURST suffers from a very low sensitivity, and has not found widespread applications in clinical MRI [92]. Spiral imaging techniques avoid rapid switching, and use gradients that vary smoothly, however they have their own pros and cons [93], and will not be discussed here.

²In order to distinguish these pulses from the traditional slice-selective pulses, they are named spin-packet-selective pulses. In the MRI literature they are also called “line” or “spin-isochromat”.

In the rest of this chapter, we limit ourselves to time-encoding sequences, and show how one can modify established time-encoding sequences to reduce the gradient switching rate. Our modified version has the additional advantage that it leads to a uniform echo time TE for all echoes. In addition, we show how one can increase the resolution, and reduce image artefacts by implementing the sequence in an interleaved fashion, albeit at the cost of losing the advantages offered by a single-scan sequence.

Fig. 4.1a shows a typical EPI sequence, while a typical hybrid spatial encoding sequence is shown in Fig. 4.1b. Their detection blocks are similar, though the blip gradients are usually larger in hybrid spatial encoding than in EPI. In both sequences, the blip gradients can be replaced by a constant gradient whose area equals the total area of the blips, which is shown in Fig. 4.2. In the sequences shown in Fig. 4.2, a simple Fourier transformation leads a distorted image in both EPI and spatial encoding, therefore, additional processing is needed for image reconstruction [94, 3]. Replacing the phase- or spatial encoding blip gradients by a constant gradient obviously reduces the gradient switching rate, both in EPI and some other sequences using EPI-like detection schemes. However, replacing the alternating readout gradients is not easy in these sequences.

A typical BURST sequence [90, 91] is depicted in Fig. 4.3a³. The original⁴ time-encoding sequence proposed by Meyerand and Wong [12] is shown in Fig. 4.3b. The detection blocks for these two sequences are similar. In both techniques we have a train of echoes in the detection block. In BURST these echoes are phase-encoded, whereas in hybrid time-encoding techniques they are time encoded; that is each echo corresponds to a time at which the corresponding spin-packet has been excited.

³There are some other versions for BURST in which the phase-encoding is performed in detection block.

⁴In this dissertation the pulse sequence introduced in the reference number [12] is referred to as the original time-encoding sequence. However before this version, in 1993, Meyerand and her colleagues had published a different time-encoding sequence in which a quadratic xy field gradient was used in time-encoding direction [49].

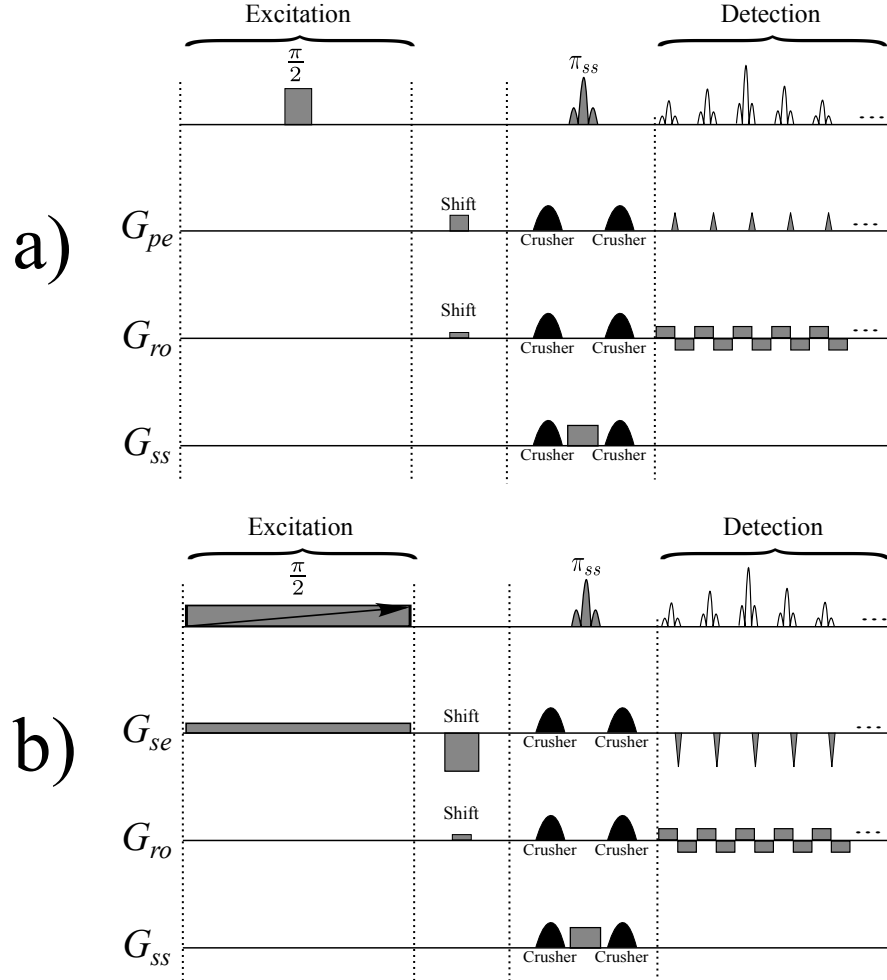


Figure 4.1: (a) A typical spin echo EPI sequence, and (b) a typical hybrid spatial encoding sequence. G_{ss} , G_{ro} , G_{pe} , and G_{se} stand for slice-selection, readout, phase-encoding, and spatial encoding gradients respectively. The sloping arrow represents a frequency-swept chirp pulse. Note that the detection blocks are similar, although in the hybrid sequence, the blip gradients (applied in the spatial encoding direction) are usually larger than in EPI. The large shift gradient (in spatial encoding direction) reverses the detection order, leading to an identical TE for all echoes.

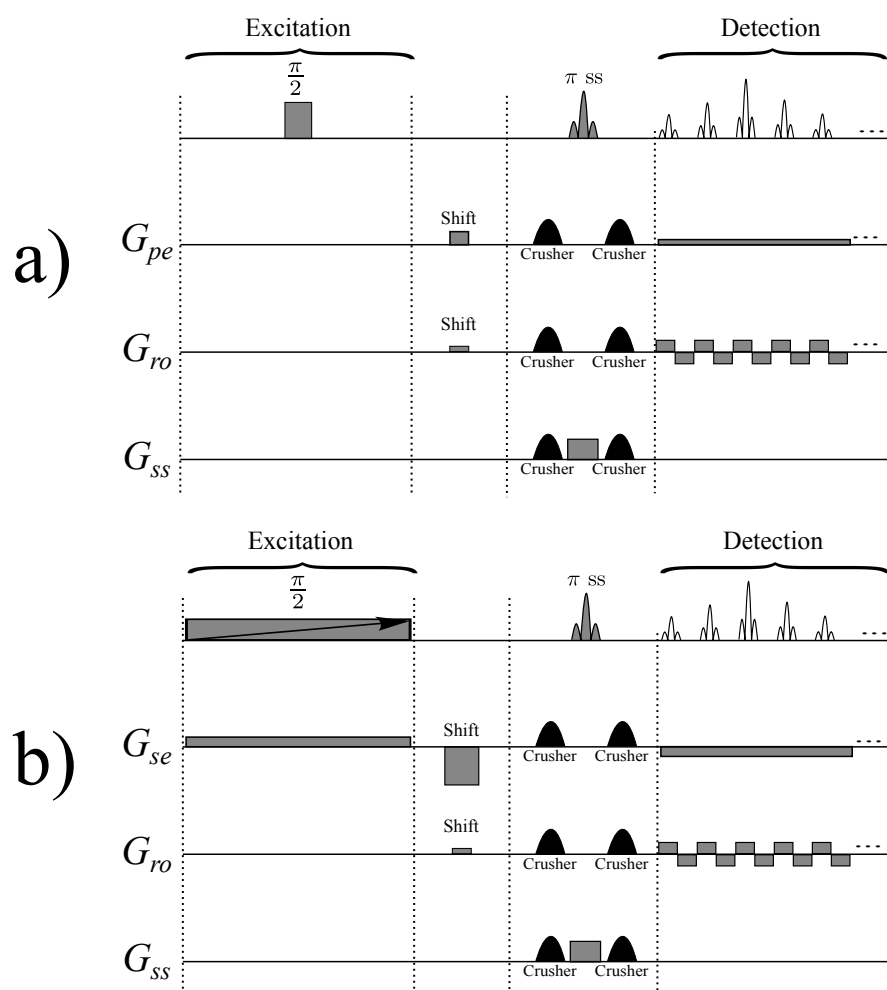


Figure 4.2: (a) A typical spin echo EPI sequence using a constant phase-encoding gradient during data acquisition, and (b) a typical hybrid spatial encoding sequence with a constant spatial encoding gradient during data acquisition. G_{ss} , G_{ro} , G_{pe} , and G_{se} stand for slice-selection, readout, phase-encoding, and spatial encoding gradients respectively. The sloping arrow represents a frequency-swept chirp pulse. The detection blocks are similar, although in the hybrid sequence the gradients (in the spatial encoding direction), are usually larger than in EPI. The large shift gradient (in spatial encoding direction) reverses the detection order, leading to an identical TE for all echoes. Note that both methods need some extra processing for image reconstruction, otherwise they lead to a distorted image.

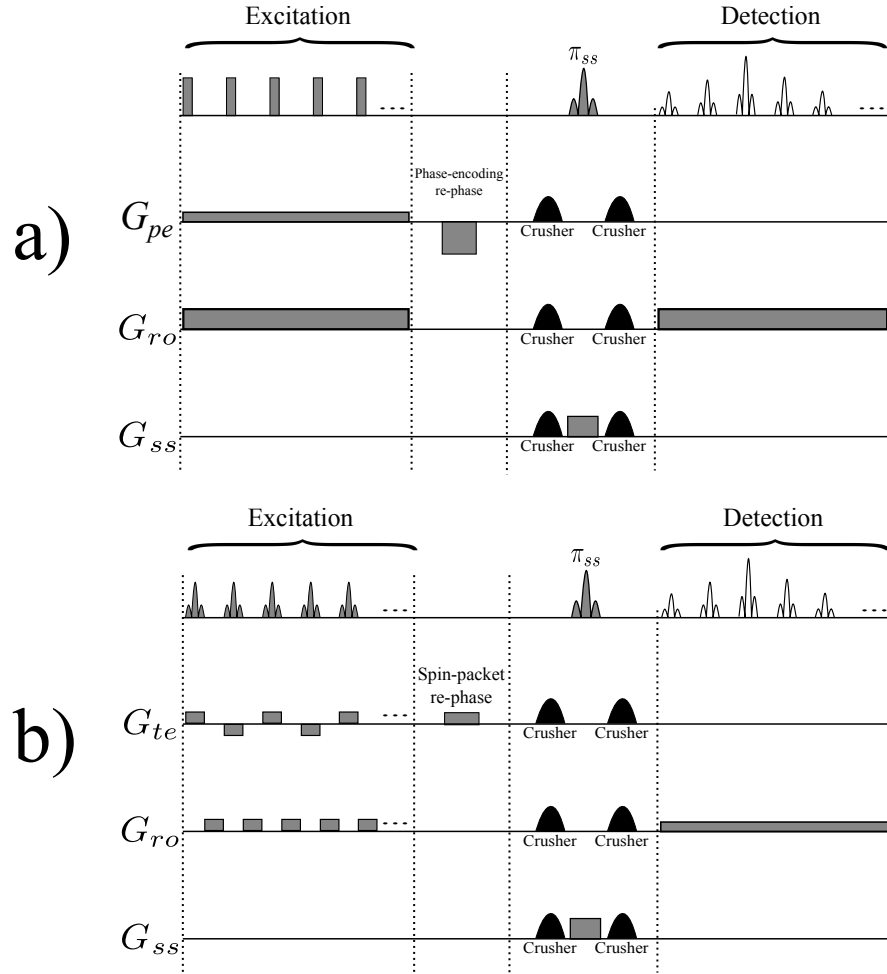


Figure 4.3: (a) A typical BURST sequence, and (b) the original hybrid time-encoding sequence proposed by Meyerand and Wong [12]. As usual, G_{ss} , G_{ro} , G_{pe} , and G_{te} represent slice-selection, readout, phase-encoding, and time-encoding gradients. In both cases, the re-phasing gradients will have the effect of un-winding the phase accumulated during excitation. The detection blocks of these two sequences are similar. Note that in the original BURST sequence [90, 91] phase-encoding is done in the detection block of the sequence, whereas in the modified version of BURST [92] shown in (a), phase-encoding is achieved in the excitation block of the sequence.

As can be deduced from Fig. 4.3b, the order of excitation is the reverse of the order of detection in the original hybrid time-encoding sequence. Those spin-packets that are excited earlier are detected later in this pulse sequence. Therefore, each spin-packet has a different echo time⁵. This causes a monotonic decay of the signal due to T_2 relaxation and diffusion, which is a disadvantage of the original time-encoding sequence. In contrast to EPI-like sequences, reducing the gradient switching rate in hybrid time-encoding sequences is not difficult. In the following sections, first we introduce some modifications into the original hybrid time-encoding sequences, and then we propose some alternatives to reduce the gradient switching rate.

4.2 Modifications on the original hybrid time-encoding sequence

4.2.1 Uniform echo time

Fig. 4.4a shows a variant of the original hybrid time-encoding sequence used in this work. It is very similar to the original hybrid time-encoding sequence proposed by Meyerand and Wong with this subtle difference that no rf -pulse is applied during negative time-encoding gradients. Fig. 4.4b depicts the modified version of the sequence shown in Fig. 4.4a. In Fig. 4.4b the echo time is the same for all data points. The idea is to reverse the order of the echoes with respect to the original sequence, which can be done by inserting a shift gradient. The area under this shift gradient must be equal to the total area of the readout blip gradients in the excitation block, plus half of the area of a single blip gradient pulse. Adding such a shift gradient will totally re-phase the first spin-packet, whereas the re-phasing of the second spin-packet will be slightly overdone, i.e., it is slightly de-phased. The third will be even more over re-phased (more de-phased), and

⁵That is why that Meyerand and Wong have always used average TE instead of TE .

so on. As a result, in contrast to the original sequence, spin-packets which are excited earlier will also be detected earlier, and those who are excited later will be detected later. Therefore, as a result of this modification, all data points will be acquired with the same echo time TE ; provided that, the acquisition and excitation times are the same, which is the case in our experiments. Adding half the area of a blip gradient to the shift gradient causes the echo of each spin-packet to occur in the middle of its detection period, thus increasing the signal-to-noise ratio. Having a constant echo time for all spin-packets avoids the non-uniform signal weighting observed in the original version [12].

4.2.2 Reducing the gradient switching rate

A new hybrid time-encoding sequence is introduced in Fig. 4.5a. In contrast to Fig. 4.4, a spin-packet which is excited by n^{th} excitation pulse is de-phased (in time-encoding direction) by the $n + 1^{th}$ spin-packet-selective gradient and all subsequent gradients. All spin-packet-selective gradients in Fig. 4.5 are positive, while in Fig. 4.4 the effect of positive gradients is compensated by negative gradients. In other words in Fig. 4.5a the time-encoding blip gradients that are active during detection, they have the same function as the negative time-encoding blip gradients in Fig. 4.4 that are active during excitation, i.e, they re-phase the magnetization in time-encoding direction. In Fig. 4.5a, the time-encoding gradient is inactive during the data acquisition, therefore, the image reconstruction is done by performing only a 1DFT on each echo in the readout direction, without any need for a phase correction.

The blip gradients in the detection block of Fig. 4.5a can be replaced by a constant gradient whose area equals the total area of the blip gradients. As depicted in Fig. 4.5b. This sequence leads to the same results as Fig. 4.5a, and has the advantage that gradient switching rate is reduced. In analogy to the RASER experiments with constant spatial encoding gradients [3] mentioned before, the image reconstruction is a little different

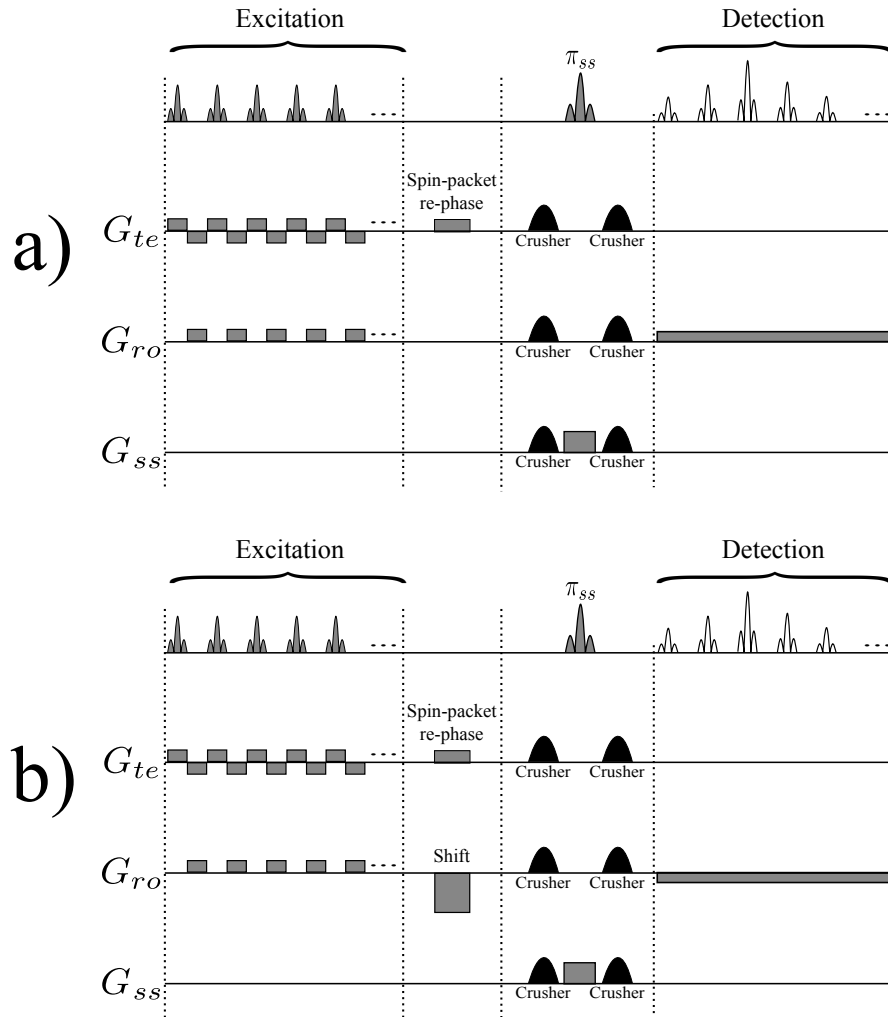


Figure 4.4: (a) The hybrid time-encoding sequence without reordering of the signal, and (b) with reordering of the signal, as used in some of our experiments. In contrast to (a), all echoes have an identical echo time TE in (b). This is achieved by adding a shift gradient, which causes the signal of the spin-packets to appear in the same order as the excitation. G_{ss} , G_{ro} , and G_{te} respectively stand for slice-selection, readout, and time-encoding gradients. The crusher gradients remove artefacts from the images, the shift gradient reverses the detection order, leading to an identical TE for all echoes. Spin-packet re-phasing will unwind the phases accumulated during the excitation of the spin-packets.

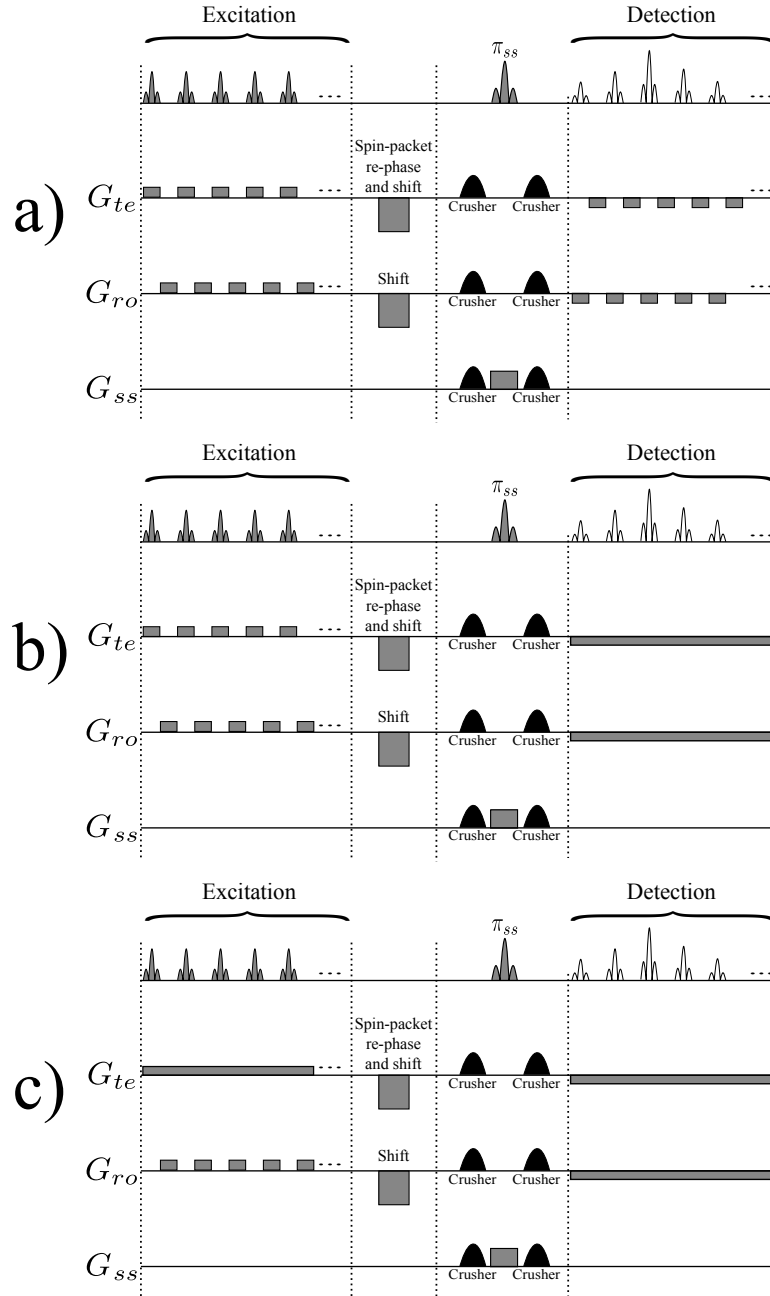


Figure 4.5: (a) Alternative hybrid time-encoding sequence in which excited the spin-packets are re-phased in the detection block. (b) Similar as (a), but where the pulsed gradients of the detection block are replaced by a constant gradient, so as to decrease the gradient switching rate. (c) A further decrease of the gradient switching rate can be achieved by replacing the spin-packet-selective blip gradients by a constant gradient. In all sequences, G_{ss} , G_{ro} , and G_{te} stand for slice-selection, readout, and time-encoding gradients, respectively. The crusher gradients remove artefacts from the images, the shift gradients reverse the detection order, leading to identical echo times TE for all echoes. Spin-packet re-phasing un-winds the phase accumulated during spin-packet excitation.

in this case; before performing the 1DFT on each echo, a time-dependent linear phase correction ϕ has to be applied to the data points according to the following equation [3].

$$\begin{aligned}\phi &= -2\pi n_{ro} \frac{\gamma G_{te} \text{FOV}_{te}}{\gamma G_{ro} \text{FOV}_{ro}} \left(\frac{n_{te}}{N_{te}} - \frac{x_{centre}}{\text{FOV}_{te}} - 0.5 \right) \\ &= -2\pi n_{ro} \frac{bw_{te}}{bw_{ro}} \left(\frac{n_{te}}{N_{te}} - \frac{x_{centre}}{\text{FOV}_{te}} - 0.5 \right)\end{aligned}\quad (4.1)$$

where G_{te} and G_{ro} are time-encoding and readout gradients, FOV_{te} and FOV_{ro} are the fields of view for time-encoding and readout directions, and bw_{te} and bw_{ro} are bandwidth for time-encoding⁶ and readout directions. n_{ro} is an index that refers to the n^{th} data point in the readout direction, n_{te} is an index that refers to n^{th} data row in the time-encoding direction, N_{te} is the total number of time-encoding rows (equal to the number of spin-packets), and x_{centre} is the position of the spin-packet excited when $n_{te} = 0.5N_{te}$. This phase correction is required because the time-encoding gradient is active during the data acquisition and leads to a phase shift of the frequency-encoded signal.

Further reduction of the gradient switching rate can be achieved by replacing the blip excitation gradients (in time-encoding direction) in Fig. 4.5b by a constant gradient. The resulting sequence is depicted in Fig. 4.5c. Replacing blip gradients in Fig. 4.5b by a constant gradient will increase the total area of the time-encoding gradient in excitation block, since, a constant gradient is active during whole excitation period. Consequently, the area of the time-encoding gradient in detection block must be adjusted accordingly.

4.2.3 Interleaved spin-packet-selection

Using long and large gradients will cause a significant signal attenuation due to diffusion. To avoid this effect, one can reduce the duration of de-phasing by reducing the number

⁶The time-encoding bandwidth is the difference between the highest and lowest frequency of the slice-selective pulses.

of pixels (in time-encoding direction) and by shortening the entire sequence. This will of course deteriorate the resolution. Alternatively, one can reduce the length of the gradients by dividing the experiment into several interleaved scans, where each scan uses a different set of frequencies to excite different spin-packets. This, reduces the length of each scan, diminishing signal attenuation due to diffusion. In practice, to implement an interleaved sequence, the frequencies of the spin-packet-selective pulses can be adjusted so that immediately adjacent spin-packets are not excited in individual scans, but excited in an interleaved fashion in complementary scans.

4.3 Experimental

All of our experiments were performed on a Bruker 800 MHz NMR instrument equipped with imaging accessories. Two different phantoms and two different coils (with different diameters) were used. The first phantom was a cross-shaped piece of plastic that was placed in a 25 mm O.D. glass tube filled with de-ionized water. This phantom is shown in Fig. 2.6. This phantom was used with a 25 mm imaging probe. The second phantom was a rawlplug (also known as “wall plug”. It is a piece of plastic used to enable the attachment of a screw in materials like concrete, wall, etc.) which is shown in Fig. 4.6. The second phantom was put in a 10 mm NMR tube filled with de-ionized water, and was used with a 10 mm imaging probe. The pulse programmes were written and implemented in Topspin, and the data were processed by a home-written Python code. For the cross-shaped phantom, the slice thickness was about 1 mm, the FOV was 27.0×27.0 mm, and the total matrix size was either 64×64 or 64×32 (64 in the k -encoding direction, and 32 in the time-encoding direction). For the rawlplug, the slice thickness was about 0.5 mm, the FOV was 27.0×13.5 mm (27.0 mm in the k -encoding direction, and 13.5 mm in the time-encoding direction), and the total matrix size was 64×32 (64 in k -encoding direction, and 32 in time-encoding direction). In experiments with four-fold interleaving

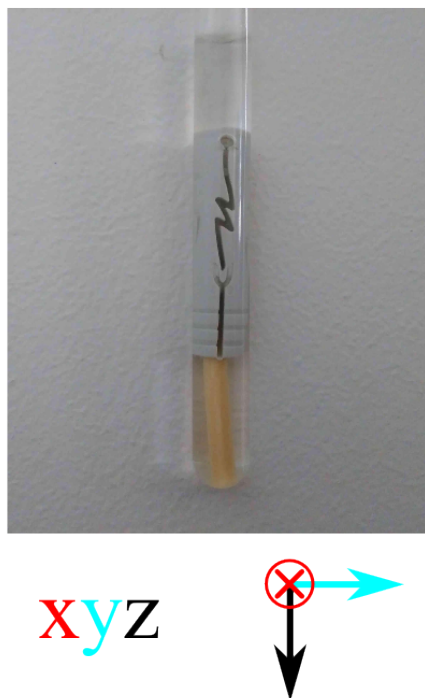


Figure 4.6: The rawlplug used as a phantom in this chapter. In all figures a “sagittal” image (parallel to y - z plane) of this phantom is depicted.

the total FOV was 27.0×27.0 mm, and the total matrix size was 64×64 , however, the matrix size for each of the four complementary scans was reduced to 16×64 .

4.4 Results and discussion

In Fig. 4.7 six images of the rawlplug are depicted, which were obtained by different imaging methods. Fig. 4.7a and b show standard FLASH and spin echo EPI images respectively. The parameters are given in the caption to Fig. 4.7. Since Fig. 4.7a was obtained by a multi-scan imaging sequence with a short echo time, it represents an almost ideal image. Some parts of Fig. 4.7b are slightly distorted; this is probably due to field inhomogeneities caused by susceptibility effects. Fig. 4.7c was obtained with an unmodified hybrid time-encoding sequence (shown in Fig. 4.4a), in which the order of

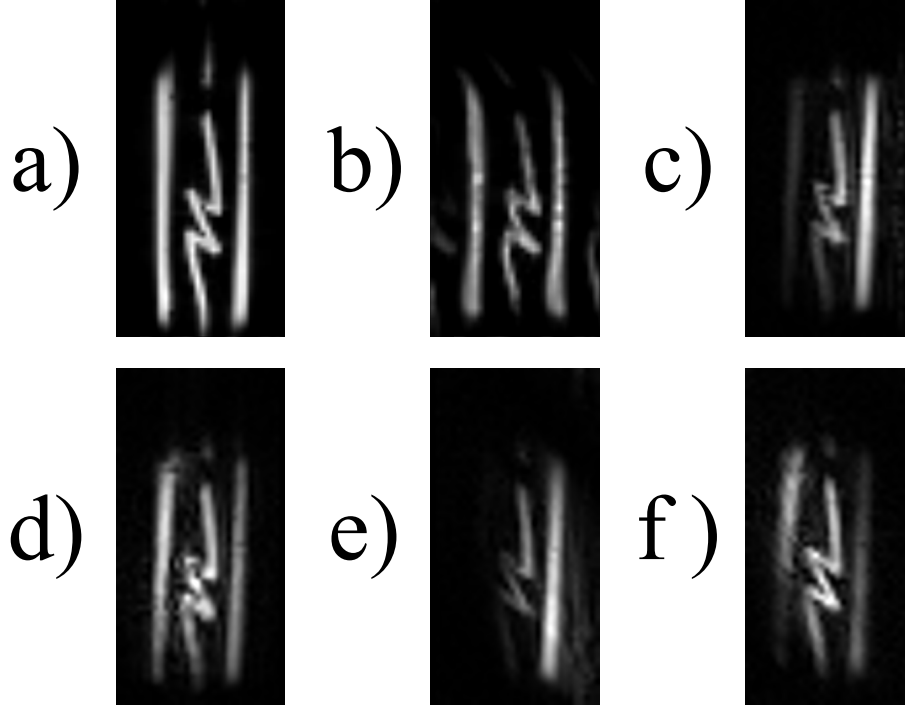


Figure 4.7: Sagittal view of the rawplug phantom. All images have been recorded with a matrix size of 64 in the k -encoding direction, and 32 in phase- or time-encoding direction ((a) and (b) phase-encoding, (c)–(f) time-encoding), an FOV 27.0 mm in the k -encoding direction, and 13.5 mm in phase- or time-encoding direction, and a slice-thickness 0.5 mm. (a) Multi-scan FLASH with a readout bandwidth of 50 kHz, excitation flip angle 30° , $TE=4.0$ ms, $TR=100$ ms, and a total scan time of 3.2 s. (b) Single-scan spin echo EPI with a readout bandwidth of 200 kHz, excitation flip angle 90° , $TE=21.8$ ms. (c) An image obtained by the unmodified hybrid time-encoding sequence shown in Fig. 4.4a, average $TE=21.6$ ms. (d) Image recorded with the hybrid time-encoding sequence of Fig. 4.4b, $TE=21.6$ ms for all echoes. (e) Image recorded with the hybrid time-encoding sequence of Fig. 4.5c (with a constant excitation gradient, but without the shift gradient), average $TE=21.6$ ms. (f) The same as (e) with reordering (with the shift gradient), $TE=21.6$ ms for all echoes. For all hybrid time-encoding sequences a readout bandwidth of 125 kHz, a total scan time 38.0 ms, and a rectangular spin-packet-selective pulses with a flip angle of 22.5° were used.

excitation and detection are reverse. As can be observed, the signals of some parts of the object have been lost as a result of relaxation and diffusion.

The situation has been improved in Fig. 4.7d obtained by the modified sequence shown in Fig. 4.4b, in which the shift gradient leads to identical echo times TE for all

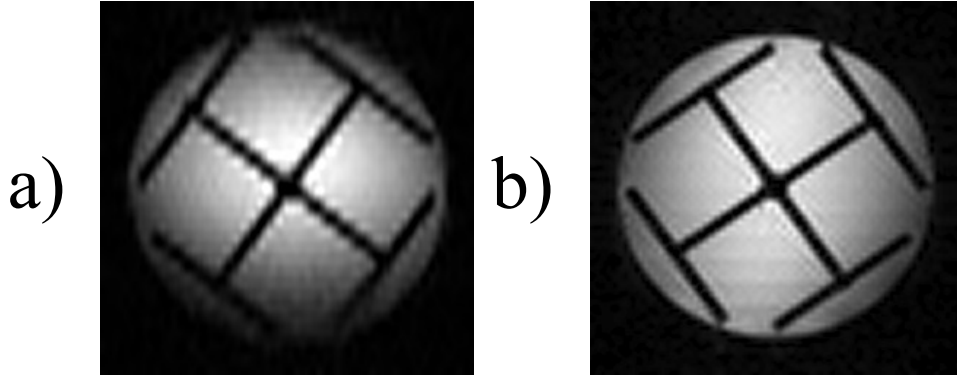


Figure 4.8: (a) Single-scan time-encoding image obtained using the sequence of Fig. 4.4b, with a matrix size of 32 in the time-encoding direction, and 64 in the k -encoding direction, a FOV of 27.0×27.0 mm, and $TE = 23.6$ ms. (b) Similar image as in (a) but obtained using a four-fold interleaving of the excitation frequencies, with a matrix size of 64×64 (16×64 for individual scans), a FOV 27.0×27.0 mm, and $TE = 12.4$ ms. In both, Gaussian pulses with a flip angle of 90° were used for the excitation of the spin-packets.

echoes. A comparison between Figs. 4.7c and d illustrates the benefits of re-ordering the signals by using an extra gradient.

Figs. 4.7e and f were obtained by the sequence shown in Fig. 4.5c, with and without reordering (shift) gradients, respectively. Note that in the non-reordered case the sign of the detection gradients must change. In Figs. 4.5b and c, both time-encoding and readout gradients are active during signal acquisition. Therefore, to obtain an undistorted image, we need a phase correction according to Eq. 4.1. Note that, although Figs. 4.7d and f do not show significant differences, Fig. 4.7f is to be preferred since it was obtained by a sequence with a smaller gradient switching rate.

4.4.1 Interleaving

Fig. 4.8a shows an image of the cross-shaped phantom obtained by the sequence of Fig. 4.4b. Fig. 4.8b was obtained under the same conditions as (a) but using a four-fold interleaving. As can be seen, artefacts near the top and bottom of Fig. 4.8a, which arise from signal attenuation due to diffusion, are absent in Fig. 4.8b. The resolution in the

time-encoding direction in Fig. 4.8b is twice as good as in Fig. 4.8a. Because of large signal losses due to diffusion, it is not possible to obtain a single-scan image under the conditions of Fig. 4.8b, i.e., with 64 pixels in the time-encoding direction. Comparing Figs. 4.8a and b shows the merits of implementing several time-encoding sequences in an interleaved manner, so that one can obtain images with high resolution, obviously at the expense of sacrificing the single-scan nature of the method.

4.4.2 The effects of excitation pulses with different shapes

Fig. 4.9 shows the effects of excitation pulses with different shapes for selective excitation of spin-packets in hybrid time-encoding methods. All images were obtained using the sequence shown in Fig. 4.4b using a simple Gaussian excitation pulse in Fig. 4.9a, a “Sinc” excitation pulse with two cycles in Fig. 4.9b and a “Sinc” excitation pulse with three cycles in Fig. 4.9c. In all case the same length of $256 \mu\text{s}$ was used for all three pulse shapes, leading to different bandwidths. In each experiments, the strength of the excitation gradient was adjusted accordingly to avoid overlapping between consecutive spin-packets. As can be seen, the differences between these three images is not a lot. However, the image of Fig. 4.9a is to be preferred because it was obtained using a much smaller bandwidth in the time-encoding direction, and much smaller time-encoding gradient.

4.4.3 Overlapping excitation pulses

In time-encoding methods, the thickness of the spin-packets is determined by the bandwidth of the excitation pulses and the strength of the time-encoding gradients used during excitation. In an ideal situation, the field of view in the time-encoding direction (FOV_{te}) can be divided into several non-overlapping spin-packets. This, would be the case if the time-encoding gradient is large enough so that the thickness of the spin-packet excited

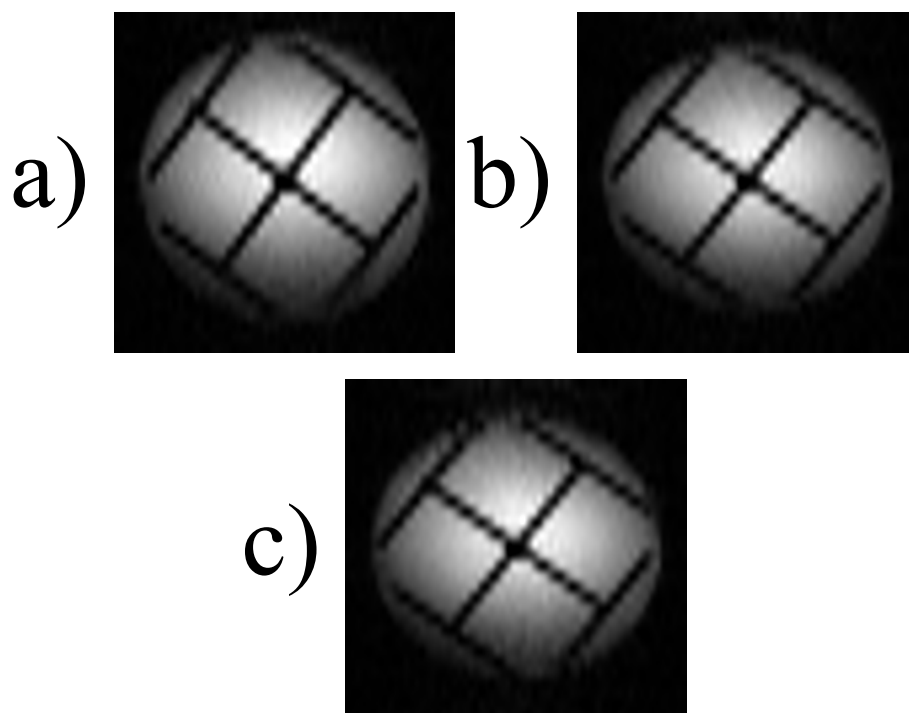


Figure 4.9: Three different images obtained using the sequence shown in Fig. 4.4b. (a) Using a simple Gaussian excitation pulse and a time-encoding bandwidth of $bw_{te} = 310\text{kHz}$, (b) using a “Sinc” excitation pulse with two cycles, and $bw_{te} = 496\text{kHz}$, and (c) using a “Sinc” excitation pulse with three cycles, and $bw_{te} = 744\text{kHz}$. In all cases, the strength of the excitation gradient was adjusted to match the bandwidth of the different shaped pulses. All images were obtained with a total matrix size 64 in the k -encoding direction, and 32 in the time-encoding direction, a FOV 27.0×27.0 mm, and $TE = 23.6$ ms. The lengths of the excitation pulses were $256 \mu\text{s}$ in all cases.

by pulse is equal to the theoretical distance between two successive spin-packets given by: $\frac{\text{FOV}_{te}}{N_{te}}$, where N_{te} is the total number of pixels in the time-encoding direction. If the gradient is not strong enough, adjacent spin-packets will partly overlap, thus lowering the genuine spatial resolution of the image, although the digital resolution has not been reduced.

A partial overlap between successive spin-packets deteriorates the image quality; the extent of this deterioration obviously depends on the extent of the overlap and the excitation profiles of the spin-packet-selective pulses. The effect is larger for pulses with rectangular excitation profiles, because, spins located near the edges of a spin-packets have the same flip angle as spins located in the central parts of the spin-packets. On the other hand, if one uses pulses with non-rectangular excitation profiles, the spins at the edges have smaller flip angles, rendering the effect of the overlap less severe in the final images. This means that in a time-encoding sequence one can usually allow for some degree of overlap, while keeping the image quality reasonably high. This allows one to use weaker time-encoding gradients and narrower time-encoding bandwidths, which makes it possible to reduce the switching rate of the gradients. For example, the time-encoding bandwidths of the images shown in Fig. 4.10 are narrower than in Fig. 4.9, yet both images feature a decent quality.

4.4.4 Time-encoding sequence with uniform susceptibility effects

In Fig. 4.12 another time-encoding sequence is depicted. It is very similar to the previous sequences, with this difference that it has an extra π pulse. In the absence of susceptibility effects the sequences shown in Fig. 4.12 and Fig. 4.5 should give the same results, however in the sequences shown in Fig. 4.5 field inhomogeneities will affect different spin-packets by a different extent. The slice-selection π pulse refocuses field inhomogeneities only if the time interval between the slice-selection π pulse and excitation is the same as the

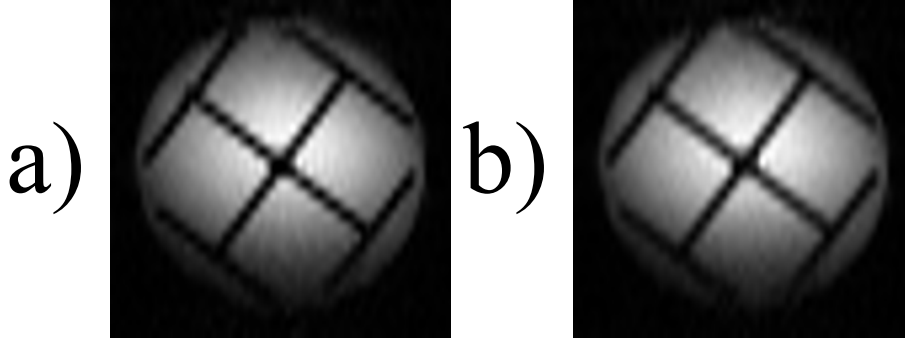


Figure 4.10: Hybrid time-encoding images obtained under exactly the same conditions as in Fig. 4.9b for (a) and as in Fig. 4.9c for (b), but both obtained with a reduced time-encoding bandwidth $bw_{te} = 420\text{kHz}$. Note that, although both images have a satisfactory resolution, the deterioration of the image compared to the case in which there is no overlap is less severe for (a) than for (b). Because, the extent of the overlap is smaller in (a) than in (b) ($\frac{496\text{kHz}}{420\text{kHz}}$ compared to $\frac{744\text{kHz}}{420\text{kHz}}$).

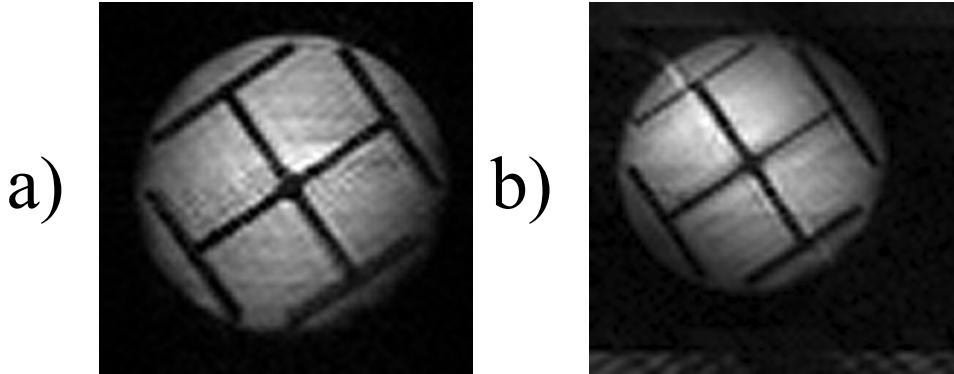


Figure 4.11: (a) Hybrid time-encoding image obtained by the sequence of Fig. 4.12a, with a matrix size 64×64 , FOV 27.0×27.0 mm, and $TE = 15.5$ ms. (b) Hybrid time-encoding image obtained from the sequence of the Fig. 4.12b with the same matrix size and TE as in (a) but with a FOV 32×32 mm. Both images were obtained by a four-fold interleaving. In both cases hard 90° pulses were used for spin-packet excitation.

time interval between the pulse and detection. This is obviously not the case for all spin-packets in the sequences shown in Fig. 4.5. In the sequences shown in Fig. 4.12 on the other hand, there are two π pulses that do not have a refocusing effect. As a result, in the sequences shown in Fig. 4.12 all the spin-packets are uniformly affected by field inhomogeneities.

Figs. 4.11a and b represents two images obtained by the sequences shown in Figs. 4.12a, b respectively. The sequence Fig. 4.11a uses blip gradients in detection block, in which the time-encoding gradient is inactive during data acquisition. As it was mentioned before in this case a proper image can be obtained by performing a 1DFT on each echo. This would not be case for Fig. 4.11b, in which the time-encoding gradient is active during data acquisition. In the latter case a phase correction is needed according to Eq. 4.1, however the new aspect of Figs. 4.11a and b which was not evident in Figs. 4.7d and f is that here the phase factor needed to compensate for the effect is larger than before. Since Eq. 4.1 causes a phase shift between successive data points in both directions, performing a phase correction will move the image in both directions. This movement is evident in Fig. 4.11b but not in Fig. 4.7f, because the phase factor needed for correction is smaller in the latter case. Note that the movement of the image due to the phase correction will results in an aliasing artefact if the field of view, FOV, is not large enough. Therefore in 4.11b, FOV is chosen to be larger than the one in 4.11a. Alternatively, one may move the FOV (in both directions) so that the whole image lies in the FOV after the phase correction.

4.4.5 Importance of the coincidence of echoes

In most pulse sequences, only one readout gradient is active during signal acquisition. If in addition to the readout gradient, another gradient is active during signal acquisition, a phase correction on the raw data is needed before signal processing, as discussed above. In addition, some sequences like those in Figs. 4.5 and 4.12 comprise further gradients that have additional effects. In some time-encoding sequences like in Fig. 4.4, the magnetization will be de-phased during excitation only in the readout direction, and subsequently need to be re-phased only in the readout direction during signal acquisition. In this case one can easily observe the a train of echoes, even if amplitudes of

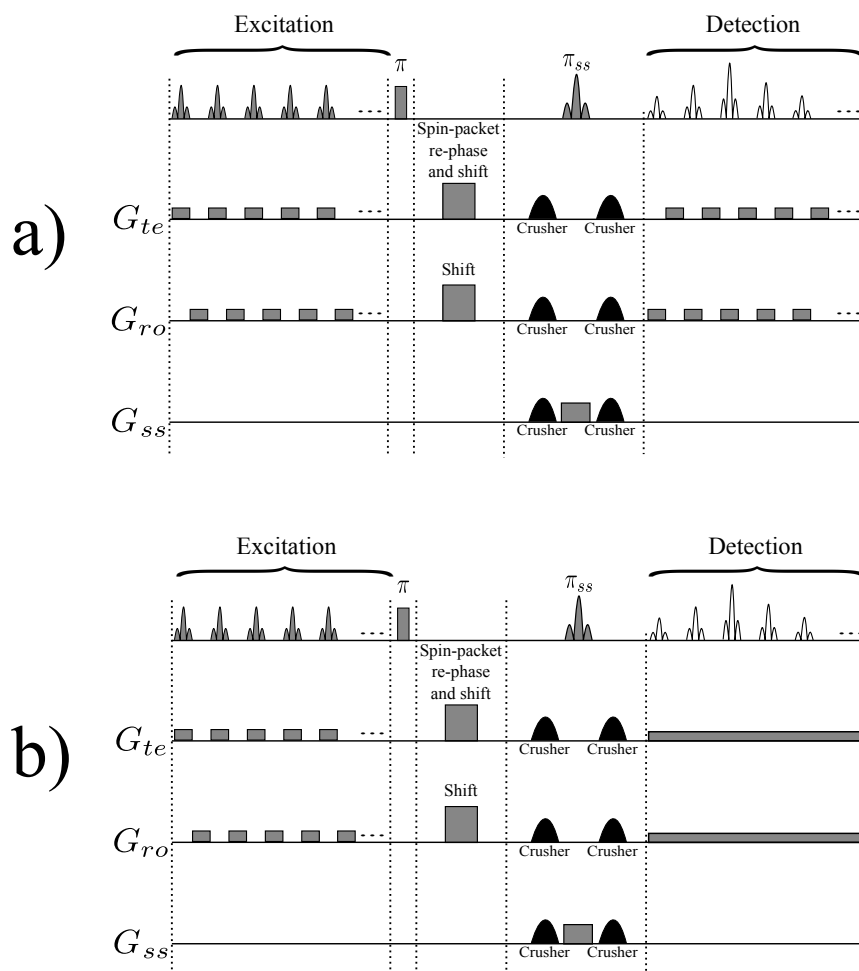


Figure 4.12: (a) The pulse sequence used to produce Fig. 4.11a, and (b) the pulse sequence used to produce Fig. 4.11b. The hard π pulses cause that the effects of field inhomogeneities become the same for all spin-packets. In both sequences G_{ss} , G_{ro} , and G_{te} respectively stand for slice-selection, readout, and time-encoding gradients. The crusher gradients remove artefacts from the image, the shift gradient reverses the detection order, so that TE is identical for all echoes. Spin-packet re-phasing will unwind the phase accumulated during the excitation of the spin-packets.

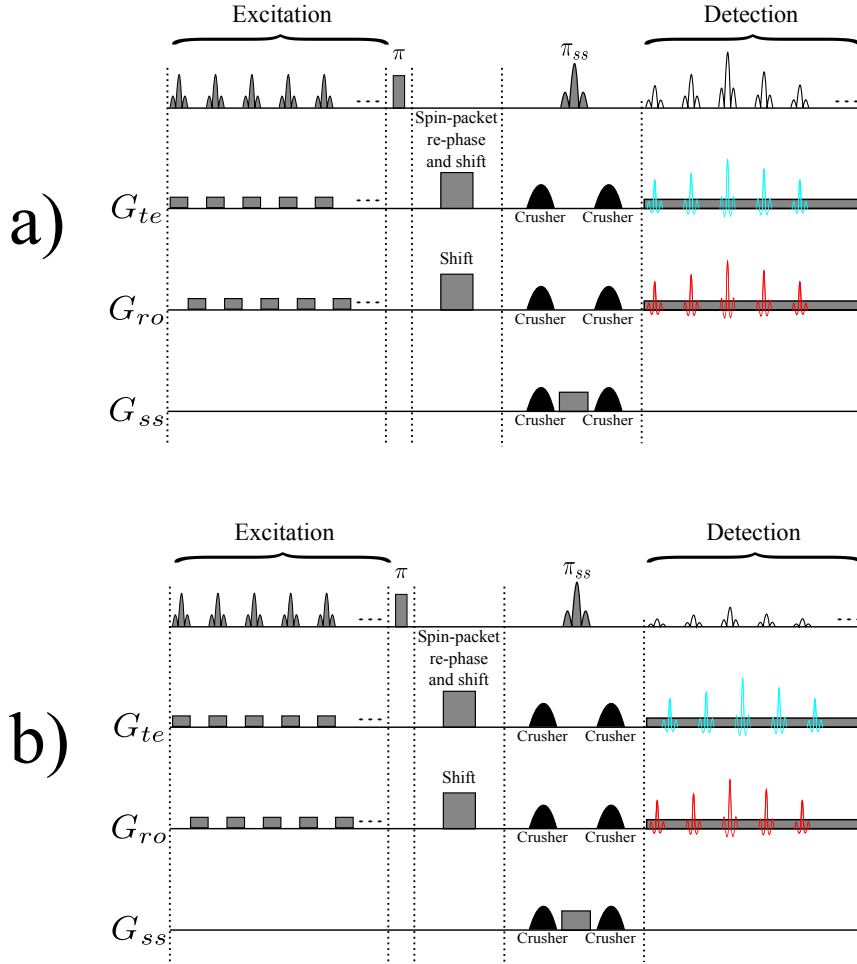


Figure 4.13: (a) A time-encoding sequence in which the echo times are properly adjusted, and (b) a time-encoding sequence in which echo times at time-encoding and readout directions have not been carefully adjusted. Partial echoes are shown in blue and red in time-encoding and readout directions respectively. Note that if the partial echoes does not coincide the total signal will vanish.

different gradients are slightly different from their theoretical value, e.g., due to hardware imperfections. However, in sequences like those of Figs. 4.5 and 4.12 the magnetization is de-phased during the excitation in both time-encoding and readout directions, and must therefore be re-phased in both directions during signal acquisition. Consequently, each of the time-encoding and readout gradients has its own de- and re-phasing effect. Such a situation is depicted in Fig. 4.13.

In fact, when the magnetization is re-phased only in one the directions, a partial echo⁷ occurs. This partial echo may be visible if the de-phasing effects in the other direction are not too large. In such a situation, one should observe the expected signals only if the partial echoes in both directions coincide with each other. Therefore, one must properly match the echo times of the partial echoes in sequences like Figs. 4.5 and 4.12 by careful adjustment of the shift gradients. Otherwise, the signal is diminished or vanishes completely, since each partial echo is attenuated by de-phasing effects of the gradients applied in the other direction.

4.4.6 Concluding remarks

In conclusion in this chapter it has been shown that the original version of hybrid time-encoding sequence can be improved in several aspects. By rearranging positive and negative gradients we have shown how one can reduce the switching rate of the gradients. Moreover, by using an additional gradient we could change the detection order in the original time-encoding sequence. This leads to an identical echo time for all echoes, and hence a uniform signal attenuation due to relaxation. Furthermore, it was shown how one can implement time-encoding sequences in an interleaved fashion in order to reduce signal attenuation due to diffusion. Of course time-encoding sequences proposed in this chapter can still be improved. One perspective is toward a hybrid time-encoding sequence that does not use any switching gradients, which was one of the main motivations for the work presented at this chapter.

⁷Partial, because the magnetization is partially re-phased in one direction, and partially de-phased in the other direction.

Conclusions and perspectives

Various aspects of single-scan spatiotemporal encoding MRI have been discussed in this dissertation. The experimental results show that single-scan k -encoding methods such as EPI can lead to distorted images in inhomogeneous magnetic fields. Single-scan spatiotemporal encoding methods can be an alternative in these conditions as they lead to images that are much less distorted. It was shown that in spatiotemporal encoding sequences, the attenuation of the signal due to diffusion is often not uniform across the entire object, leading to a misleading contrast in the image. One remedy is to modify the sequence so that all the voxels have the same de- and re-phasing intervals. In the case of RASER, this has been done by adding a 180° chirp pulse to the original sequence so as to obtain the double chirp RASER (DC-RASER).

Although in inhomogeneous magnetic fields, single-scan spatiotemporal encoding methods are superior over traditional single-scan methods, they are not completely mature yet. There are a few published works about contrast in spatiotemporal encoding. By modifying the RASER pulse sequence, we achieved the ES-RASER pulse sequence in which one can adjust the contrast due to field inhomogeneities to a desired level. This allows one to take advantage of susceptibility effects as a source of contrast, while avoiding image distortions caused by an inhomogeneous magnetic field. We believe that ES-RASER may offer a viable alternative for EPI. Since it is very effective for suppressing

the effects of field inhomogeneities, which are exacerbated at higher fields at which most fMRI experiments are performed.

The original version of time-encoding sequence can be improved in several aspects. By rearranging positive and negative gradients it has been shown how one can reduce the switching rate of the gradients. This is important because fast gradient switching is not always technically feasible; in addition, it may unwittingly stimulate the patient's nervous system. By using an additional gradient we could change the detection order in the original time-encoding sequence. This leads to an identical echo time for all echoes, and hence to a uniform signal attenuation due to relaxation. Furthermore, we have shown how one can implement time-encoding sequences in an interleaved fashion in order to reduce signal attenuation due to diffusion, and improve resolution. Of course time-encoding sequences proposed in the last chapter can still be improved. One perspective would be a time-encoding sequence that does not use any switching gradients, which was one of the main motivations for the work presented at the last chapter. However, further work is required to realise this perspective.

Bibliography

- [1] R. Schmidt, B. Baishya, N. Ben-Eliezer, A. Seginer, L. Frydman, Super-resolved parallel MRI by spatiotemporal encoding, *Magnetic Resonance Imaging* 32 (2014) 60–70. [doi:10.1016/j.mri.2013.07.007](https://doi.org/10.1016/j.mri.2013.07.007).
- [2] N. Ben-Eliezer, Y. Shrot, L. Frydman, D. K. Sodickson, Parametric analysis of the spatial resolution and signal-to-noise ratio in super-resolved spatiotemporally encoded (SPEN) MRI, *Magnetic Resonance in Medicine* 72 (2014) 418–429. [doi:10.1002/mrm.24954](https://doi.org/10.1002/mrm.24954).
- [3] R. Chamberlain, J. Y. Park, C. Corum, E. Yacoub, K. Ugurbil, C. R. Jack, M. Garwood, RASER: A new ultrafast magnetic resonance imaging method, *Magnetic Resonance in Medicine* 58 (2007) 794–799. [doi:10.1002/mrm.21396](https://doi.org/10.1002/mrm.21396).
- [4] S. Marhabaie, G. Bodenhausen, P. Pelupessy, The effects of molecular diffusion in spatially encoded magnetic resonance imaging, *Journal of Magnetic Resonance* 273 (2016) 98–104. [doi:10.1016/j.jmr.2016.10.010](https://doi.org/10.1016/j.jmr.2016.10.010).
- [5] R. W. Brown, Y.-C. N. Cheng, E. M. Haacke, M. R. Thompson, R. Venkatesan, *Magnetic Resonance Imaging: Physical Principles and Sequence Design*, John Wiley & Sons Ltd, Chichester, 2014. [doi:10.1002/9781118633953](https://doi.org/10.1002/9781118633953).
- [6] C. T. W. Moonen, G. Liu, P. V. Gelderen, G. Sobering, A fast gradient-recalled MRI technique with increased sensitivity to dynamic susceptibility effects, *Magnetic Resonance in Medicine* 26 (1992) 184–189. [doi:10.1002/mrm.1910260118](https://doi.org/10.1002/mrm.1910260118).

-
- [7] S. Marhabaie, G. Bodenhausen, P. Pelupessy, Susceptibility contrast by echo shifting in spatially encoded single-scan mri, *Physical Chemistry Chemical Physics* 19 (2017) 14210–14213. [doi:10.1039/C7CP01898C](https://doi.org/10.1039/C7CP01898C).
- [8] P. Mansfield, Multi-planar image formation using nmr spin echoes, *Journal of Physics C: Solid State Physics* 10 (1977) L55–L58.
- [9] P. Mansfield, A. Maudsley, Planar spin imaging by NMR, *Journal of Magnetic Resonance* (1969) 27 (1977) 101–119. [doi:10.1016/0022-2364\(77\)90197-4](https://doi.org/10.1016/0022-2364(77)90197-4).
- [10] S. Bushong, G. Clarke, *Magnetic Resonance Imaging: Physical and Biological Principles*, Elsevier Mosby, St. Louis, 2014, Ch. 20.
- [11] J. Groebner, R. Umathum, M. Bock, A. J. Krafft, W. Semmler, J. Rauschenberg, MR safety: simultaneous B_0 , $d\Phi/dt$, and dB/dt measurements on MR-workers up to 7 T, *Magnetic Resonance Materials in Physics, Biology and Medicine* 24 (2011) 315–322. [doi:10.1007/s10334-011-0270-y](https://doi.org/10.1007/s10334-011-0270-y).
- [12] M. E. Meyerand, E. C. Wong, A time encoding method for single-shot imaging, *Magnetic Resonance in Medicine* 34 (1995) 618–622. [doi:10.1002/mrm.1910340419](https://doi.org/10.1002/mrm.1910340419).
- [13] M. E. Meyerand, C. H. Moritz, E. C. Wong, Single-shot, motion insensitive cardiac imaging on a standard clinical system, *Magnetic Resonance in Medicine* 40 (1998) 930–933. [doi:10.1002/mrm.1910400620](https://doi.org/10.1002/mrm.1910400620).
- [14] S. H. Faro, F. B. Mohamed (Eds.), *BOLD fMRI*, Springer, New York, 2010, Ch. 2.
- [15] D. M. Grant, R. K. Harris (Eds.), *Encyclopedia of nuclear magnetic resonance*, John Wiley, Baffins lane, Chichester, 1996.
- [16] E. L. Hahn, Felix Bloch and magnetic resonance, *Bulletin of Magnetic Resonance* 7 (1985) 82–89.
- [17] N. F. Ramsey, Early history of magnetic resonance, *Bulletin of Magnetic Resonance* 7 (1985) 94–99.

-
- [18] C. Gorter, Negative result of an attempt to detect nuclear magnetic spins, *Physica* 3 (1936) 995–998. [doi:10.1016/S0031-8914\(36\)80324-3](https://doi.org/10.1016/S0031-8914(36)80324-3).
- [19] I. I. Rabi, Space quantization in a gyrating magnetic field, *Physical Review* 51 (1937) 652–654. [doi:10.1103/PhysRev.51.652](https://doi.org/10.1103/PhysRev.51.652).
- [20] I. I. Rabi, J. R. Zacharias, S. Millman, P. Kusch, A new method of measuring nuclear magnetic moment, *Physical Review* 53 (1938) 318–318. [doi:10.1103/PhysRev.53.318](https://doi.org/10.1103/PhysRev.53.318).
- [21] F. Bloch, Nuclear induction, *Physical Review* 70 (1946) 460–474. [doi:10.1103/PhysRev.70.460](https://doi.org/10.1103/PhysRev.70.460).
- [22] F. Bloch, W. W. Hansen, M. Packard, The nuclear induction experiment, *Physical Review* 70 (1946) 474–485. [doi:10.1103/PhysRev.70.474](https://doi.org/10.1103/PhysRev.70.474).
- [23] E. M. Purcell, H. C. Torrey, R. V. Pound, Resonance absorption by nuclear magnetic moments in a solid, *Physical Review* 69 (1946) 37–38. [doi:10.1103/PhysRev.69.37](https://doi.org/10.1103/PhysRev.69.37).
- [24] R. R. Ernst, W. A. Anderson, Application of Fourier Transform Spectroscopy to Magnetic Resonance, *Review of Scientific Instruments* 37 (1966) 93–102. [doi:10.1063/1.1719961](https://doi.org/10.1063/1.1719961).
- [25] W. P. Aue, E. Bartholdi, R. R. Ernst, Two-dimensional spectroscopy. Application to nuclear magnetic resonance, *The Journal of Chemical Physics* 64 (1976) 2229–2246. [doi:10.1063/1.432450](https://doi.org/10.1063/1.432450).
- [26] J. Jeener, P. Broekaert, Nuclear magnetic resonance in solids: Thermodynamic effects of a pair of rf pulses, *Physical Review* 157 (1967) 232–240. [doi:10.1103/PhysRev.157.232](https://doi.org/10.1103/PhysRev.157.232).
- [27] C. Slichter, *Principles of Magnetic Resonance*, Springer-Verlag, Berlin, 1990.
- [28] J. V. Hajnal, D. J. Bryant, L. Kasuboski, P. M. Pattany, B. De Coene, P. D. Lewis, J. M. Pennock, A. Oatridge, I. R. Young, G. M. Bydder, Use of fluid attenuated

- inversion recovery (FLAIR) pulse sequences in MRI of the brain., *Journal of computer assisted tomography* 16 (1992) 841–844.
- [29] H. Y. Carr, Free precession techniques in nuclear magnetic resonance, Ph.D. thesis (1953).
- [30] H. Y. Carr, Field Gradients in Early MRI, *Physics Today* 57 (2004) 83–83. [doi:10.1063/1.1784322](https://doi.org/10.1063/1.1784322).
- [31] B. MacWilliams, Russian claims first in magnetic imaging, *Nature* 426 (2003) 375–375. [doi:10.1038/426375a](https://doi.org/10.1038/426375a).
- [32] R. Damadian, Tumor detection by nuclear magnetic resonance, *Science* 171 (1971) 1151–1153. [doi:10.1126/science.171.3976.1151](https://doi.org/10.1126/science.171.3976.1151).
- [33] R. Damadian, Apparatus and method for detecting cancer in tissue (US Patent, 3789832 A).
- [34] W. S. Hinshaw, Image formation by nuclear magnetic resonance: the sensitive-point method, *Journal of Applied Physics* 47 (1976) 3709–3721. [doi:10.1063/1.323136](https://doi.org/10.1063/1.323136).
- [35] R. Damadian, L. Minkoff, M. Goldsmith, M. Stanford, J. Koutcher, Field focusing nuclear magnetic resonance (FONAR): visualization of a tumor in a live animal, *Science* 194 (1976) 1430–1432. [doi:10.1126/science.1006309](https://doi.org/10.1126/science.1006309).
- [36] R. Damadian, Field focusing n.m.r. (FONAR) and the formation of chemical images in man, *Philosophical Transactions of the Royal Society of London B: Biological Sciences* 289 (1980) 489–500. [doi:10.1098/rstb.1980.0067](https://doi.org/10.1098/rstb.1980.0067).
- [37] P. C. Lauterbur, Image Formation by Induced Local Interactions: Examples Employing Nuclear Magnetic Resonance, *Nature* 242 (1974) 190–191.
- [38] E. D. Becker, Paul Christian Lauterbur, *Physics Today* 60 (2007) 77–78. [doi:10.1063/1.2761815](https://doi.org/10.1063/1.2761815).

- [39] P. Mansfield, P. K. Grannell, NMR 'diffraction' in solids?, *Journal of Physics C: Solid State Physics* 6 (1973) L422–L426.
- [40] A. N. Garroway, P. K. Grannell, P. Mansfield, Image formation in NMR by a selective irradiative process, *Journal of Physics C: Solid State Physics* 7 (1974) L457–L462.
- [41] P. Mansfield, A. A. Maudsley, Medical imaging by NMR, *The British Journal of Radiology* 50 (1977) 188–194. [doi:10.1259/0007-1285-50-591-188](https://doi.org/10.1259/0007-1285-50-591-188).
- [42] A. Kumar, D. Welti, R. R. Ernst, NMR Fourier zeugmatography, *Journal of Magnetic Resonance* (1969) 18 (1975) 69–83. [doi:10.1016/0022-2364\(75\)90224-3](https://doi.org/10.1016/0022-2364(75)90224-3).
- [43] R. S. Likes, Moving gradient zeugmatography (US Patent 4307343 A).
- [44] S. Ljunggren, A simple graphical representation of Fourier-based imaging methods, *Journal of Magnetic Resonance* (1969) 54 (1983) 338–343. [doi:10.1016/0022-2364\(83\)90060-4](https://doi.org/10.1016/0022-2364(83)90060-4).
- [45] D. B. Twieg, The k -trajectory formulation of the NMR imaging process with applications in analysis and synthesis of imaging methods, *Medical Physics* 10 (1983) 610–621. [doi:10.1118/1.595331](https://doi.org/10.1118/1.595331).
- [46] N. Ben-Eliezer, M. Irani, L. Frydman, Super-resolved spatially encoded single-scan 2D MRI, *Magnetic Resonance in Medicine* 63 (2010) 1594–1600. [doi:10.1002/mrm.22377](https://doi.org/10.1002/mrm.22377).
- [47] N. Ben-Eliezer, Y. Shrot, L. Frydman, High-definition, single-scan 2D MRI in inhomogeneous fields using spatial encoding methods, *Magnetic Resonance Imaging* 28 (2010) 77–86. [doi:10.1016/j.mri.2009.05.026](https://doi.org/10.1016/j.mri.2009.05.026).
- [48] J. G. Pipe, Spatial Encoding and Reconstruction in MRI with Quadratic Phase Profiles, *Magnetic Resonance in Medicine* 33 (1995) 24–33. [doi:10.1002/mrm.1910330105](https://doi.org/10.1002/mrm.1910330105).
- [49] M. E. Meyerand, E. C. Wong, H. A. J. S. Hyde, Time encoded magnetic resonance

- imaging: a novel single-shot technique, Proceedings ISMRM, 12th Annual Scientific Meeting, New York, 1993, p. 472.
- [50] M. E. Meyerand, E. C. Wong, A modified time encoded method for high resolution imaging, Proceedings ISMRM, 12th Annual Meeting and Exhibition, Nice, 1995, p. 637.
- [51] M. E. Meyerand, C. H. Moritz, E. C. Wong, Single-shot, motion insensitive cardiac imaging on a standard clinical system, Proceedings ISMRM, 4th Scientific Meeting, New York, 1996, p. 658.
- [52] J. G. Pipe, Analysis of localized quadratic encoding and reconstruction, *Magnetic Resonance in Medicine* 36 (1996) 137–146. [doi:10.1002/mrm.1910360122](https://doi.org/10.1002/mrm.1910360122).
- [53] Y. Shrot, L. Frydman, Spatially encoded NMR and the acquisition of 2D magnetic resonance images within a single scan, *Journal of Magnetic Resonance* 172 (2005) 179–190. [doi:10.1016/j.jmr.2004.09.024](https://doi.org/10.1016/j.jmr.2004.09.024).
- [54] A. Tal, L. Frydman, Spatial encoding and the single-scan acquisition of high definition MR images in inhomogeneous fields, *Journal of Magnetic Resonance* 182 (2006) 179–194. [doi:10.1016/j.jmr.2006.06.022](https://doi.org/10.1016/j.jmr.2006.06.022).
- [55] Z. Zhang, A. Seginer, L. Frydman, Single-scan MRI with exceptional resilience to field heterogeneities, *Magnetic Resonance in Medicine* 77 (2017) 623–634. [doi:10.1002/mrm.26145](https://doi.org/10.1002/mrm.26145).
- [56] U. Goerke, M. Garwood, K. Ugurbil, Functional magnetic resonance imaging using RASER, *NeuroImage* 54 (2011) 350–360. [doi:10.1016/j.neuroimage.2010.08.011](https://doi.org/10.1016/j.neuroimage.2010.08.011).
- [57] U. Goerke, Spatial specificity in spatiotemporal encoding and Fourier imaging, *Magnetic Resonance Imaging* 34 (2016) 562 – 573. [doi:10.1016/j.mri.2015.12.029](https://doi.org/10.1016/j.mri.2015.12.029).

- [58] R. Paquin, P. Pelupessy, G. Bodenhausen, Cross-encoded magnetic resonance imaging in inhomogeneous fields, *Journal of Magnetic Resonance* 201 (2009) 199–204. [doi:10.1016/j.jmr.2009.09.008](https://doi.org/10.1016/j.jmr.2009.09.008).
- [59] N. Ben-Eliezer, E. Solomon, E. Harel, N. Nevo, L. Frydman, Fully refocused multi-shot spatiotemporally encoded MRI: Robust imaging in the presence of metallic implants, *Magnetic Resonance Materials in Physics, Biology and Medicine* 25 (2012) 433–442. [doi:10.1007/s10334-012-0318-7](https://doi.org/10.1007/s10334-012-0318-7).
- [60] P. Shewmon, *Diffusion in Solids*, Springer International Publishing, Cham, 2016. [doi:10.1007/978-3-319-48206-4](https://doi.org/10.1007/978-3-319-48206-4).
- [61] A. Fick, Über diffusion, *Annalen der Physik* 170 (1855) 59–86. [doi:10.1002/andp.18551700105](https://doi.org/10.1002/andp.18551700105).
- [62] W. Sutherland, The measurement of large molecular masses, Australasian Association for the Advancement of Science, Report of Meeting, Dunedin, 1904.
- [63] W. Sutherland, A dynamical theory of diffusion for non-electrolytes and the molecular mass of albumin, *The London, Edinburgh, and Dublin Philosophical Magazine and Journal of Science* 9 (1905) 781–785. [doi:10.1080/14786440509463331](https://doi.org/10.1080/14786440509463331).
- [64] A. Einstein, Über die von der molekularkinetischen Theorie der Wärme geforderte Bewegung von in ruhenden Flüssigkeiten suspendierten Teilchen, *Annalen der Physik* 322 (1905) 549–560. [doi:10.1002/andp.19053220806](https://doi.org/10.1002/andp.19053220806).
- [65] M. von Smoluchowski, Zur kinetischen theorie der brownschen molekularbewegung und der suspensionen, *Annalen der Physik* 326 (1906) 756–780. [doi:10.1002/andp.19063261405](https://doi.org/10.1002/andp.19063261405).
- [66] P. T. Callaghan, *Translational Dynamics and Magnetic Resonance: Principles of Pulsed Gradient Spin Echo NMR*, Oxford University Press, Oxford, 2011. [doi:10.1093/acprof:oso/9780199556984.001.0001](https://doi.org/10.1093/acprof:oso/9780199556984.001.0001).

- [67] E. L. Hahn, Spin echoes, *Physical Review* 80 (1950) 580–594. [doi:10.1103/PhysRev.80.580](https://doi.org/10.1103/PhysRev.80.580).
- [68] H. Y. Carr, E. M. Purcell, Effects of diffusion on free precession in nuclear magnetic resonance experiments, *Physical Review* 94 (1954) 630–638. [doi:10.1103/PhysRev.94.630](https://doi.org/10.1103/PhysRev.94.630).
- [69] H. C. Torrey, Bloch equations with diffusion terms, *Physical Review* 104 (1956) 563–565. [doi:10.1103/PhysRev.104.563](https://doi.org/10.1103/PhysRev.104.563).
- [70] N. M. Loening, J. Keeler, G. A. Morris, One-Dimensional DOSY, *Journal of Magnetic Resonance* 153 (2001) 103–112.
- [71] M. J. Thrippleton, N. M. Loening, J. Keeler, A fast method for the measurement of diffusion coefficients: one-dimensional DOSY, *Magnetic Resonance in Chemistry* 41 (2003) 441–447. [doi:10.1002/mrc.1195](https://doi.org/10.1002/mrc.1195).
- [72] Y. Shrot, L. Frydman, Single-scan 2D DOSY NMR spectroscopy, *Journal of Magnetic Resonance* 195 (2008) 226–231. [doi:10.1016/j.jmr.2008.09.011](https://doi.org/10.1016/j.jmr.2008.09.011).
- [73] L. Guduff, I. Kuprov, C. van Heijenoort, J.-N. Dumez, Spatially encoded 2D and 3D diffusion-ordered NMR spectroscopy, *Chemical Communications* 53 (2017) 701–704. [doi:10.1039/C6CC09028A](https://doi.org/10.1039/C6CC09028A).
- [74] R. T. Constable, J. C. Gore, The Loss of Small Objects in Variable TE Imaging: Implications for FSE, RARE, and EPI, *Magnetic Resonance in Medicine* 28 (1992) 9–24. [doi:10.1002/mrm.1910280103](https://doi.org/10.1002/mrm.1910280103).
- [75] P. Giraudeau, S. Akoka, Sources of sensitivity losses in ultrafast 2D NMR, *Journal of Magnetic Resonance* 192 (2008) 151–158. [doi:10.1016/j.jmr.2008.02.007](https://doi.org/10.1016/j.jmr.2008.02.007).
- [76] P. Giraudeau, S. Akoka, Sensitivity losses and line shape modifications due to molecular diffusion in continuous encoding ultrafast 2D NMR experiments, *Journal of Magnetic Resonance* 195 (2008) 9–16. [doi:10.1016/j.jmr.2008.08.001](https://doi.org/10.1016/j.jmr.2008.08.001).

- [77] J.-M. Bohlen, M. Rey, G. Bodenhausen, Refocusing with chirped pulses for broadband excitation without phase dispersion, *Journal of Magnetic Resonance* (1969) 84 (1989) 191–197. [doi:10.1016/0022-2364\(89\)90018-8](https://doi.org/10.1016/0022-2364(89)90018-8).
- [78] E. Kupce, R. Freeman, Adiabatic Pulses for Wideband Inversion and Broadband Decoupling, *Journal of Magnetic Resonance* 115 (1995) 273–276. [doi:10.1006/jmra.1995.1179](https://doi.org/10.1006/jmra.1995.1179).
- [79] Y. Chen, J. Li, X. Qu, L. Chen, C. Cai, S. Cai, J. Zhong, Z. Chen, Partial Fourier transform reconstruction for single-shot MRI with linear frequency-swept excitation, *Magnetic Resonance in Medicine* 69 (2013) 1326–1336. [doi:10.1002/mrm.24366](https://doi.org/10.1002/mrm.24366).
- [80] L. Ciobanu, E. Solomon, N. Pyatigorskaya, T. Roussel, D. Le Bihan, L. Frydman, fMRI contrast at high and ultrahigh magnetic fields: Insight from complementary methods, *NeuroImage* 113 (2015) 37–43. [doi:10.1016/j.neuroimage.2015.03.018](https://doi.org/10.1016/j.neuroimage.2015.03.018).
- [81] E. Solomon, N. Nissan, R. Schmidt, E. Furman-Haran, U. Ben-Aharon, L. Frydman, Removing silicone artifacts in diffusion-weighted breast MRI by means of shift-resolved spatiotemporally encoding, *Magnetic Resonance in Medicine* 75 (2016) 2064–2071. [doi:10.1002/mrm.25757](https://doi.org/10.1002/mrm.25757).
- [82] T. Zhang, L. Chen, J. Huang, J. Li, S. Cai, C. Cai, Z. Chen, Ultrafast multi-slice spatiotemporally encoded MRI with slice-selective dimension segmented, *Journal of Magnetic Resonance* 269 (2016) 138–145. [doi:10.1016/j.jmr.2016.06.002](https://doi.org/10.1016/j.jmr.2016.06.002).
- [83] J.-N. Dumez, L. Frydman, Multidimensional excitation pulses based on spatiotemporal encoding concepts, *Journal of Magnetic Resonance* 226 (2013) 22–34. [doi:10.1016/j.jmr.2012.10.010](https://doi.org/10.1016/j.jmr.2012.10.010).
- [84] J.-N. Dumez, R. Schmidt, L. Frydman, Simultaneous spatial and spectral selectivity by spatiotemporal encoding, *Magnetic Resonance in Medicine* 71 (2014) 746–755.

- [doi:10.1002/mrm.24718](https://doi.org/10.1002/mrm.24718).
- [85] A. L. S. Snyder, C. A. Corum, S. Moeller, N. J. Powell, M. Garwood, MRI by steering resonance through space, *Magnetic Resonance in Medicine* 72 (2014) 49–58. [doi:10.1002/mrm.24888](https://doi.org/10.1002/mrm.24888).
- [86] G. Liu, G. Sobering, A. W. Olson, P. Van Gelderen, C. T. W. Moonen, Fast echo-shifted gradient-recalled MRI: Combining a short repetition time with variable T_2^* weighting, *Magnetic Resonance in Medicine* 30 (1993) 68–75. [doi:10.1002/mrm.1910300111](https://doi.org/10.1002/mrm.1910300111).
- [87] P. van Gelderen, J. H. Duyn, N. F. Ramsey, G. Liu, C. T. W. Moonen, The PRESTO technique for fMRI, *NeuroImage* 62 (2012) 676–681. [doi:10.1016/j.neuroimage.2012.01.017](https://doi.org/10.1016/j.neuroimage.2012.01.017).
- [88] H. Geen, R. Freeman, Band-selective radiofrequency pulses, *Journal of Magnetic Resonance* (1969) 93 (1991) 93–141. [doi:10.1016/0022-2364\(91\)90034-Q](https://doi.org/10.1016/0022-2364(91)90034-Q).
- [89] M. Stehling, R. Turner, P. Mansfield, Echo-planar imaging: magnetic resonance imaging in a fraction of a second, *Science* 254 (1991) 43–50. [doi:10.1126/science.1925560](https://doi.org/10.1126/science.1925560).
- [90] J. Hennig, M. Hodapp, Burst imaging, *Magma* 1 (1993) 39–48. [doi:10.1007/BF02660372](https://doi.org/10.1007/BF02660372).
- [91] J. Hennig, M. Mueri, Fast imaging using burst excitation pulses, *Proceedings of 7th ISMRM*, San Francisco, 1988, p. 238.
- [92] S. J. Doran, M. E. Bourgeois, M. O. Leach, Burst imaging—Can it ever be useful in the clinic?, *Concepts in Magnetic Resonance Part A* 26 (2005) 11–34. [doi:10.1002/cmr.a.20035](https://doi.org/10.1002/cmr.a.20035).
- [93] J. Tsao, Ultrafast imaging: Principles, pitfalls, solutions, and applications, *Journal of Magnetic Resonance Imaging* 32 (2010) 252–266. [doi:10.1002/jmri.22239](https://doi.org/10.1002/jmri.22239).

-
- [94] F. Hennel, J.-F. Nédélec, Interleaved asymmetric echo-planar imaging, *Magnetic Resonance in Medicine* 34 (1995) 520–524. [doi:10.1002/mrm.1910340406](https://doi.org/10.1002/mrm.1910340406).

CURRICULUM VITAE

Sina Marhabaie

Education:

- ⤴ PhD in Physical Chemistry, École Normale Supérieure-Paris, May 2014-December 2017.
- ⤴ MSc in Physical Chemistry, Sharif University of Technology, September 2010-2012, (GPA: 18.33 / 20).
- ⤴ BSc in Physics, Sharif University of Technology, June 2008-2010, (GPA: 18.06 / 20).
- ⤴ BSc in Chemistry, Sharif University of Technology, September 2005-June 2009, (GPA: 18.06 / 20).

Honors and Awards:

- ⤴ Silver Medal, Ranked Second, International Scientific Olympiad (Chemistry), Tehran, Iran, July 2009.
- ⤴ Member of Iranian National Elites Foundation.
- ⤴ Ranked First among BSc Chemistry students.
- ⤴ Ranked Second among BSc Physics students.

Publications:

- ⤴ Sina Marhabaie, and Mohsen Tafazzoli, "QUADRELAX: A Program for Computing Relaxation Data for Quadrupolar Nuclei, Including Chemical Exchange Effects", Concepts in Magnetic Resonance, 228-236, 2014.
- ⤴ Sina Marhabaie, Geoffrey Bodenhausen, and Philippe Pelupessy, "The effects of molecular diffusion in spatially encoded magnetic resonance imaging", Journal of Magnetic Resonance 98-104, 2016.
- ⤴ Sina Marhabaie, and Piotr Tekely, "Toward Recording ^{33}S NMR Spectra of Cross-Linked Elastomers: Relaxation Dynamics Perspective", Concepts Magn Reson Part A, e21386, 2017.
- ⤴ Sina Marhabaie, Geoffrey Bodenhausen, and Philippe Pelupessy, "Susceptibility contrast by echo shifting in spatially encoded single-scan MRI", Phys. Chem. Chem. Phys., 14210-14213, 2017.
- ⤴ Dennis Kurzbach, et al, "Dissolution dynamic nuclear polarization of deuterated molecules enhanced by cross-polarization", The Journal of Chemical Physics 145, 194203, 2016.
- ⤴ David Guarin, et al, "Characterizing Thermal Mixing DNP via Cross-Talk between Spin Reservoirs", J. Phys. Chem. Lett. 2017, 8, 5531-5536.

Presentations and posters:

- ⤴ Sina Marhabaie, Geoffrey Bodenhausen, and Philippe Pelupessy, "Susceptibility contrast by echo shifting in spatially encoded single-scan MRI", Oral presentation, Euromar conference,

Warsaw, 5th July 2017.

- ⤴ Sina Marhabaie, Geoffrey Bodenhausen, and Philippe Pelupessy, “Susceptibility contrast by echo shifting in spatially encoded single-scan MRI”, Poster presentation, Euromar conference, Warsaw, July 2017.
- ⤴ Sina Marhabaie, Geoffrey Bodenhausen, and Philippe Pelupessy, “The Role of Diffusion in Spatially Encoded MRI”, Poster presentation, Euromar conference, Aarhus, July 2016.

Research interests:

- ⤴ Magnetic Resonance Imaging, Chemical Physics

Scientific Skills:

- ⤴ Experienced in working with Bruker spectrometers, and familiar with routine MRI experiments.
- ⤴ Experienced in working with basic chemical analysis instruments, (GC, UV/Vis, ...)

Computer Skills:

- ⤴ Python, Latex, Top spin, Paravision programming, Octave, Office

Work and Teaching Experiences:

- ⤴ Aryan Fan Azma Co, (responsible for development of new experiments for analyzing water samples), November 2011-May 2014.
- ⤴ Teaching Assistant, General Chemistry, Sharif University of Technology, Spring 2012 semester.
- ⤴ Teaching Assistant, General Chemistry, Sharif University of Technology, Fall 2011 semester.
- ⤴ Teaching chemistry to high school students who want to prepare for the Chemistry Olympiad, September 2007-February 2010.
- ⤴ Tutoring general mathematics.
- ⤴ Tutoring high school courses.

Hobbies and Entertainments:

- ⤴ Composing, reading and memorizing classical poetry in Persian (I can recite more than half of Hafiz poems by heart).

Résumé

Il y a plus de soixante-dix ans que la résonance magnétique nucléaire (RMN) a été découverte, mais elle est toujours prospère et vivante, couvrant un large éventail d'applications dans les sciences, technologies et industries. Une application omniprésente de la résonance magnétique nucléaire est une technique appelée imagerie par résonance magnétique (IRM), qui a trouvé beaucoup d'applications en sciences, en technologie, et particulièrement en médecine.

Il a été montré que les techniques d'imagerie hybride à balayage unique, qui utilisent l'encodage k traditionnel dans une direction et l'encodage spatiotemporel dans l'autre, sont supérieures aux méthodes traditionnelles qui utilisent l'encodage k dans les deux directions, notamment pour supprimer les effets de variations de fréquence (causées par des champs magnétique inhomogènes, ou par la présence de plusieurs déplacements chimiques, ou par toute autre source de variations de fréquence), et conduisent à des images beaucoup moins déformées que les méthodes d'imagerie traditionnelles. Dans cette thèse, l'idée de l'imagerie par résonance magnétique par encodage spatial sera discutée. La formation de l'image et les propriétés des images résultant de différentes séquences d'encodage spatial seront brièvement étudiées.

Les effets de la diffusion sur une séquence hybride établie appelée 'acquisition rapide par excitation séquentielle et refocalisation (RASER)' sont étudiés. On montrera que dans les séquences d'encodage spatial, l'atténuation du signal due à la diffusion n'est souvent pas uniforme sur l'ensemble de l'objet, provoquant un contraste trompeur dans l'image. Afin d'éliminer ce faux contraste, une séquence d'impulsion comprenant deux impulsions balayées en fréquence (DC-RASER) est proposée. Les résultats expérimentaux sont conformes à nos prévisions théoriques sur les effets de la diffusion dans ces séquences. Ils confirment que l'atténuation du signal due à la diffusion est uniforme sur l'ensemble de l'objet.

Afin de développer les applications de l'encodage spatial à balayage unique, nous montrons comment on peut améliorer le contraste dans la séquence originale RASER. En changeant le déroulement de la séquence d'impulsions, nous avons réalisé une variante de RASER appelée RASER avec écho décalé (ES-RASER), qui fournit un niveau de contraste ajustable.

Enfin, nous montrons comment on peut améliorer quelques aspects des séquences à encodage temporel disponibles. En réarrangeant les gradients positifs et négatifs, nous montrons comment on peut réduire la vitesse de la commutation des gradients. Ceci est important, car une commutation rapide des gradients n'est pas toujours techniquement possible et peut en plus stimuler involontairement le système nerveux du patient. En utilisant un gradient supplémentaire, nous avons pu modifier l'ordre de détection dans la séquence originale d'encodage temporel. Cela conduit à un temps d'écho identique pour tous les échos, et à une atténuation uniforme du signal due à la relaxation. Finalement, nous montrons comment on peut répartir l'acquisition des séquences d'encodage temporel de façon entrelacée, afin de réduire l'atténuation du signal due à la diffusion.

Mots Clés

IRM, Encodage spatial, Encodage temporel, Encodage spatiotemporel, SPEN, RASER

Abstract

Although Nuclear Magnetic Resonance (NMR) has been discovered more than seventy years ago, it is still thriving and alive, covering a very broad spectrum of applications in science, technology and industry. One of the most ubiquitous applications of Nuclear Magnetic Resonance is a technique dubbed Magnetic Resonance Imaging (MRI), which has found many applications in science, technology, and particularly in medicine.

Single-scan hybrid imaging techniques that use traditional k -encoding in one direction, and spatiotemporal encoding in the other have been shown to be superior to traditional full k -encoding methods (that use k -encoding in both directions) in suppressing the effects of frequency variations (caused by inhomogeneous magnetic fields, the presence of more than one chemical shift, or any other frequency variation) and lead to images that are much less distorted than traditional single-scan imaging methods. In this dissertation the main idea behind spatial encoding magnetic resonance imaging will be introduced. Image formation and image properties in different spatial encoding sequences will also be briefly investigated.

Then, the effects of diffusion on an established hybrid sequence called "Rapid Acquisition by Sequential Excitation and Refocusing, RASER" are investigated. It will be shown that in spatial encoding sequences, the attenuation of the signal due to diffusion is often not uniform across the entire object, leading to a misleading contrast in the image. In order to eliminate this misleading contrast, a double-chirp RASER (DC-RASER) pulse sequence is proposed in this work. The experimental results are in accordance with our theoretical investigations about the effects of diffusion in these sequences. They also confirm that the signal attenuation due to diffusion is uniform, as expected theoretically for DC-RASER.

In order to develop applications of single-scan spatial encoding MRI we show how one can enhance the contrast in the original RASER sequence. By changing the timing of the pulse sequence, we achieved a variant of RASER called Echo Shifted RASER (ES-RASER), which provides a tunable contrast level.

Finally, we show how one can improve a few aspects of the available time-encoding sequences. By rearranging positive and negative gradients we show how one can reduce the switching rate of the gradients. This is important because fast gradient switching is not always technically feasible; in addition, it may unwittingly stimulate the patient's nervous system. By using an additional gradient we could change the detection order in the original time-encoding sequence. This leads to an identical echo-time for all echoes, and hence a uniform signal attenuation due to relaxation. Furthermore, we show how one can implement time-encoding sequences in an interleaved fashion in order to reduce signal attenuation due to diffusion.

Keywords

MRI, Spatial encoding, Time-encoding, Spatiotemporal encoding, SPEN, RASER